DATA ANALYSIS OF TWO NON-ISOTHERMAL TURBULENT JETS

Data Analysis of Two Opposing Non-Isothermal Turbulent Jets

By

DAN QUACH, B.ENG.

A Project Report

Submitted to the School of Graduate Studies

in Partial Fulfillment of the Requirements

for the Degree of

Master's of Engineering

McMaster University

Abstract

A three-component Laser Doppler Anemometer (LDA) instrument, an array of stationary thermocouples and a moving thermocouple were used to capture the three-dimensional flow and temperature fields for the system of two opposing axisymmetric turbulent jets. It was found that buoyancy-induced curvature of the hot jet resulted in cross shearing with the opposing jet. The following report will investigate the adequacy of the current experimental measurements for the identification of coherent structures and the characterization of their effects on the mean flow. Identification tools include the power spectra and conditional average velocity measurements based on the Window Average Gradient (WAG). It was determined that the low sampling and large spatial positions of the thermocouple measurements were not for the retrieval of quantitative turbulence data. For the velocity measurements, the LDA data were found to be adequate in regions of low turbulence intensities but degraded as the measurements approached the region where the two jet shear layers interacted. The detection of periodic structures from the power spectrum was inconclusive due to noise. The WAG algorithm was affected by the irregular sampling and required modification. For the events detected, an intermittency factor of 16.4% at the interaction region of two shear layers was observed. In addition, these results suggest that these events contribute 30% of the mean momentum transfer across the jet. Furthermore, the contribution of these events to the lateral component of the turbulent kinetic energy was nearly eight times larger than the contributions to the axial or transverse direction.

Acknowledgements

The author graciously acknowledges the help and guidance that was provided during the process of making this report. I would like to thank my supervisors Jacek Szymanski, Drs. David Jackson and Dan Ewing for their dedication, patience and valuable assistance that enhanced the presentation of this report. To Drs. Hans van Maanen and Holger Nobach who provided their expert opinions in the field of LDA by answering my (never-ending) questions. Special thanks also to David Novog who played an instrumental role as the interface between me and the individuals at Chalk River Laboratories. I am also in debt to Dr. John Mackinnon and the Nuclear Safety Analysis Division (NSAD) at Nuclear Safety Solutions Limited for providing the financial assistance and opportunity to complete the Ontario Power Generation NSAD scholarship program.

Last but not least, I want to thank Sasha Patton for her support and assistance in editing this paper.

Table of Contents

Table of Figures

List of Tables

Notations

Symbol	Name	Units
ρ_o	Reference density	kg/m^3
ρ	Fluid density	kg/m^3
$\Delta\rho$	$(\rho - \rho_a)$	kg/m^3
U_x, U_y, U_z	Mean velocity in the axial, lateral and transverse direction respectively	m/s
u_x, u_y, u_z	Fluctuating velocity component in the axial, lateral and transverse direction respectively	m/s
P	Mean Pressure	atm
p	fluctuating pressure component	atm
U_m	Local maximum convection velocity at x/D = 11.425	m/s
T_s	Taylor microscale	s
T_{aL}	Integral time scale	s
T_m	Total measurement time	s
D	Jet diameter	m
r	Jet radius	m
Ri	Richardson Number	-
Re	Reynolds Number	-
θ	Fluctuating temperature	°C
Θ	Mean temperature	°C
σ	Standard deviation, RMS value of fluctuating part of the velocity component	m/s
g	Gravitational acceleration	m/s^2
τ	Lag time	s
$\rho(\tau)$	Auto-Correlation Function	-
ρ_{ab}	Correlation Coefficient	-
ϖ	Radial frequency	rad/s
q^2	Turbulent kinetic energy	m^2s^{-2}
t_o	Characteristic time of distribution: $(1/t_o)$ is the mean data rate	ms
N_p	Number of cross-products appearing in a given slot	-
N_t	Total number of data points in the time series	-
τ_{max}	Maximum lag time	s
$\Delta\tau$	Width of slot used in ACF estimations	s
γ	Intermittency factor	-
I(t)	Intermittency function	-
$P(\Delta\tau)$	Time Interval Distribution	s^{-1}

< > (angled brackets)	Conditionally averaged quantity
$\bar{}$ (Over-bar)	Time-average
$\bar{\bar{}}$ (Double-over-bar)	Coherent structure averaged over a given length
' (a prime)	Denotes the root-mean-squared value of the component

Acronyms

PSD	Power Spectra Density
ACF	Auto-Correlation Function
DNS	Direct Numerical Simulation
K-H	Kelvin-Helmoltz
LDA	Laser Doppler Anemometry
HWA	Hot-Wire Anemometry
TC	Thermocouple
TID	Time Interval Distribution
SNR	Signal to Noise Ratio
v-WAG	Velocity-Based Window Average Gradient
ω-WAG	Vorticity-Based Window Average Gradient
TID	Time-Interval-Distribution

1.0 Introduction

A moderator system of a CANDU[1] reactor operates ideally at 60-70°C. An abnormal rise in temperature may result in unwanted pressure build-up and damage to the surrounding fuel. Adequate safety analyses of certain accident scenarios require accurate numerical models for the prediction of the flow patterns and the associated temperature distributions in the calandria of the CANDU reactor. These predictions are performed using the numerical code MODTURC_CLAS[2]. An experimental program was recently designed and completed by the AECL[3] Fuel Channel thermalhydraulic group to provide sufficient data to validate the numerical code. The experiment consists of a hot axisymmetric turbulent buoyant jet and opposing cold jet issuing into an environment with a nominal temperature that is between the average temperature of the two jets. A three-component Laser Doppler Anemometer (LDA) instrument, an array of stationary thermocouples and a moving thermocouple were used to capture the three-dimensional flow and temperature fields.

---

[1] CANDU is a trademark of Atomic Energy of Canada Limited (AECL) for CANada Deuterium Uranium

[2] MODTURC_CLAS is a moderator circulation code which applies a buoyancy model

[3] Atomic Energy of Canada

Within the two opposing jets, the interface between two shear layers is subject to shear instabilities that may generate significant mixing and the development of large-scale structures. It is suspected that these structures play a significant role in influencing the temperature distribution of the flow.

The following report will investigate the adequacy of the current experimental measurements for the identification and characterization of the effects of coherent structures on the mean flow. The second chapter introduces the physical phenomenon and the governing equations of motion, which includes a literature review on the physical properties of a coherent structure and techniques for the identification of these structures. Chapter three will outline the experimental system and chapter four will formally introduce the tools used to characterize the experimental data and to identify coherent structures within the interacting shear layer. The discussion includes the following: 1) conventionally computed statistics for single point measurements, 2) the Window Averaging Gradient (WAG), 3) power spectral density estimation tools from irregularly sampled data, and 4) techniques for the qualitative assessment of LDA data. Chapter five will apply the tools developed in chapter four to assess the quality of the measurement data, characterize the flow system, and assess the applicability of the coherent structure identification tools under an irregularly sampled setting. Conclusions and recommendations will be provided in the remaining chapters.

2.0 Background

2.1 Governing Equations of the Turbulent Buoyant Jet

The dynamics of the flow for the turbulent buoyant jet are different from those of the turbulent jet and the buoyant jet systems. This finding can be understood since both the initial momentum and buoyancy fluxes are present in the flow (Rodi, 1982). To derive the mean dynamical governing equations for the horizontal axisymmetrical turbulent buoyant jet, a rectangular Cartesian coordinate system is used. Expressed in stress tensor notation, equations (2.1-1), (2.1-2) and (2.1-3) is given for the conservation of momentum, temperature and mass respectively (Turner, 1973).

(2.1-1) $$U_j \frac{dU_i}{dx_j} = \frac{-d\overline{u_i u_j}}{dx_j} - g\delta_{i3}\frac{\Delta\rho}{\rho_o}$$

(2.1-2) $$U_j \frac{d\Theta}{dx_j} = \frac{-d\overline{u_j \theta}}{dx_j}$$

(2.1-3) $$\frac{dU_j}{dx_j} = 0$$

where δ_{ij} is the Kronecker delta. In the above terms, i = 1 correspond to the axial direction, i =2 represents the lateral and i = 3 is the vertical component. To obtain these results, it was assumed that the pressure gradient was negligible, viscous effects are small and that the Boussinesq approximation was valid (Boussinesq, 1903). Furthermore, in equation (2.1-2), it was assumed that the

molecular diffusion of momentum and heat was assumed to be small relative to turbulent transport.

2.2 Coherent structures

There is persistent support that turbulent shear flows consist of large-scale, non-random structures with complex internal organizations in addition to small-scale, random, incoherent components. Visualization experiments at low Reynolds numbers by Brown and Roshko (1974) were the first to provide evidence for the existence of large-scale spanwise vortices, whereas Konrad (1977) and Breidenthal (1980) provided support of the existence of a streamwise aligned structure. The interactions of these structures with each other and the mean turbulence have been associated with the transport of heat, mass and momentum, entrainment, and aerodynamic noise generation (Clark et al., 1981). Although their importance is clear, no unique definition of a coherent structure exists. Many have chosen to define it based on vorticity concepts, whereas others have left the concept implicit, and only classify such structures as more dynamically significant than other scales in the flow (Hussain, 1986).

Certain physical properties are associated with these dynamically important structures and have been characterized by various researchers. These characteristics include the development, typical size, persistance, entrainment, turbulence production and the role in the transport of momentum. These characteristics will be discussed in the following section.

Physical Properties and Development

Much of the earlier knowledge of coherent structures came from observations obtained from flow visualization experiments. The size of a large-scale structure was observed to be on the order of the transverse length scale of the shear flow, whereas the intermediate-scale coherent structures, such as the secondary streamwise vortices, were usually noted to be on the order of the Taylor microscale (Hussain, 1986). In addition, the size of a coherent structure has also been found to scale to the structure's average survival distance. This distance was characterized by Clark et al. to be approximately one 'turn-over time', which is roughly equal to five times the local characteristic time scale (Clark et al., 1981).

Fundamental differences in the dynamics and development of the turbulent flow have been observed when shear and buoyancy forces are present. The development of coherent structures in a stratified flow under uniform shear (Piccirillo et al., 1997), under cross shear (Thorpe, 1968, Atsavapranee et al., 1997), and under a spatially accelerating shear layer (Pawlak et al., 1998). Atsavapranee et al. (1997) used a two-dimensional temporal mixing layer to generate a velocity shear, and investigated the effects of stratification on coherent structure development. They used a Reynolds[4] number of 2200 and a

[4] $Re = \Delta U\delta/\nu$ where ΔU = difference in velocity of the two shear layers, δ = max. velocity-gradient thickness, and ν = kinematic viscosity.

Richardson[5] number *Ri* in the range of 0.01 to 0.20. The results for the stratified case suggests that the primary vortex structures were developed due to instability caused by the shearing of two layers and observed to remain prominent up to a *Ri* of 0.16. However, the most striking result was that Richardson numbers in the range of 0.043 to 0.16 led to a four-fold reduction in the size of the large-scale vortices, and a two-fold reduction in their fluid entrainment ratio was observed. These results were tightly coupled since the reduction in the maximum vortex size attained at the climatic state resulted in significantly less entrainment of denser fluid into the smaller vortices. Consequently, the mixing efficiency was also reduced.

Piccirillo et al. also found evidence that buoyancy suppressed the development of the shear flow. Both the Reynolds shear stress and the turbulence kinetic energy was shown to be significantly reduced with an increasing Richardson number (Piccirillo et al., 1997). These conclusions were also found in a Direct Numerical Simulation *DNS* by Roher (1988) who studied experiments with uniform shear and stable stratification. Roher was able to show that the effects of buoyancy on the turbulence were primarily in the reduction of the turbulence production.

Other complex phenomena due to buoyancy include the counter gradient heat fluxes occurring under non-sheared flows (Thoroddsen et al., 1996).

---

[5] $Ri = g\Delta\rho\delta/\rho_a(\Delta U)^2$; g=gravitational acceleration, $\Delta\rho$= difference in density, ρ_a = avg.density

Furthermore, buoyancy forces were also shown to affect the energy cascade process. Anisotropy increased with an increasing Richardson number as buoyancy forces dominated the small-scale turbulence and suppressed the amount of spectral energy transfer from large to small scales. Piccirillo et al. observed this phenomenon in both their experiments with stratification with uniform shearing and their stratified experiments without uniform shearing. Clearly, stratification of the flow resulted in an intense stabilizing effect and thus a suppression of vertical motions of the vortical structures. However, Piccirillo et al. note that although buoyancy preferentially suppresses vertical velocity energy, less suppression for lateral or streamwise velocity turbulent energy was observed (Piccirillo et al., 1997).

The ability to transport momentum is another signature property of all coherent structures. Various works exist that apply conditional-sampling techniques to quantify a coherent structure's contribution to the transfer of momentum and to the turbulent kinetic energy (Bonnet et al., 1998, Bisset et al., 1990, Auburn et al., 2002). Studying from a plane, incompressible, fully developed turbulent two-stream mixing layer, Bisset et al. noted that coherent structures were able to contribute substantially in the most turbulent region of the flow that was up to 40% of the Reynolds shear stress. The contribution to the turbulent energy was also noted to be significant in the transverse direction with a value of approximately 40%. In contrast, the contribution from the axial component was expectedly lower at only 10%.

Methods for the Identification of Coherent Structures

Various techniques currently exist for the identification of coherent structures (Bonnet et al., 1998, Bonnet et al., 1993). These techniques include vorticity-based conditional sampling (Hussain, 1986), vorticity- based conditional sampling using the Window Averaging Gradient (ω-WAG) (Bisset et al., 1990), velocity-based conditional sampling using Window Averaging Gradient (v-WAG) (Bisset et al., 1990), wavelet (Kevlahan N. et al., 1993), pattern recognition tools (Mumford, 1982, Ferre et al., 1993), proper orthogonal decomposition (POD) (Aubry et al., 1988, Glauser and George, 1987), pseudo-flow visualization (PFV) (Glauser and George, 1992) and topological concept-based methods (Perry, A. et al., 1986).

Each structure identification technique exhibits individual strengths and weaknesses and can be dependent on the several factors such as the desired information sought, definition of a coherent structure or the experimental and numerical capabilities available to the experimenter. These differences were attempted to be resolved in a recent benchmarking test using various techniques based on the same mixing layer database. The ability of each detection scheme to identify a coherent structure was assessed and the results are presented in figure 2.3-1 (Bonnet et al., 1998).

The results of the comparison clearly indicate that the velocity-based detection that includes 1) wavelet, 2) DCS, 3) POD, 4) v-WAG provided very similar detection sequences. It is clear from the results that the v-WAG algorithm detects structures at a slightly different location than that of the wavelet, DCS and POD. This finding can be understood since the v-WAG scheme is triggered during sharp transverse gradients that physically correspond to regions of the saddle point that appear between structures. In contrast, vorticity-based schemes search for points of maximum spanwise vorticity, which occur at the centres of the vortex. In addition, it was interesting to observe that the v-WAG was also capable of missing a detection position as shown by the five-point star in figure 2.3-1. The wavelet, DCS and POD in comparison were all capable of detecting five of the five possible structures. However, DCS and POD clearly proved to be the most consistent with the visual data, whereas the wavelet scheme appeared to detect both the saddle points and the core of the vortex structure.

The results of the benchmark tests suggest that the detection of the coherent structures appears to be most successful for techniques that utilize multi-point sensors (DCS, POD, PFV). These sensors have been shown to be simpler, less ambiguous and more reliable to the visual outputs. In addition, an assessment of the ideal location for the detection of vortices can easily be achieved.

However, the luxury of multi-point measurements is not available in the present experiment, as only single-point LDA velocity measurements were taken. Regardless of the shortcoming, the success of the wavelet and v-WAG schemes in the benchmark test provided support that single-point measurement experiments are still capable of detecting and analyzing the coherent structures of the turbulent flow. A v-WAG was applied in this report and a detailed discussion of the methodology will be given in section 4.2 with the presentation of its results provided in section 5.2.

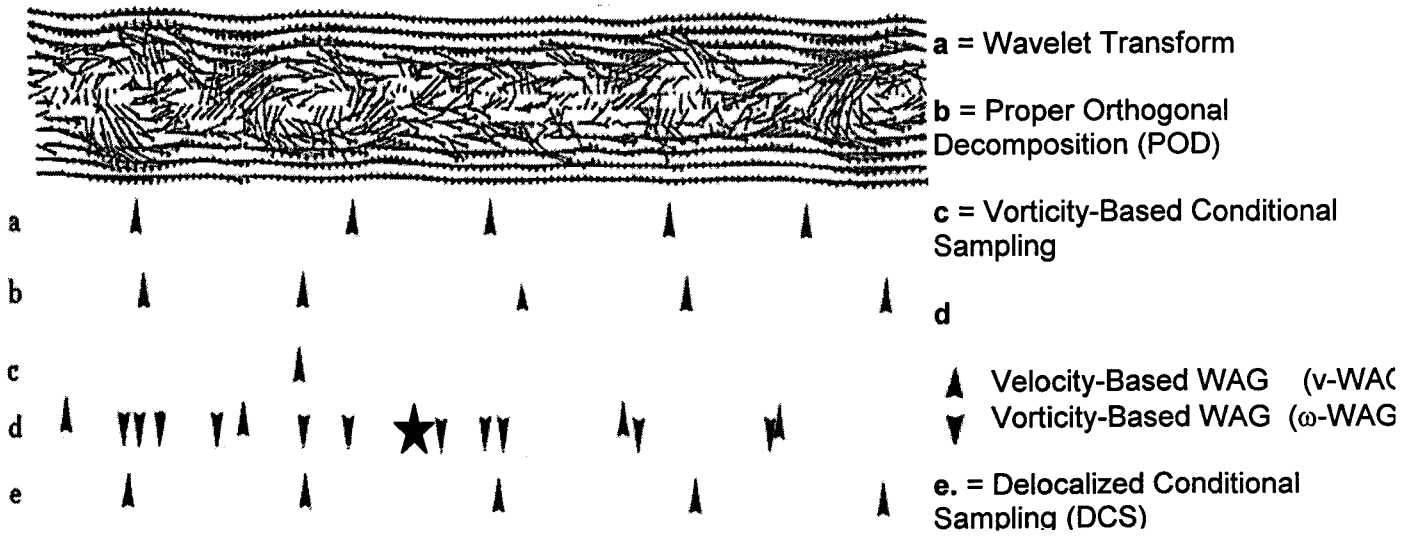

Figure 2.3-1 A summary of the benchmark test to assess an identification scheme's ability to detect the passage of a coherent structure in a plane, incompressible, fully developed turbulent two-stream mixing layer [Illustration taken from Bonnet et al., 1998].

3.0 Experimental

3.1 Experimental Equipment and Procedure

The experimental program was conducted by the AECL Fuel Channel Thermalhydraulics group and completed at Chalk River Laboratories. Six experiments were completed labeled B1 to B6. The data set used in the analysis of this report was experiment B4 since the test conditions resulted in the most significant buoyancy effects. The experimental tests were completed over a period of several weeks.

Apparatus

The two turbulent jets experiment was completed in the buoyancy test facility shown in figure 3.1-1. This buoyancy test facility is a component of the moderator test facility and is illustrated in figure 3.1-2.

Within the buoyancy test facility, the loop instrumentation includes flow meters and thermocouples to measure the fluid flow rates and temperature respectively. Their positions are indicated in figure 3.1-2. The temperature measurements allowed proper monitoring of the inlet jet temperatures that were measured upstream of the three-way valves, while all pipes leading into the test section were insulated to minimize any heat loss. The estimated measurement uncertainty for the flow meters and thermocouples is given in table 3.1-1

The schematic of the buoyancy vessel used in the experiment is given in figure 3.1-3 with all dimensions given in the figure. The buoyancy vessel was a semi-cylinder with two opposing round nozzles (52 mm inner diameter) at the positions indicated in figure 3.1-3.

The illustration indicates the existence of a static mixer (model FMX7321, manufactured by OMEGA) and a honeycomb flow straightener (6.4 mm cell-size) used to reduce the bends upstream of the static mixers. Four outlet ports were situated at the top of the vessel and in the four corners. The temperature at these outlet ports was measured to monitor and ensure a uniformly distributed vessel. Vortices existing near the outlet ports were eliminated using a combination of honeycomb flow straighteners and anti-ventilation plastic plates (Khartabil, 2001a).

Measurement Systems and Locations

The velocity measurements were taken from a three-component Laser Doppler Velocimetry (LDV) system. The recording of velocity measurement was set to record only when the three velocity components were available. The implications were that the data acquisition was irregular. The mean data rate varied depending on the position of the flow. More details on the mean date rate are given in section 5.1.1.

The LDV velocity measurement locations, as specified by OPGI[6], are given in figures 3.1-4(a) for the XZ-plane (side-view) and 3.1-4(b) for the XY-plane (top view). The three-dimensional profile of all the LDV measurements is given in figure 3.1-5, which corresponds to the points presented in 3.1-4. Measurements at the exit of the hot jet are seen more clearly in figure 5.1.1-4 and denoted by the solid dots.

Within the buoyancy vessel, temperature measurements were taken from 100 fixed stainless steel thermocouples with an approximate diameter of 0.9 mm. The sampling rate 0.2 Hz was used. The measurement locations are given in figures 3.1-6 and 3.1-7. The sign convention used in this report is consistent with that shown in figures 3.1-6 and 3.1-7. Additional thermocouple measurements were placed 6.0 cm above the measurement volume of the LDV system when taken at the jet exits, and 4.0 cm above the measurement volume at the remaining locations. Figure 3.1-8 is given to illustrate the measurement positions of the moving thermocouple. The sampling frequency was again 0.2 Hz. The estimated measurement uncertainty for the temperature measurements is given in table 3.1-1.

Data Acquisition and Storage

Two data acquisition and storage systems were used. All loop-measurements (thermocouples and flow rates) were obtained using a PC-based data acquisition

---

[6] OPGI is the trademark name of Ontario Power Generation Incorporated

system that uses PARAGON TNT software (Lachance, 1999). The LDV data were collected using the TSI FIND software package (Lee, 1999).

Experimental Procedure

The experimental procedure is found in greater detail in (Khartabil, 2001b) but a summarized form is reproduced and given in the Appendix A. The experimental test conditions were established to ensure significant buoyancy effects were observed. The test conditions are given in table 3.1-2 where the Reynolds number is defined based on the jet diameter and given as

$$\text{Re} = \frac{\rho u D}{\mu} \tag{3.1-1}$$

where ρ is the fluid density, u is the exit velocity, D is the jet diameter, and μ is the fluid viscosity.

Table 3.1-1 Summary of the Measurement Uncertainty (Khartabil, 2001c)	
Instrument	***Measurement Uncertainty***
Flow-meters were factory-calibrated	±1.4%
Loop Thermocouples	±0.3^{0}C (95% Confidence level)
Vessel Thermocouples**	±0.4^{0}C

Table 3.1-2: Experimental Test Conditions (Khartabil, 2001c)	
Experimental Test	B4
Flow Rate [kg/s]	0.5
Pipe Diameter [m]	0.052
Area [m^2]	0.002123717
T_{Cold} [^{0}C]	30
Density [kg/m3]	995.7
Viscosity [kg/ms]	0.00079553
Velocity[m/s]	0.236453054
Re (Cold jet)	1.54E+04
T_{Hot}[^{0}C]	50
Density [kg/m3]	988.7
Viscosity [kg/ms]	0.0005494
Velocity	0.238127
Re (Hot Jet)	2.23E+04

** calibrated indirectly by establishing isothermal conditions in the vessel and comparing their readings to the readings of the calibrated loop thermocouples.

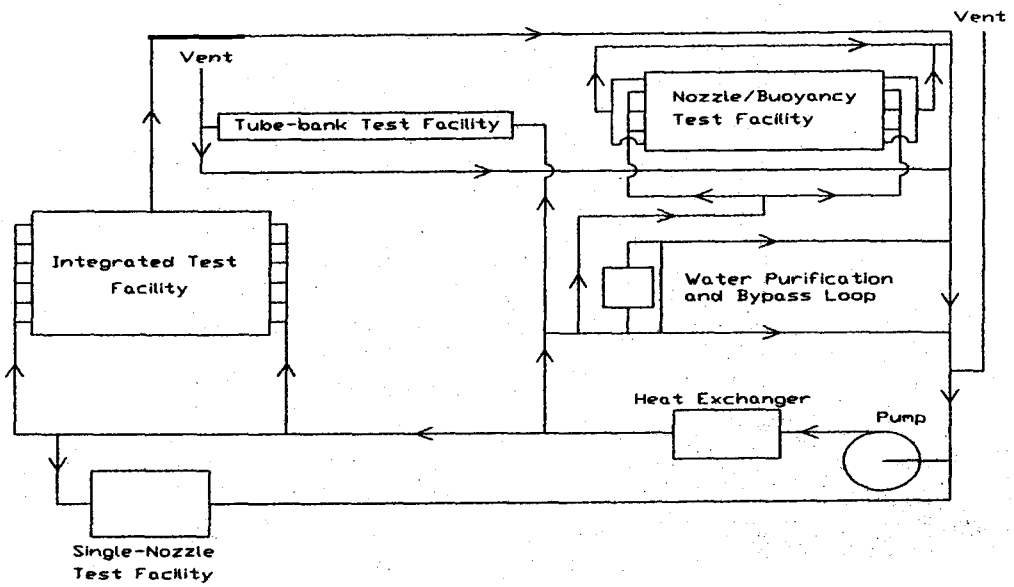

Figure 3.1-1 Buoyancy test Facility Flow Diagram [Taken from: Khartabil, 2001a]

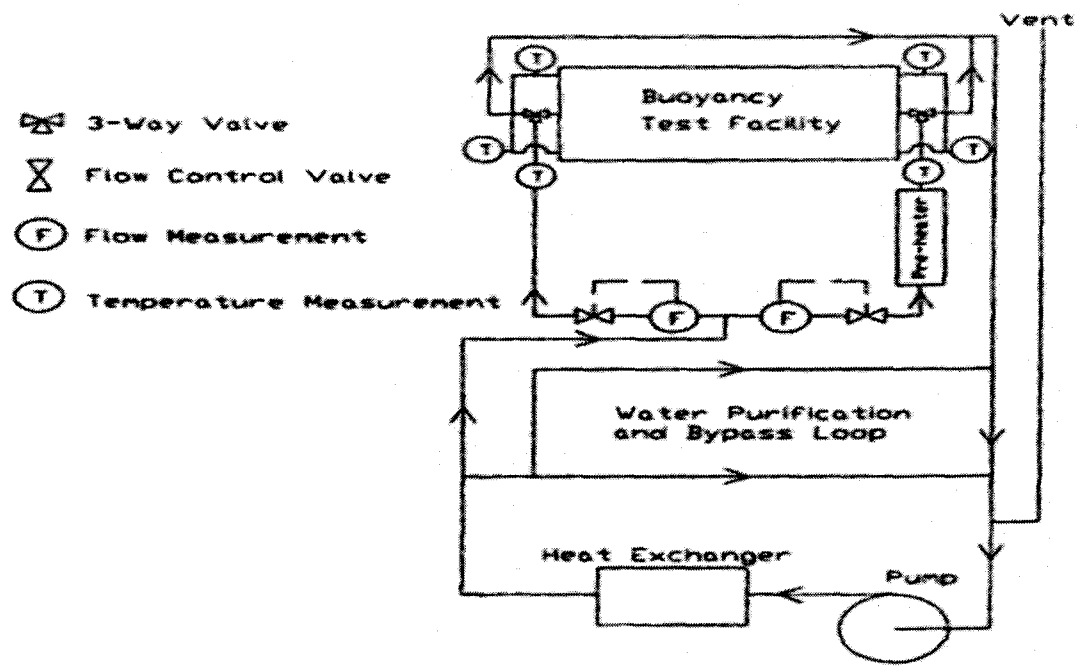

Figure 3.1-2 Modified Moderator test Facility Flow Diagram [Taken from: Khartabil, 2001a]

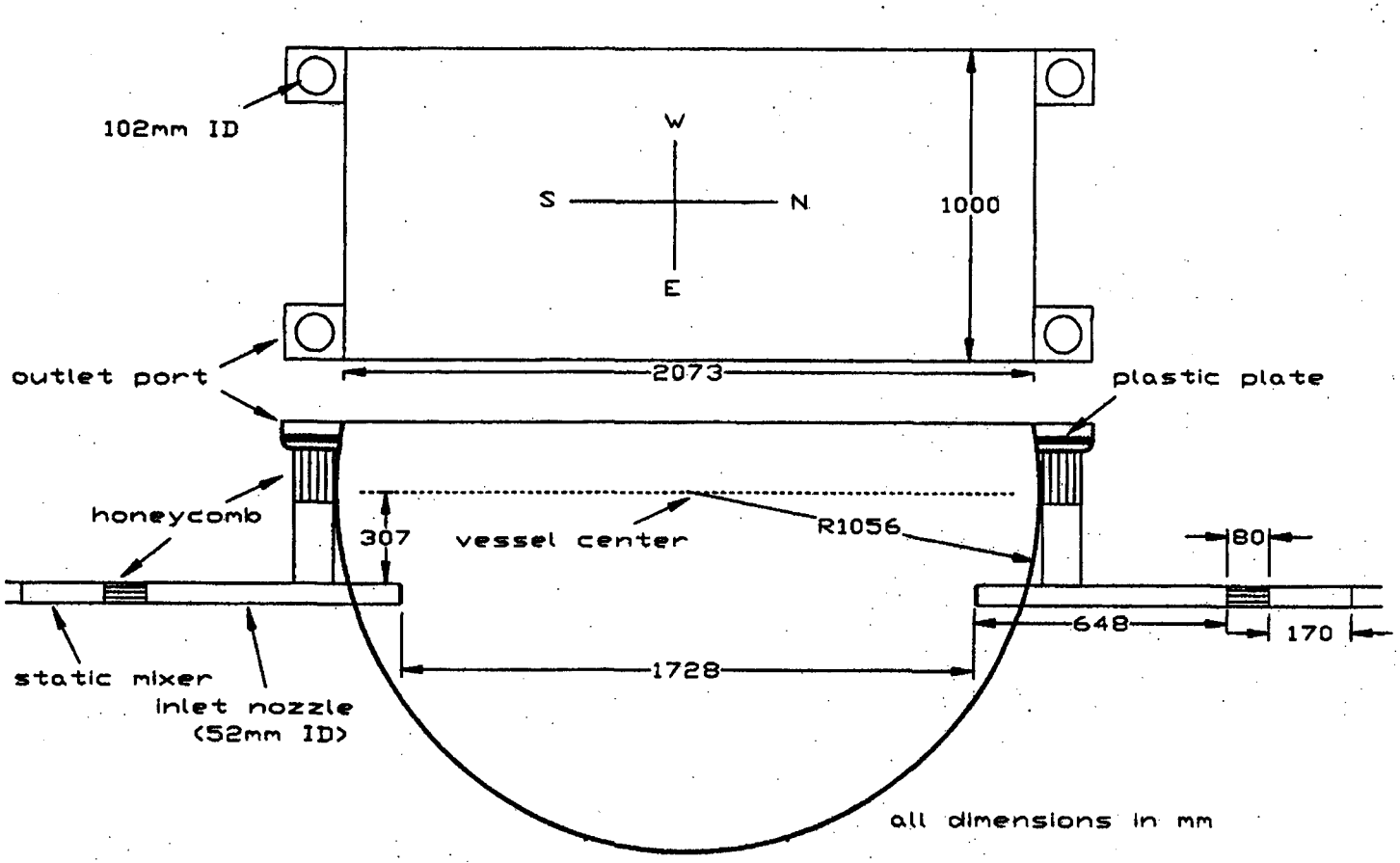

Figure 3.1-3 Buoyancy Vessel [Taken from: Khartabil 2001a].

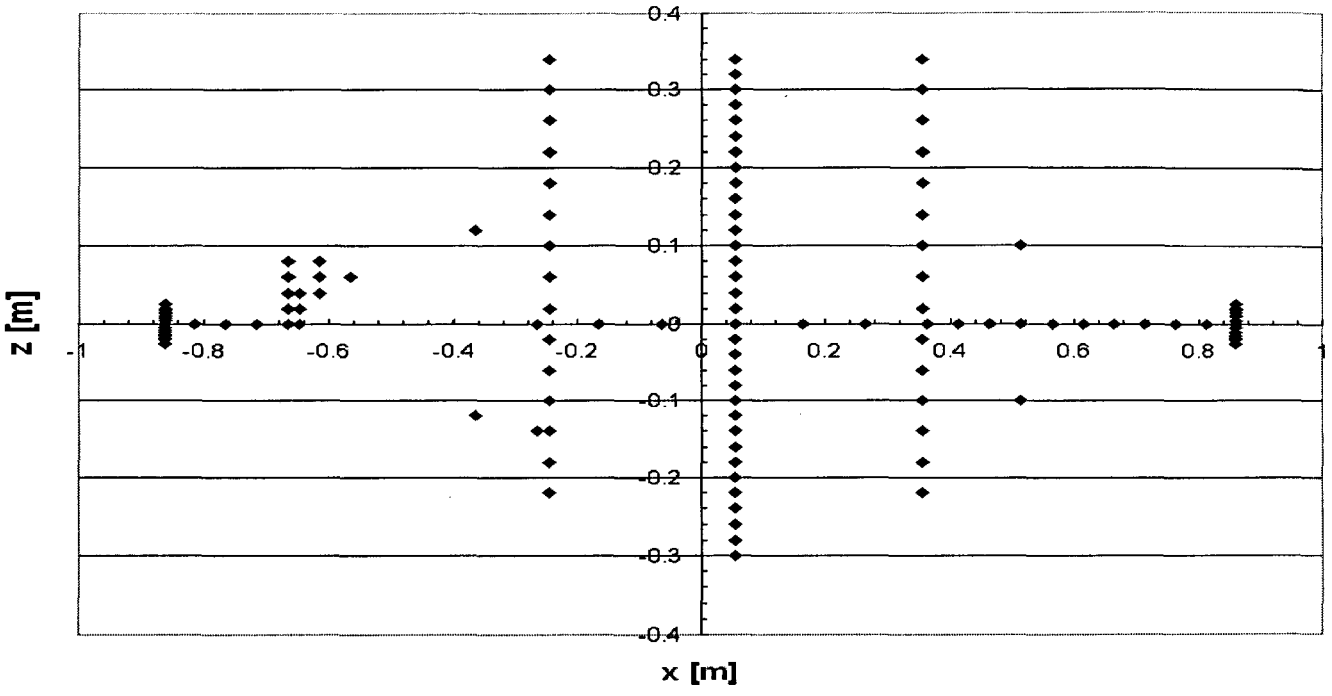

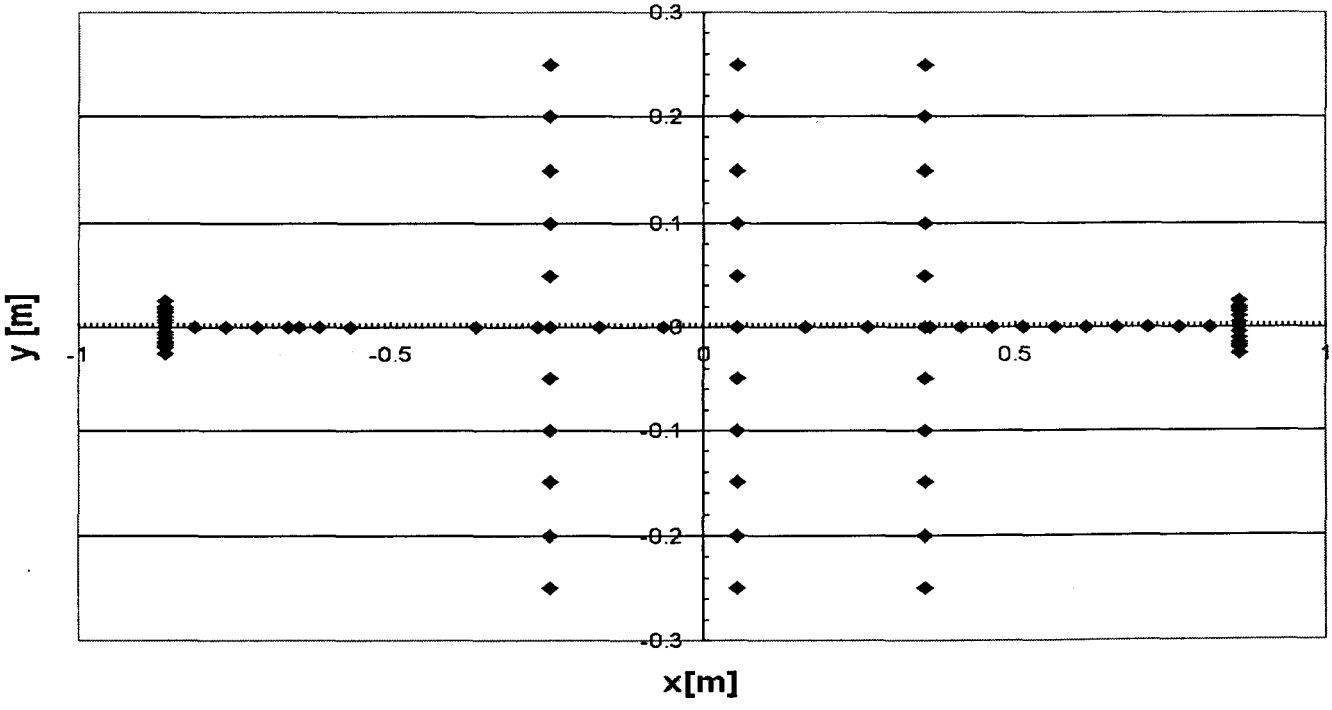

Figure 3.1-4 (a) Side-view (b) Top-view. The position of the hot jet is at x= -0.861 m. The cold jet is at x=+0.861 m. The corresponding three-dimensional view of all the measurements is given in figure 3.1-7. .

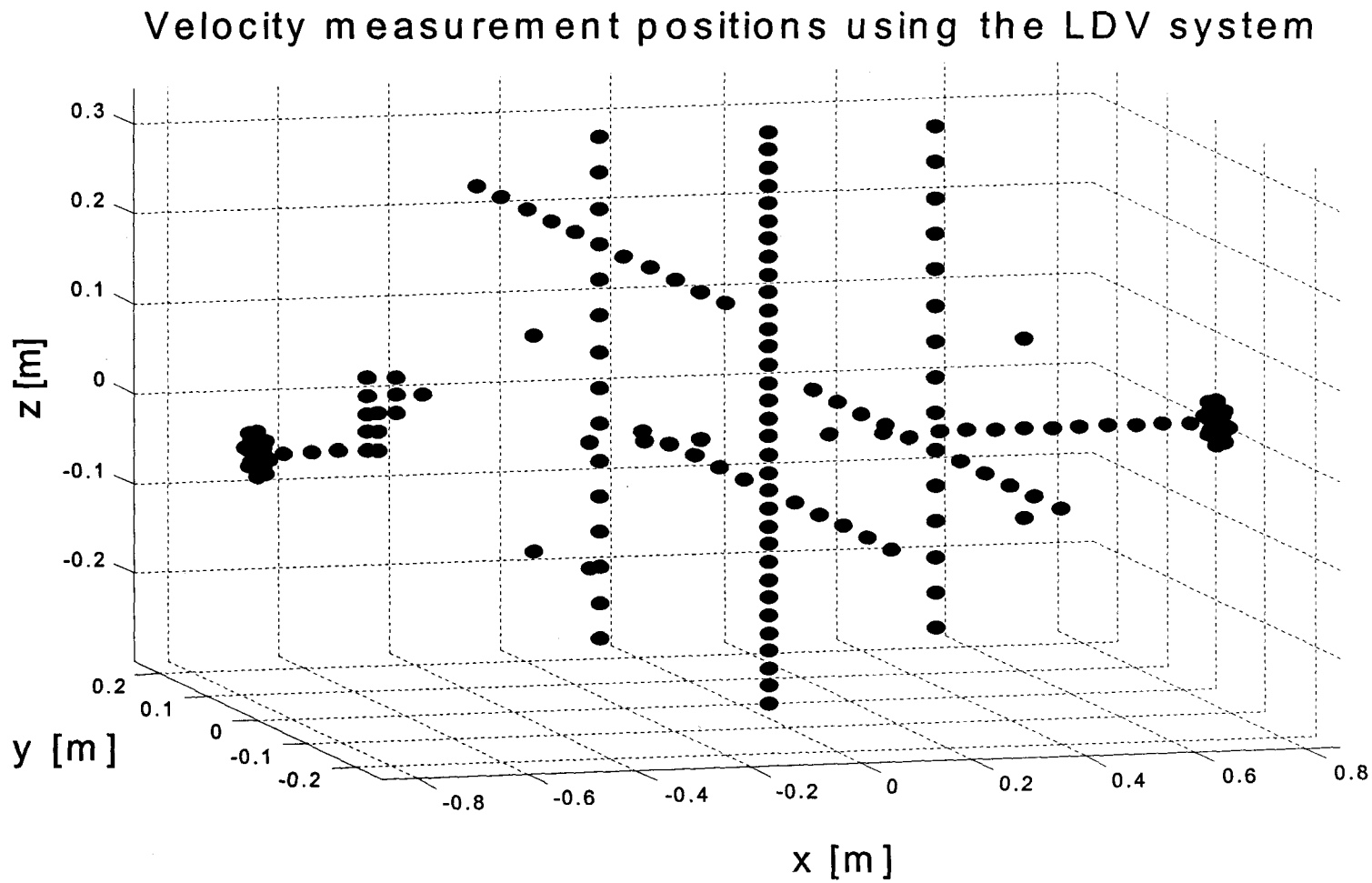

Figure 3.1-5 LDV velocity measurements taken in the experiment. These measurement points correspond to the measurement points given in figure 3.1-6. These measurement points were ***not*** taken simultaneously, but were completed over a period of several weeks. The hot jet is at x= -0.861 m.

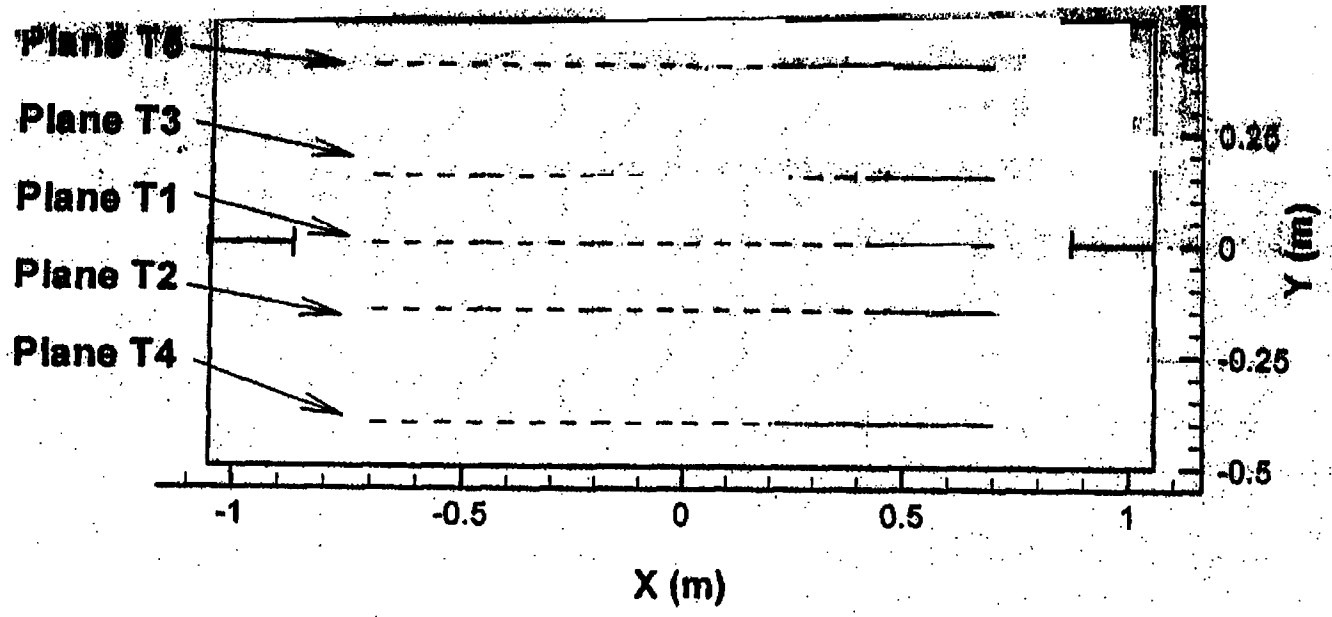

Figure 3.1-6 Fixed thermocouple planes [Taken from: Khartabil, 2001a].

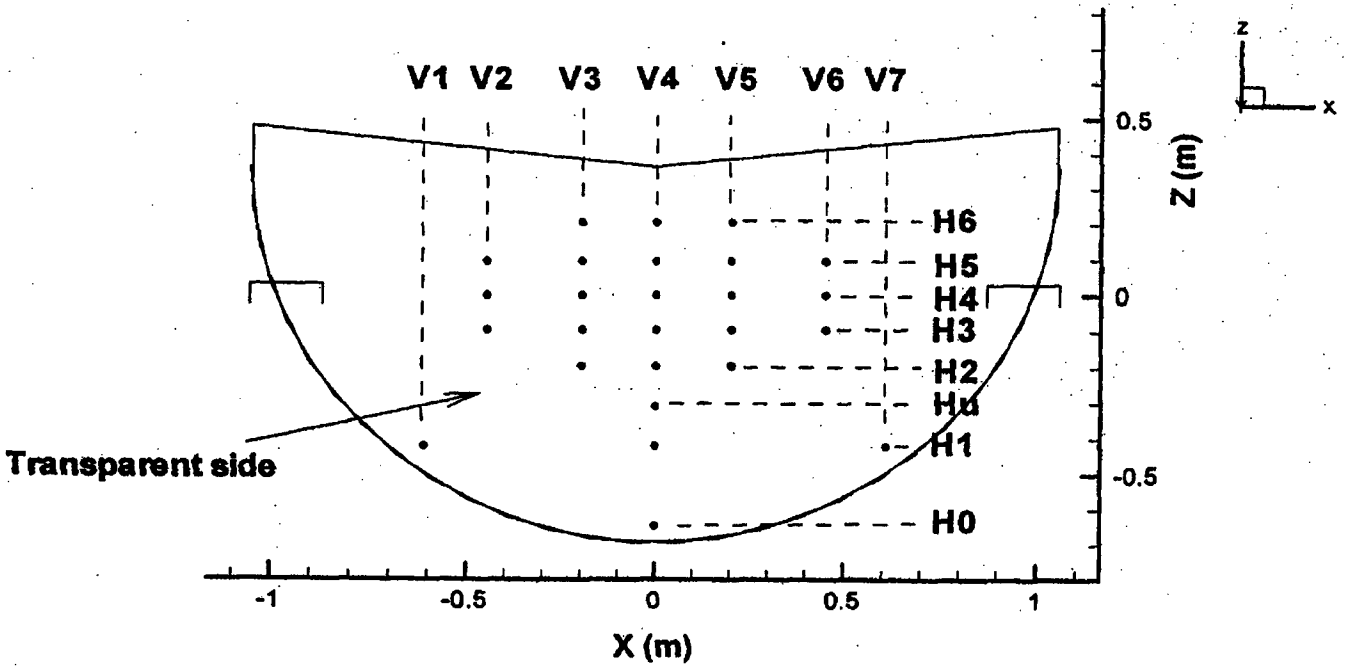

Figure 3.1-7 Location of the fixed thermocouples used in the buoyancy test vessel. Support wire matrix used to locate the fixed thermocouples [Taken from: Khartabil, 2001a]

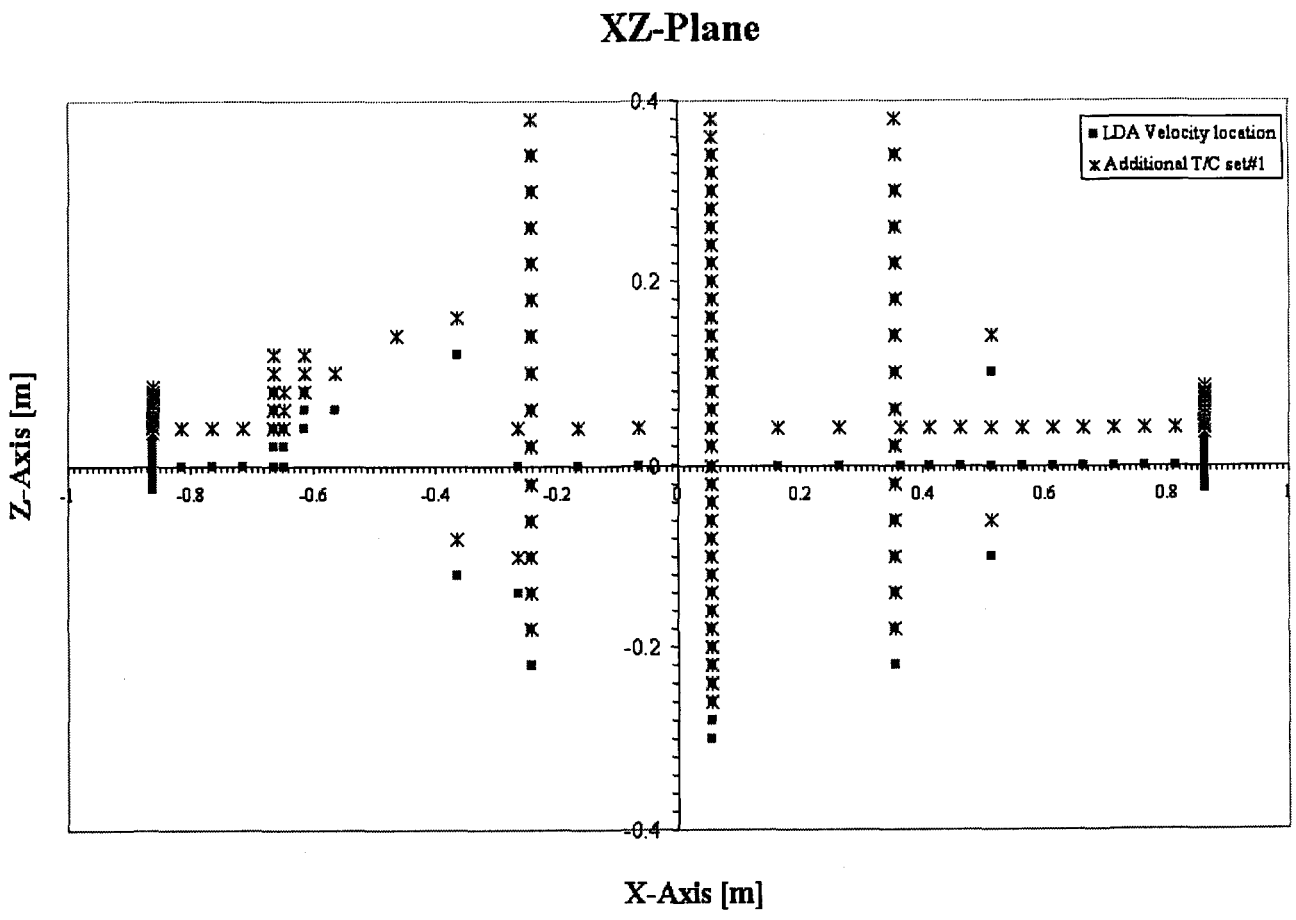

Figure 3.1-8 Location of the additional thermocouples.

4.0 Data Processing and Tool Development

4.1 Conventional Statistics for Single Point Measurements

Assuming the process is statistically stationary, the instantaneous $\widetilde{a}(t,x)$ signal is decomposed into a mean *A(x)* and a fluctuation component a(t,x) and given as the following

(4.1-1) $$\widetilde{a}(t,x) = A(x) + a(t,x)$$

where $\widetilde{a}(t,x)$ corresponds to any physical quantity such as pressure, velocity or temperature. A statistically stationary process implies that the time record used to compute the statistical average is long enough to contain the largest integral scales (George, 1979). The integral scale given in (4.1-2) can be obtained from the intersection with the time delay axis of $\rho(\tau)$ which is the auto-correlation function defined in (4.1-3).

(4.1-2) $$T_{aL} = \int_0^\infty \rho(\tau) d\tau$$

(4.1-3) $$\rho(\tau,x) = \frac{\overline{a(t,x)\cdot a(t+\tau,x)}}{\left[\overline{a^2(x)}\cdot\overline{a^2(x)}\right]^{1/2}}$$

where the over-bar in the above equation denotes a time average (Tennekes et al., 1972). The discrete temporal averages is found in the following way for an instantaneous quantity that requires velocity bias correction

(4.1-4) $$A = \frac{\sum_{i=1}^{N} \tilde{a} \cdot \xi}{\sum_{i=1}^{i=N} \xi}$$

where ξ is the bias correction factor[7] (ξ=1 for no bias correction) and N is the total number of samples that satisfy some stability criteria. As given in (4.1-1), the fluctuating component of an instantaneous value is computed by the following:

(4.1-5) $$a = \tilde{a} - A$$

The fluctuating component is used to measure the variability of the data set about the mean quantity *A* using the variance defined as:

(4.1-6) $$\sigma^2 = \overline{a^2} = \left(\frac{\sum \tilde{a}^2 \xi}{\sum \xi} - A^2 \right)$$

The standard deviation (or root-mean squared (RMS)) is obtained from the variance given by the following:

(4.1-7) $$\sigma = \overline{a^2}^{1/2} = a'$$

where the prime is used for convenience to denote the RMS quantity.

The correlation between two fluctuating components plays an essential role in the study of turbulence. An adequate measure of the interdependence of two variables is shown through the correlation coefficient given as:

---

[7] The bias correction factor used in this report was the transit time (Tummers et al., 2000). Minor differences were observed between the TSI computed values and values from the statistical tools developed in this report. The difference is suspected to be due to an error in the TSI software.

(4.1-8) $$\rho_{ab} = \frac{\overline{a \cdot b}}{\left[\overline{a^2} \cdot \overline{b^2}\right]^{1/2}}$$

where $\rho_{ab} = \pm 1$ signifies *a* is perfectly positively or negatively correlated with *b*. Note, $\rho_{ab} = 0$ suggests no correlation. Application of the temporal auto-correlation function allows one to extract important time scales. The integral time scale has already been introduced and given in (4.1-2) and quantifies the average time over which the signal remains correlated. This value physically corresponds to a measure of the time scale of a large-scale structure to be advected past a measurement position (Tennekes et al., 1972). A measure of the small scale turbulence is given by the Taylor microscale as shown below (Tennekes et al., 1972):

(4.1-9) $$T_{sa}(x) = \left[\frac{2\overline{a^2(x)}}{\left(\overline{da/dt}\right)^2(x)}\right]^{1/2} = \left[\frac{2}{-\rho''_a(0,x)}\right]^{1/2}$$

Other statistical properties that are of interest include the skewness and kurtosis (flatness factor) given in equation (4.1-10) and (4.1-11) respectively. The skewness provides a measure of asymmetry, whereas the kurtosis quantifies the shape (flat or peaked) of the distribution (Tennekes et al., 1972).

(4.1-10) $$S = \frac{\overline{a^3}}{\sigma^3}$$

(4.1-11) $$K = \frac{\overline{a^4}}{\sigma^4}$$

4.2 The Window Average Gradient (WAG) Methodology

The algorithm applied in this report for the detection of coherent structures is the Window Average Gradient (Bisset et al., 1990). The procedure requires computing the difference between the average data values of two window halves by moving a window of size (2τ +1) data points through the data set from j=1,2,3,....N, where N is the total number of data points. The Window Average Gradient coefficient at point j as determined by the following:

(4.2-1) $$WAG_j = \frac{1}{2\tau}\left[\sum_{i=j+1}^{j+\tau} u_z - \sum_{i=j-\tau}^{j-1} u_z\right]$$

The design of the WAG algorithm results in a preference to detect sharp transverse gradients that generally occur in the region of the saddle points (Bisset et al., 1990, Bonnet et al., 1998). The saddle point corresponds to regions of large entrainment of fluid. Physically, this corresponds to regions in which fluid is entrained due to the straining (stretching) motions at the interface of the shear layer. Thus, a large vertical velocity gradient is expected. The algorithm detects these regions if the computed value of (4.2-1) exceeds a given threshold.

Ensemble Statistics

Assuming the frozen Taylor hypothesis[8] holds, the local length and time scales can be related to the convection velocity and are given as the following:

---

[8] The frozen Taylor hypothesis states that when the relative convection velocity U_m is constant and much larger than then turbulent fluctuation, one can assume that the flow essential consists of a series of a

(4.2-2) $$< L >= t \cdot U_m$$

The algorithm employed in this work passes a band pass filter through the data to retain only the properties of a coherent structure of a specific size. For every triggered realization, the ensemble statistics for a specific length scale were computed. The angle brackets will be used to denote a conditional averaging procedure.

The fluctuating component of an instantaneous physical quantity is also decomposed as

(4.2-3) $$a = \tilde{A} - A$$

The phase-averaged coherent values for a given structural size can be obtained by

(4.2-4) $$< A >_k = \frac{1}{(\xi_{jm+k})} \sum_{m=1}^{n} \xi_{jm+l} \cdot A_{jm+k}$$

where *n* is the number of identified detections, *k* is the relative position from the maximum value at jm (Bisset et al., 1990) and ξ_{jm+k} is the bias correction for the velocity measurement at jm+k. The phase-average of structural dimension starting from position k_1 to k_2 is then given as follows

(4.2-5) $$\overline{\overline{< A >}} = \frac{1}{(k_1 + k_2 + 1)} \sum_{-k_1}^{k_2} < A >_k$$

The Reynolds stresses are computed from the instantaneous fluctuating quantities *a* and *b*, which for example, may correspond to u_x and u_z . Using an analogous derivation

---

'frozen' pattern of homogeneous turbulence that is convected past the measurement position (Reynolds, 1974).

and assuming that the correlation between coherent and the random, incoherent contributions are null, then the Reynolds stresses are defined as follows

(4.2-6) $$ab = < a_c b_c > + a_r b_r$$

Again, for any specified structural dimension starting from k_1 and ending at k_2, the structural average for the coherent part of the Reynolds stress is computed using (4.2-5), where *A* in (4.2-5) is substituted with either the second term or third term in (4.2-6).

The square wave function is used to define the proportion of time that any given measurement sensor 'sees' a coherent structure and given as:

(4.2-7) $$I(x,t) = \begin{cases} = 1 \text{ if coherent structure is passing} \\ = 0 \text{ otherwise} \end{cases}$$

Thus, the probability that a given fluid has a coherent structure passing is given by the intermittency factor defined by the time average of (4.2-7) and given as

(4.2-8) $$\gamma = \bar{I} = \frac{1}{T_s} \int_{t=0}^{t=T_s} I(x,t)dt$$

where T_s is the total sampling period. Thus, any of the conventionally computed moments are recovered by using the relation:

(4.2-9) $$A = \gamma < A_c > -(1-\gamma)A_r$$

To quantify the contribution that a coherent structure has to turbulent energy and the transfer of momentum can be completed as follows (Bisset et al., 1990, Bonnet et al.,

1998). The contribution that a detected structure makes to the u_i component of turbulent energy can be obtained from the following ratio,

(4.2-10) $$\frac{\overline{\overline{<u_i>}}}{\overline{\overline{<u_i^2>}}}$$

where i corresponds to either x, y or z.

The contributions that a coherent structure makes to the transfer of momentum from the Reynolds normal and shear stresses can be determined from equation (4.2-11) and (4.2-12) respectively.

(4.2-11) $$\frac{\overline{\overline{\gamma \cdot <u_i^2>}}}{\overline{u_i^2}}$$

(4.2-12) $$\frac{\overline{\overline{\gamma \cdot <u_i u_j>}}}{\overline{u_i u_j}}$$

Modifications for the WAG Algorithm for Irregularly Sampled Data

Difficulties were experienced in applying the traditional WAG algorithm under the irregularly sampled data set. For example, detecting the typical length scale of a coherent structure was affected due to 1) the irregular sampling, 2) low data rate and 3) noise in the data. Large delays between data sampled result in an ambiguous estimate of the time duration of a passing structure. To overcome this problem, the filtering process for one particular length scale was not completed, but a filtering based on a specified range was applied. The results of the distribution were then used to assess

the (*approximate)* dominant length scale that appeared for the measurement location. The approximate length scale was suggested to be typically 10% to 30% of the jet diameter. Although this percentage is small, it does not appear to be unreasonable as discussed in section 2.2 where it was suggested that the typical size of a coherent structure decayed with distance from the origin of development with a survival time in the order of five times the characteristic time scale (Clark et al., 1981). In addition, the typical size of the coherent structure was also noted to decrease significantly due to stratification effects (Atsavapranee et al., 1997). Thus, it is not unreasonable to believe that based on the position of the measurement, that the size of the detected structure was much smaller than the typically defined 'large-scale' coherent structure.

In addition, a slight modification to the WAG algorithm was implemented in this report. Bisset et al. (1990) detected abrupt changes in one vertical direction only, and for ideal signals with minimal noise, this approach appears to provide excellent results. However, issues of signal dropouts ('false-alarms') and noise complicate the detection sequence and may result in very low detection sequences. Low detection sequences are not reliable since they may include a significant amount of information related to the noise of the signal rather than to the coherent structure itself. Thus, to improve the detection algorithm, the detection region was allowed to trigger when either an abrupt upward velocity gradient or an abrupt downward velocity gradient was detected.

4.3 Estimation of the Auto-Correlation Function (ACF) and Power Spectral Density (PSD) from Irregularly Sampled Data

Due to the irregularly sampling nature and the velocity bias[9] inherent in the LDA data, traditional time series analysis tools could not be employed in the estimation of the power spectra of the data. Various efforts to estimate the Fourier Transform of an irregular sampled data set have been proposed using the traditional slotting correlation techniques (Mayo, 1974, 1978). Various improvements have been developed since then and discussed in (van Maanen et al., 1996, Benedict et al., 2000, Nobach et al., 1998). The algorithms were tested and discussed in a recent benchmarking experiment (Benedict et al., 1998).

Based on the results of the benchmarking experiment, tools were developed in the following project to obtain the Auto-Correlation Function (ACF) and the Power Spectral Density (PSD) using techniques of the local normalization with fuzzy correlation algorithm (van Maanen et al., 1996, Nobach et al., 1998). The details of the algorithm can be found in appendix B.

---

[9] The velocity estimate is correlated to the data rate

4.4 Assessment of the LDA Data Quality

Noise affects an LDA system in a complex manner where the level of noise is roughly two orders of magnitude greater than that of standard Hot-Wire Anemometer (HWA) techniques (van Maanen, 2000). The general practice in quantifying the quality of the LDA data is through the signal-to-noise ratio (SNR) and discussed by Menon et al. (1991), Adrian (1978), Shinpaugh et al. (1992) and Lehmann et al. (1997). The choice of method to compute the SNR value various and to the author's present knowledge, no unique definition of the SNR has yet to be agreed upon. This implies that the form of the SNR can be easily manipulated. Thus, only a qualitative description of the LDA measurements are presented in this report and given in section 5.1.1. The assessment of the data is made relative to the ideal Time-Interval Distribution (TID), which for an LDA system takes the form of a Poisson distribution given as (Erdmann et al., 1976, Feller, 1966)

(4.4-1) $$P(\Delta t) = \frac{1}{t_o} e^{\frac{-\Delta t}{t_o}}$$

where t_o is the characteristic time of distribution, $1/t_o$ is the mean data rate and Δt is the slot width. The description to obtain a TID profile is described in appendix C.

Deviations from the ideal distribution suggest possible problems and summarized in table 4.4-1. Each deviation has been shown to exhibit a signature profile and provides a visual aid in qualitatively diagnosing the LDA data (van Maanen, 2000).

Table 4.4-1: A summary of the possible deviations from the ideal TID distribution and its possible sources with suggested solutions (van Maanen, 2000).	
TID signatures	**Source of Deviation**
1. No data in short time intervals	Dead-time of the data processor (only if the distribution shows a sharp boundary)
2. The TID shows a 'hump' for short time intervals.	Uncertainties in the arrival time estimators
3. The TID shows a 'valley' near the characteristic time of TID (t_o).	Velocity bias (increases proportionately to the turbulence intensities)
4. A small number of bins do not contain data.	Uncertainty in the arrival time and round-off errors of the clock
5. A large number of bins do not contain data.	Significant round-off errors of the internal clock
6. A comb like structure	Computer accuracy to store arrival time is poor and noticeable for systems under long experimental times.

7. Sharp peaks at short time intervals and a linear fit that is below the value of 1.	Multiple validation ▪ Noise results in the modulation of the Doppler signal, that is, it fools the LDA system to think that more than one particle is present in the measurement system

5.0 Results and Discussion

The experimental data set B4 will be used in the analysis of the following sections. The experimental measurement positions for the LDA data are given in figures 3.1-4 and 3.1-5. In addition, the positions of the temperature measurements are found in figures 3.1-6 and 3.1-7. The figures presented in the following sections are normalized by the jet diameter *D*, which is equal to 0.052 m.

Section 5.1 will apply the diagnostic techniques introduced in section 4.4 to complete a qualitative assessment of the LDA measurements. In addition, the temperature measurements will also be investigated to assess the ideality of retrieving turbulence properties. The applicability of modeling of the intermittent behavior of the hot/cold jet interactions will also be reviewed. Section 5.2 will investigate the applicability of the power spectra and WAG algorithm for the detection and characterization of coherent structures.

5.1 Examination of the Experimental Data

5.1.1 Assessment of the LDA Data

Table 4.4-1 will be used as a qualitative guide in the assessment of the LDA data set. The Time Interval Distribution (TID) profiles for the detection measurement region are given in figures 5.1.1-1 to 5.1.1-6 with the remaining profiles given in appendix D. The characteristic time of distribution t_o can be obtained from the TID profiles allowing for the estimate of the mean data rate ($1/t_o$). These results are summarized in table

5.1.1-1. The turbulence intensities were also computed and defined as the ratio of the RMS value to the mean velocity of each component. The turbulence intensity profiles are given in figure 5.1.1-7.

The TID profiles for measurement positions from z/D = 6.5 to z/D = 2.69 appear to achieve a relatively ideal distribution as the linear fitted line appears to closely represent the distribution. This result is illustrated in figures 5.1.1-1 to 5.1.1-2. Slight effects due to velocity bias can be seen from the small peak at small time interval and minor effects due to 'round-off' errors can be seen from the 'comb-like' structure. These characteristics can be understood since the measurement locations corresponded to regions of low turbulence intensities as shown in figure 5.1.1-7. That is, these measurement locations are regions in which the two opposing jets are not highly interacting.

As the LDA measurements approached z/D = 1.92 to z/D = -1.92, obtaining adequate measurement data appear to be more difficult. Figures 5.1.1-3 to 5.1.1-6 illustrate that the existence of strong velocity bias as indicated by the sharp peak at short time intervals and the 'valley-like' profile. These results can be expected since this region corresponds to the position at which the two turbulent jet shear layers strongly interact. The effects of velocity bias have great implications on the estimate of the auto-correlation function, and hence the estimate of both the Taylor microscale and the integral time scale (Tummers et al., 2000, van Maanen et al., 1998, Benedict et al., 1998). The estimate the Taylor microscale is presented in figure 5.1.1-8 and illustrates

a large variability in the region of large turbulence intensities, and hence large velocity bias. Furthermore, the effects of velocity bias can result in a significant number of data points appearing greater than $5t_o$ (van Maanen, 2000). A theoretical estimate of the number of points expected to appear after $5t_o$ can be computed from equation (4.4-1), which is approximately 0.67% for an ideal distribution. Systems with significant velocity bias will result in a significant number of data points appearing after $5t_o$ as shown in figures 5.1.1-1 to 5.1.1-6 and summarized in table 5.1.1-1. This result has great implications in the estimate of the passing length scale in the WAG algorithm as discussed in section 4.2. In addition, problems of round-off errors also appear to be present in the interacting region of the opposing jets. This problem is seen in the crenellate profile due to an insufficient accuracy in the storage of the cumulative arrival time. Further support for round-off errors due to quantisation by the processor is seen in figure 5.1.1-9 that shows a 'comb-like' probability distribution function for the axial velocity at z/D = 4.23.

Instantaneous velocity profiles were used to investigate the presence of multiple validation errors (van Maanen, 2000). The signature property of multiple validation is seen from sharp peaks as shown in figure 5.1.1-10 for the instantaneous axial velocity measurement at z/D = -1.15.

Summary

The result of the LDA data assessment is that the measurement data appear to be sufficient in regions of low turbulence intensities (z/D = 6.5 to z/D = 2.7). As the

measurements approached the interaction region of two jet shear layers (z/D = 1.92 to z/D = -1.92), problems associated with low data rates, noise and velocity bias will not allow the proper retrieval of small-scale turbulence properties.

Table 5.1.1-1: A summary of the results from the TID profiles

z/D	To [ms] (approximate)	Mean Data Rate ($1/t_o$) [Hz]	Mean Nyquist Frequency [Hz]	Number of Data points above $5t_o$
5.77	15.7	63.69	31.85	0.5%
5	13.5	74.07	37.04	0.65%
4.23	15.6	64.10	32.05	0.85%
3.46	16.8	59.52	29.76	1.2%
2.69	26.6	37.59	18.80	1.7%
1.92	44.5	22.47	11.24	1.9%
1.15	59.4	16.84	8.42	2.3%
0.385	39.8	25.13	12.56	1.9%
-0.385	49.2	20.33	10.16	2.1%
-1.15	***140.0***	7.14	3.57	***3%***
-1.9	32.6	30.67	15.34	2.3%
-2.69	22.4	44.64	22.32	1%

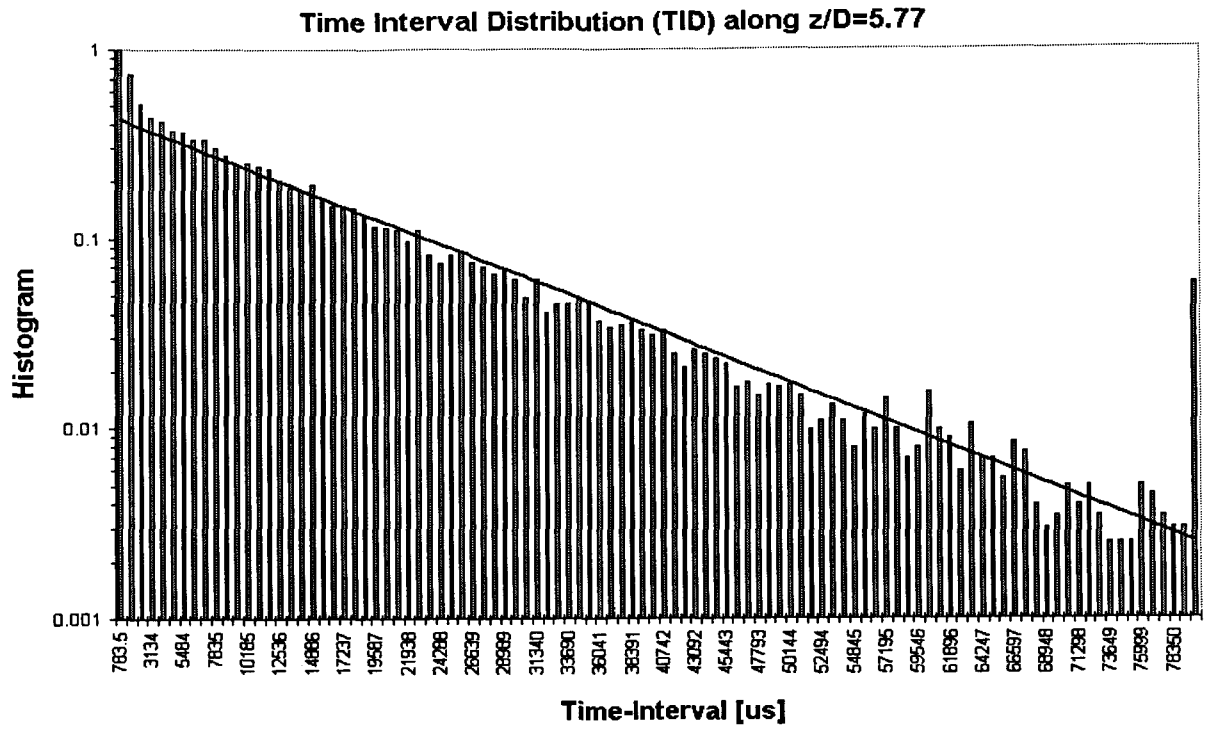

Figure 5.1.1-1 Time Interval Distribution (TID) at z/D = 5.77

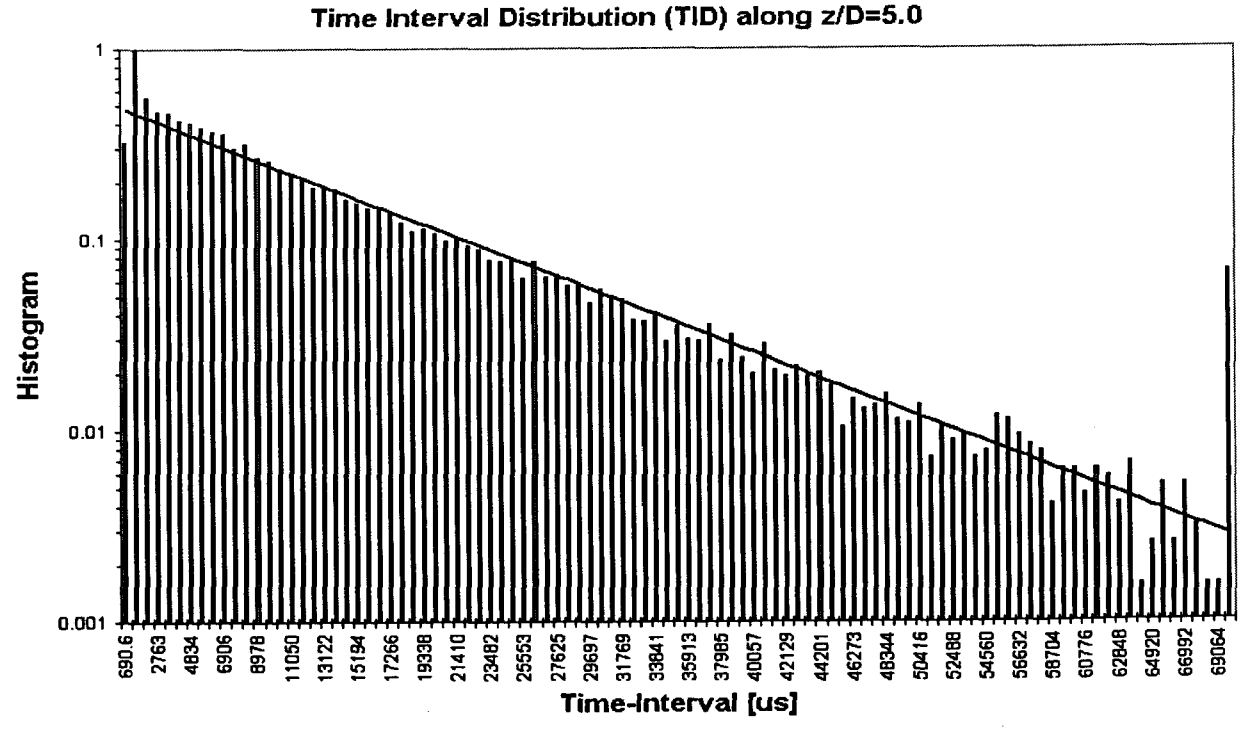

Figure 5.1.1-2 Time Interval Distribution (TID) at z/D = 5.0

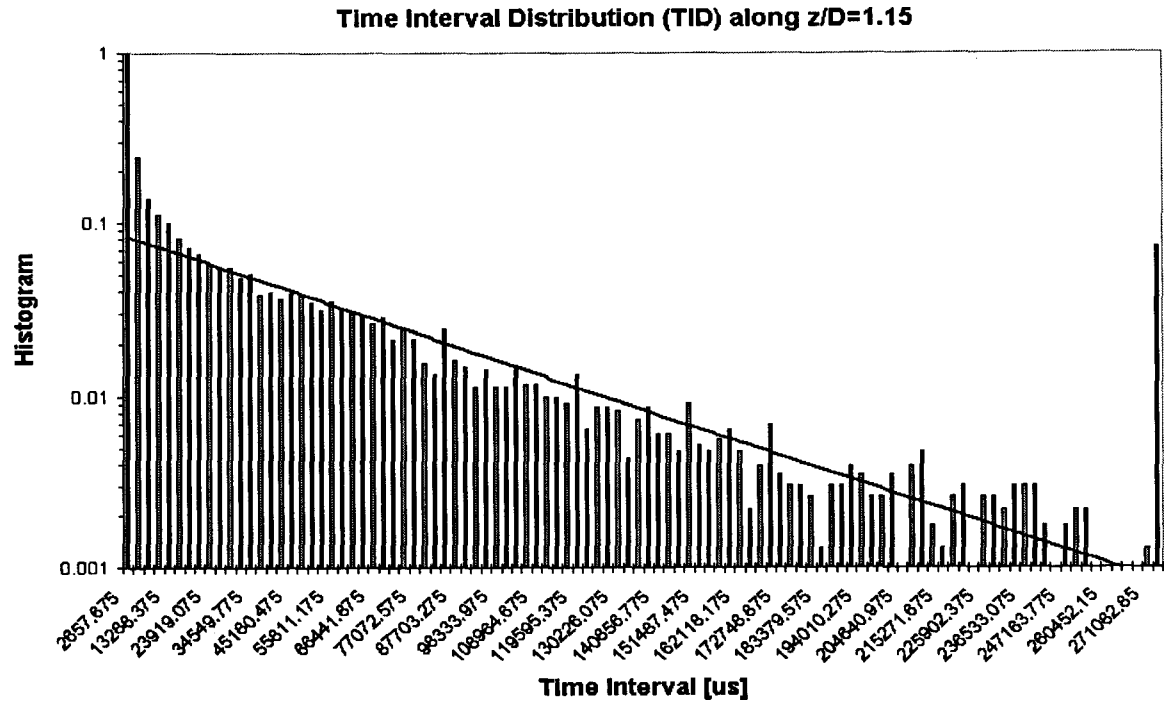

Figure 5.1.1-3 Time Interval Distribution (TID) at z/D = 1.15

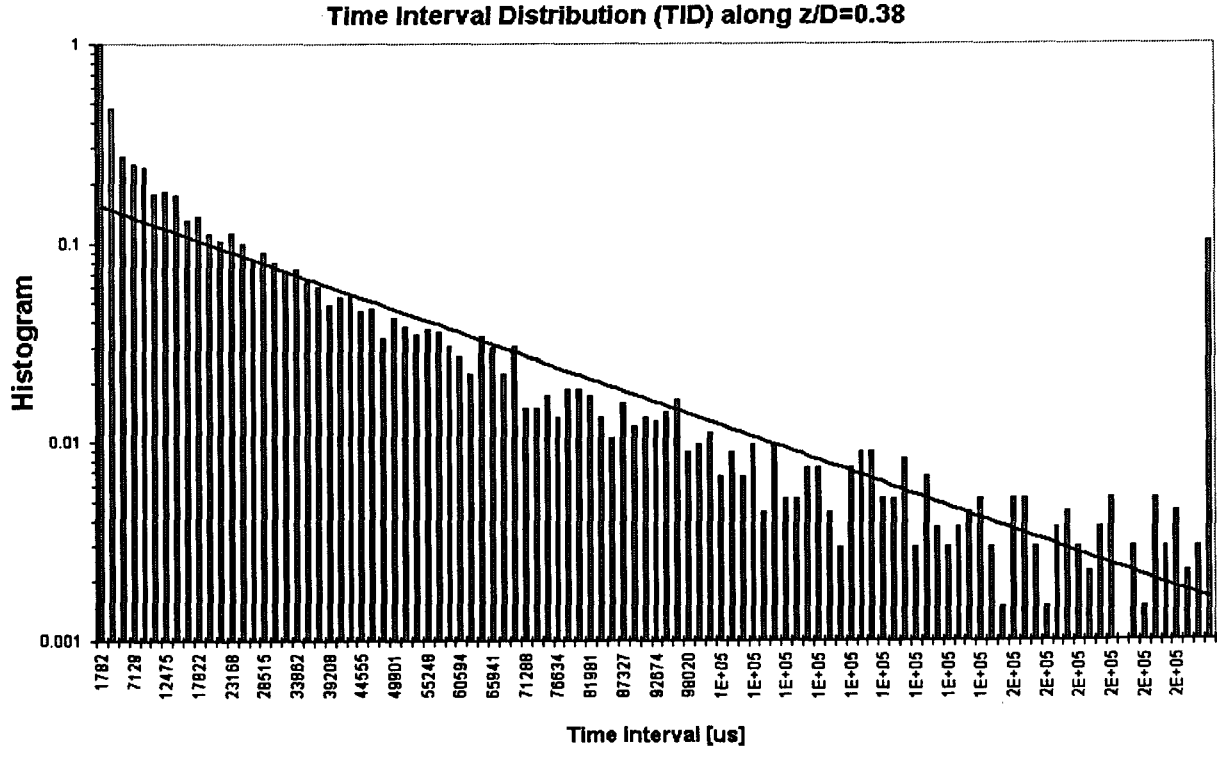

Figure 5.1.1-4 Time Interval Distribution (TID) at z/D = 0.38

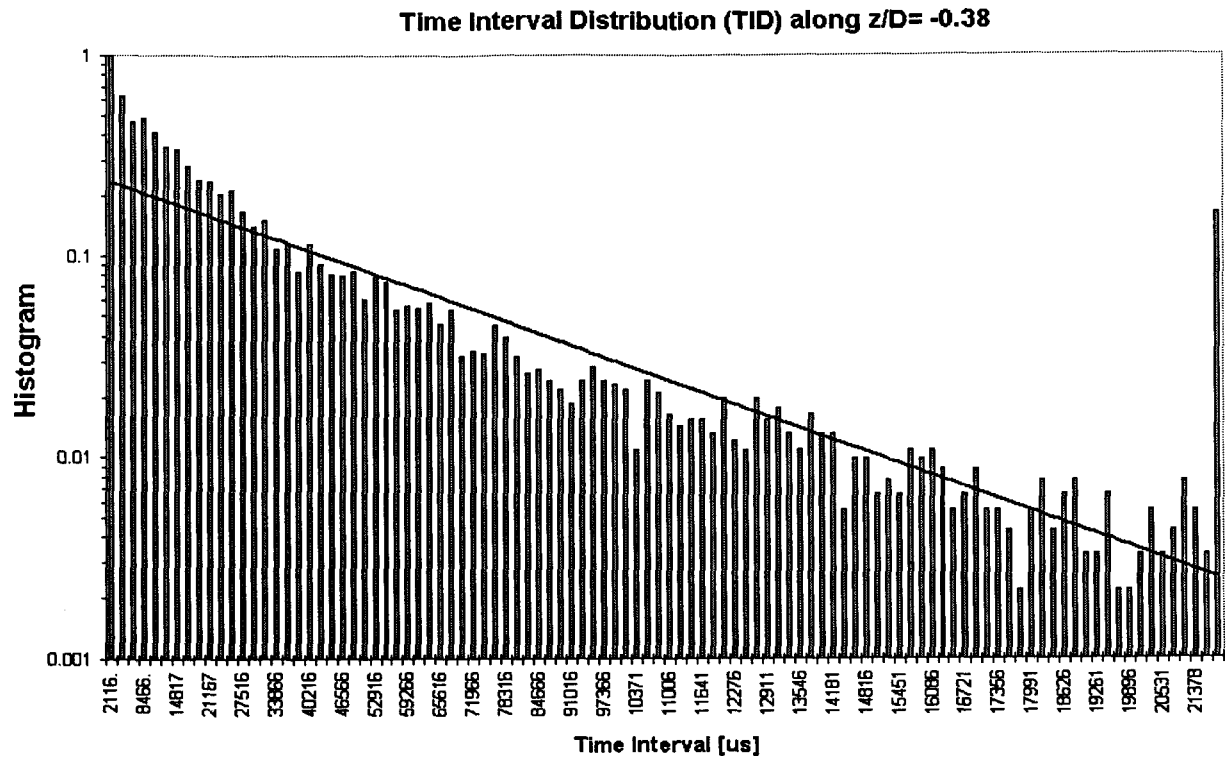

Figure 5.1.1-5 Time Interval Distribution (TID) at z/D = -0.38

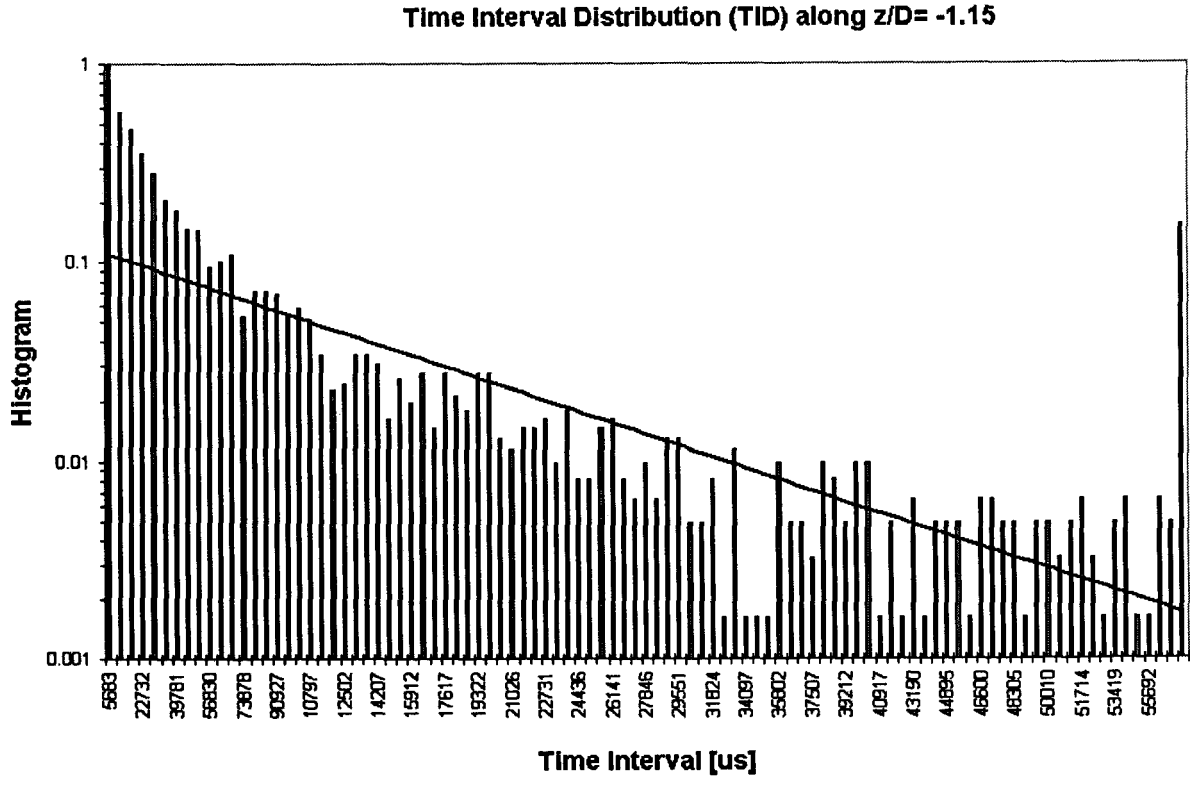

Figure 5.1.1-6 Time Interval Distribution (TID) at z/D = -1.15

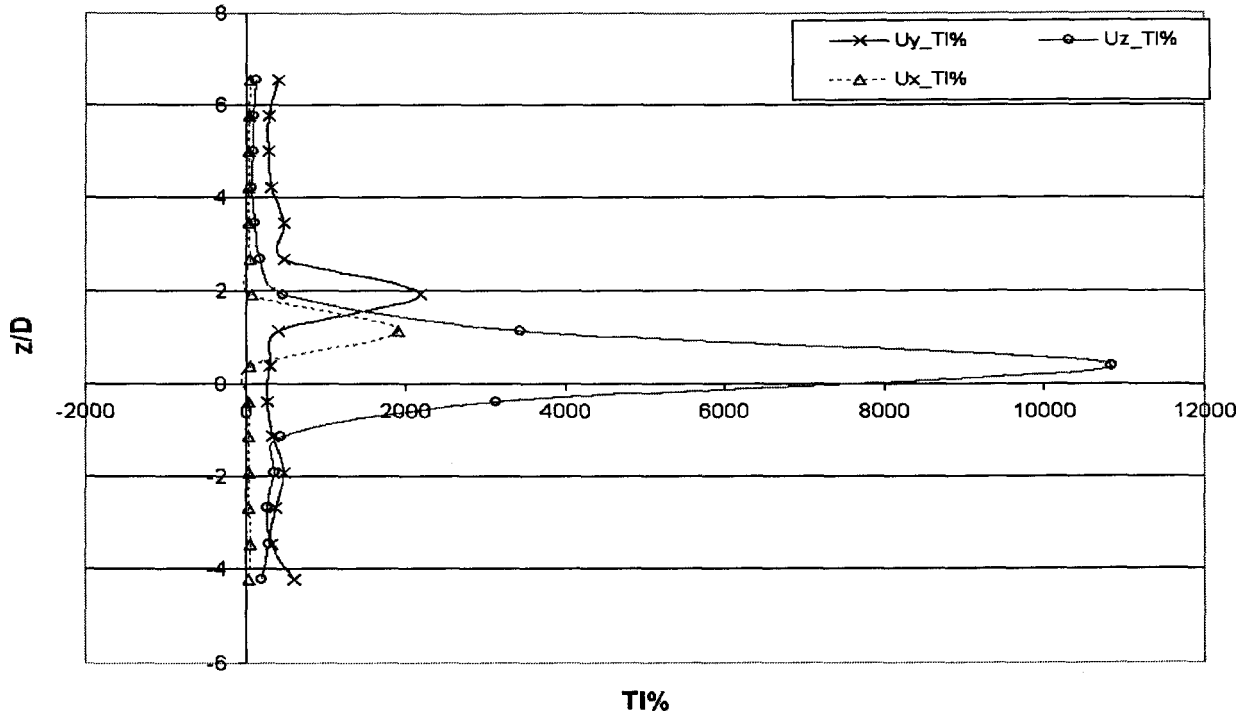

Figure 5.1.1-7 The Turbulence Intensities (TI) at x/D = 11.425, y/D = 0.

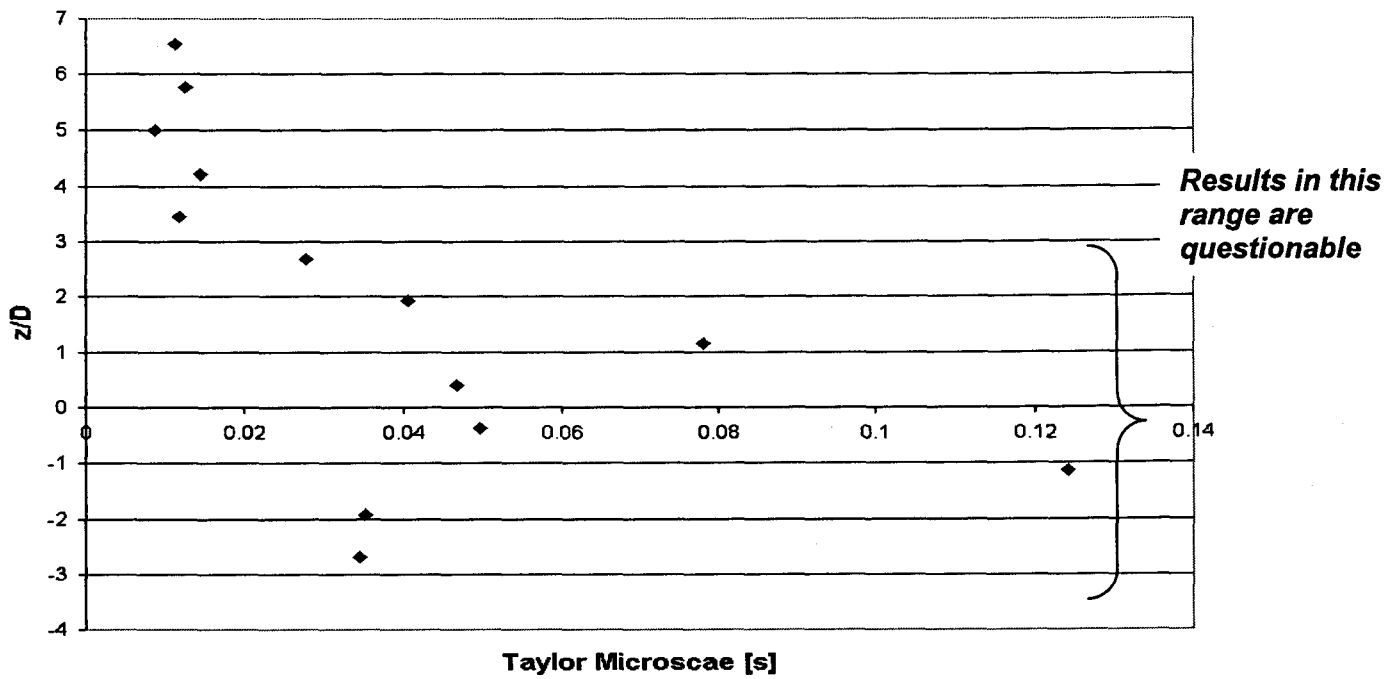

Figure 5.1.1-8 Estimate of the Taylor Microscale using a 2nd order parabolic fit on the ACF. Measurement values taken at x/D = 11.425, y/D = 0.

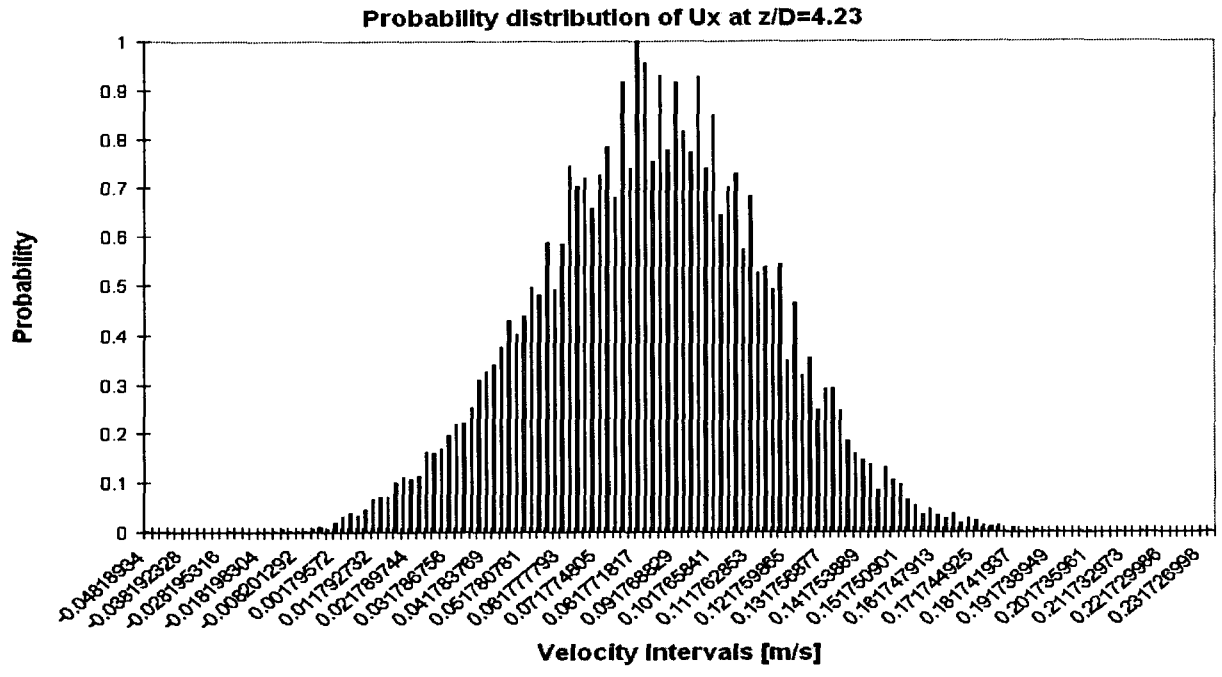

Figure 5.1.1-9 Probability distribution function of the axial velocity at z/D = 4.23. The 'comb-like' profile points to problems associated with round-off errors due to the quantisation by the processor.

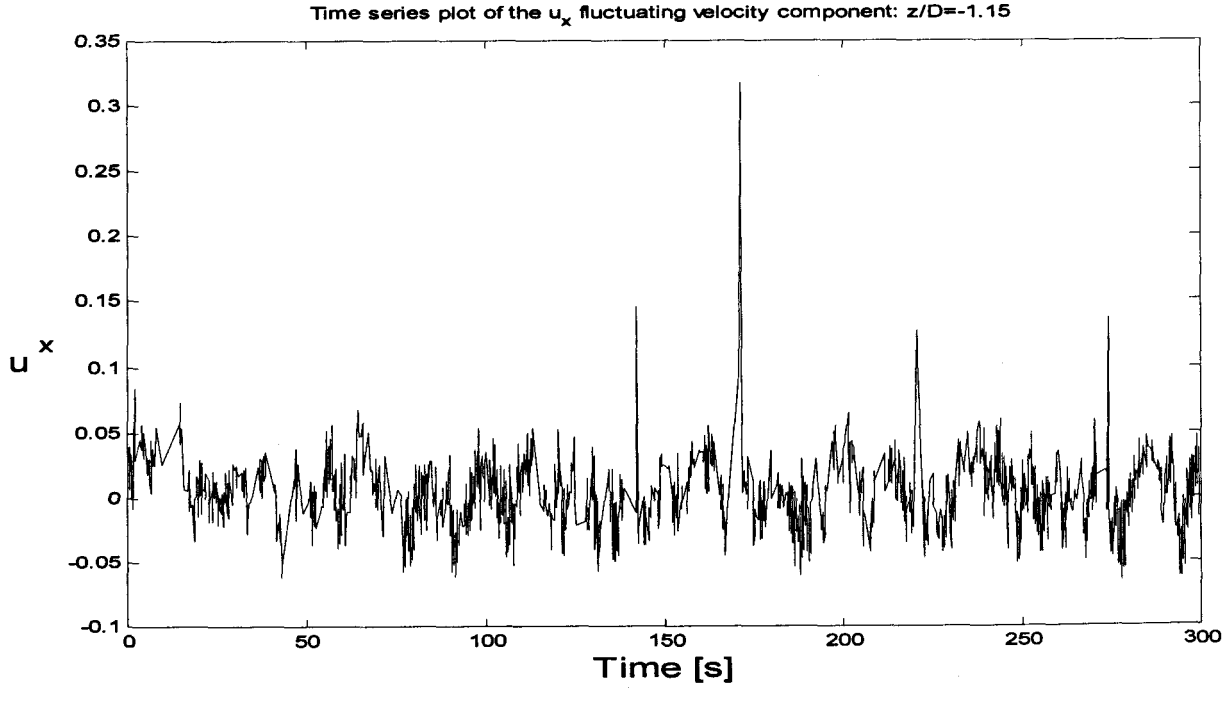

Figure 5.1.1-10 Instantaneous velocity measurements at z/D = -1.15. Indications that multiple validation issues are producing erroneous behaviour in the velocity estimates.

5.1.2 Assessment of the Temperature Measurements

The temperature measurement positions from the fixed thermocouple grid are seen in figures 3.1-6 and 3.1-7. The spatial positions of the thermocouples were nearly two jet diameters apart in the vertical and lateral directions. As noted by Atsavapranee (1997), the effect of stratification on the flow is that any development of coherent structures will be significantly suppressed. This result implies that the size of a typical large-scale structure will be much smaller in flows with significant stratification, and thus the current experimental design may not be sufficient to extract turbulence temporal and spatial time scales from the temperature measurements. In addition, the actual measurement position was not optimal in capturing the hot/cold jet shear layer interaction. This result can be seen in figure 5.1.3-1. It appears that greater insight into the intermittent behavior of the hot/cold jet shear layers could be achieved if additional measurements were placed laterally along $z/D \cong 1.0$, which approximately corresponds to the region of large stratification.

For the moving thermocouple (figure 3.1-8), the position of each thermocouple is approximately 77% of the jet diameter above the velocity measurement volume. Again, this separation is not ideal. Values less than half a jet diameter may be more appropriate for a more reliable application of a conditionally sampled statistical model using both the temperature and velocity measurements. In addition, significant differences in the sampling frequencies exist between the thermocouple (0.2 Hz) and the LDA (varied between 74 Hz to 7 Hz). Future investigation may consider increasing

the sampling frequency in the thermocouple closer to that of the LDA measurements so that more information about the flow phenomenon can be captured in the temperature/velocity statistical model.

Furthermore, to avoid aliasing[10] effects, the sampling frequency must be twice the highest frequency component in the system. Using the jet diameter and jet exit velocity, this characteristic frequency corresponds to approximately 5 Hz. In addition, the local characteristic frequency at x/D = 11.42 was roughly 1 Hz. Thus, the thermocouple measurements could not be used in the analysis since a sampling frequency of only 0.2 Hz was used.

Summary

The conclusion in this section is that the present design in the stationary temperature measurements is not adequate for the retrieval of small-scale turbulence properties such as the spatial and temporal scales. Vertical and lateral separations of less than half a jet diameter may be more appropriate. The large separation in the moving thermocouple is not optimal for the application of a conditionally sampled statistical model to explain the intermittent behavior of the flow. Again, separations of less than half a jet diameter would be more appropriate. Furthermore, since the sampling frequency for all thermocouples was less than the characteristic frequency of the

---

[10] Aliasing effects results when the sampling frequency is lower than the characteristic frequency of the system. It results in the introduction of artificial frequency components (Otnes et al., 1978).

system, temperature measurements could not be used to extract turbulence properties from the flow.

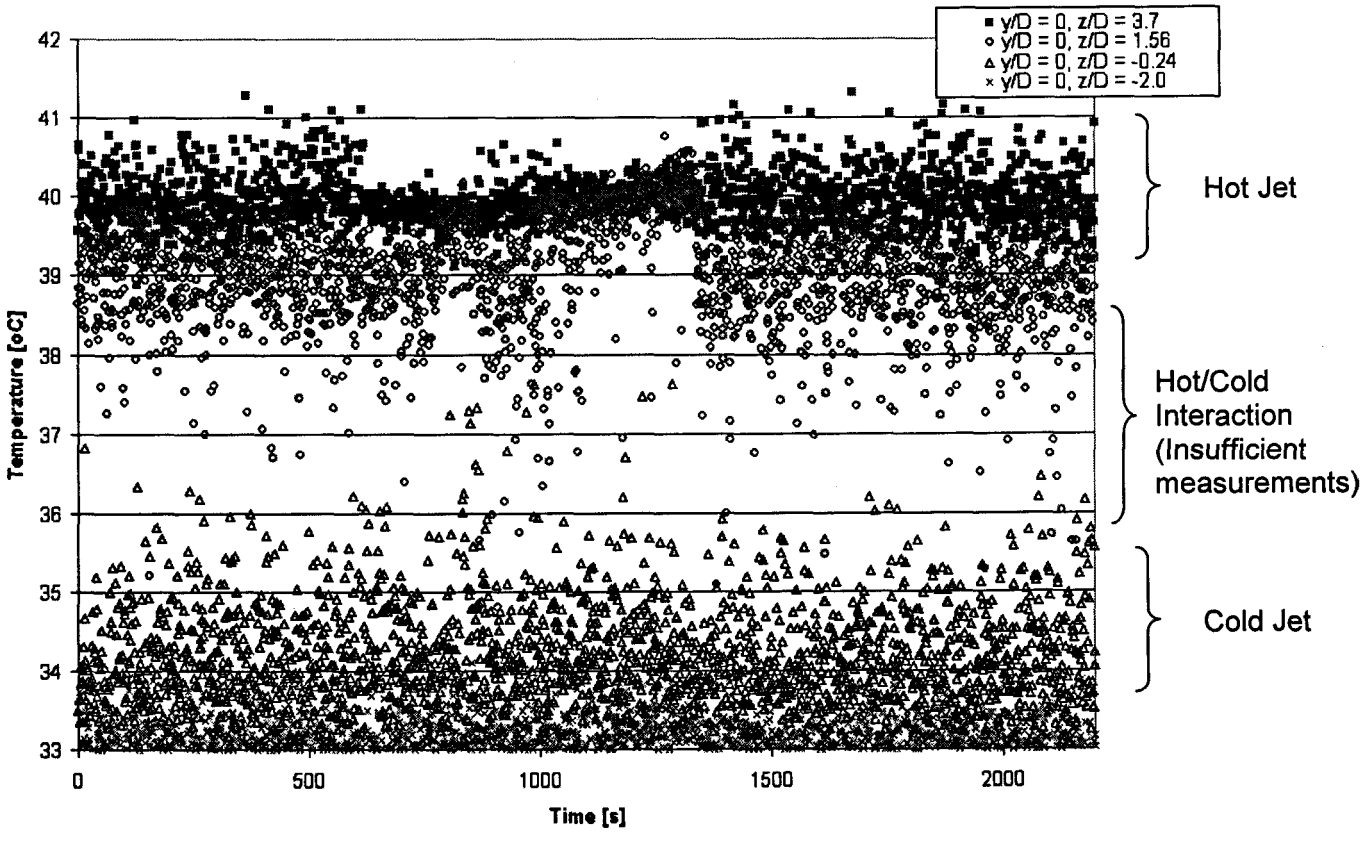

Figure 5.1.2-1 Thermocouple measurements at x/D =12.7, y/D = 0. The spatial positions are nearly 2 jet diameters apart in the vertical z/D axis and 2 jet diameters apart in the lateral axis (see figure 5.1.3-3).

5.1.3 Global Characteristics

The global characteristics of the two-opposing turbulent jets are investigated in the following section, and the details are summarized in table 5.1.3-1.

Plots of the velocity and temperature contours of the jet are given in figures 5.1.3-1 and 5.1.3-2, and provide a global aspect of the flow. Available measurements are indicated on the corresponding figures and were used in a cubic interpolation scheme to fit a surface through the available data.

The results of figures 5.1.3-1 and 5.1.3-2 illustrate the effects of buoyancy and momentum on the hot turbulent jet, which results in a curved trajectory. The results suggest that the jet shear layers lie along the vertical axis at x/D = 11.42.

Other global properties of the experimental system are investigated using the fixed thermocouple measurements. A cross-sectional view (YZ-plane) along the region of the suspected interaction zone of two shear layers can be obtained and given in figure 5.1.3-3. The results indicate regions of strong temperature stratification in the system, spanning nearly two jet diameters in the vertical direction from z/D = 1.7 to z/D = -0.28. The stratification effect can be understood by the interaction of the two shear layers; however, the design of the experiment also influenced the stratification properties of the vessel. That is, the top region of the jet was designed with four flow exits resulting in a bias to maintain the temperature of the cold jet by draining only the hotter fluids.

vessel. That is, the top region of the jet was designed with four flow exits resulting in a bias to maintain the temperature of the cold jet by draining only the hotter fluids.

The effects of the stratification on the jet flows can be further investigated from the temperature distribution profiles and the statistical outputs. The histogram profiles of the temperature measurements along YZ-plane at x/D = 12.7 illustrate that different profiles exist depending on the measurement location. Measurements at z/D = 3.9 and z/D = -3.9 illustrate a more uniform temperature distribution profile as seen in figures 5.1.3-4 and 5.1.3-5. In addition, the standard deviation and skewness coefficients are also relatively smaller as compared to the other measurement positions. These graphs are shown in figures 5.1.3-6 and 5.1.3-7. This finding can be understood since the measurement positions essentially correspond to the location of the hot jet (z/D = 3.9) and cold jet (z/D = -3.9) with very little interaction. The fact that the skewness is not perfectly zero to indicate a perfectly uniform distribution may be a result of fluid entrainment of one jet into the other.

As the temperature measurements approached the interaction region of the two shear layers (z/D = 1.56 to z/D = -2.05.), the standard deviation increased significantly. The strong variability about the mean value suggests a possible existence of a bimodal distribution as a result of the hot and cold jet interaction. However, histogram profiles as shown in figures 5.1.3-8 to 5.1.3-10 for z/D = 1.56, z/D = -0.28 and z/D = -2.05 respectively, do not clearly support this hypothesis. This result may be due to 1) the coarse sampling frequency, and 2) measurement positions taken outside of the

interaction zone of two shear layers. Significant skew was also observed in the histogram profiles in the region of greatest stratification as shown in figures 5.1.3-6 and 5.1.3-7. For measurements near the hot jet, a negative skew was observed, whereas a positive skew was noted for measurements in the cold jet region. This result is again consistent with the entrainment hypothesis noted earlier, in which one jet entrains the fluid of the other at infrequent times. It is suspected that a higher sampling frequency may reveal a larger distribution in the tails of the histogram. The kurtosis (or flatness factor) is also given in figure 5.1.3-11 and suggests that the temperature distribution of the two opposing jets have a kurtosis factor that is symmetrical about the y/D axis. Additional temperature distributions for the other measurement locations can be found in appendix E.

A top-view (XY-plane) is taken at two different vertical positions to investigate the uniformity of the temperature distribution as caused by the temperature stratification. As shown in figure 5.1.3-3, temperature stratification begins at approximately z/D = 0 to z/D = 1.55. Thus, XY-plane profiles are given in figures 5.1.3-12 (a) for z/D = 0.0127 and 5.1.3-12(b) for z/D = 1.56. These results suggest that the temperature along the XY-plane is essentially uniform with approximately one degree Celsius difference along each plane. Figure 5.1.3-12(b) suggests a slight asymmetry in the temperature distribution along the XY-plane. A possible account for this deviation may be due to the slight bias in the jet exit velocity as shown in figure 5.1.3-13 where a larger mean velocity exists relative to the centre in the negative y/R position. However, this issue is

still unclear since it has been known that transfer of energy in systems with buoyant forces has shown to favour axial and lateral transfers of energy (Piccirillo et al., 1997).

To further investigate the possible position of the shear layers, the LDA velocity measurements were used to compute the correlation coefficients and joint histograms of the fluctuating velocity components normalized by its root-mean squared values. These profiles are computed along the vertical measurements at x/D = 11.42 and y/D = 0. The cross-correlation coefficients are given in figure 5.1.3-14, and the joint histograms are given in figures 5.1.3-15 to 5.1.3-17 for z/D = 1.92, z/D =1.15, and z/D = 0.38 respectively. Regions of isotropic flows would result in contours of the joint histograms that appear as circles since no preferred direction can exist when the Reynolds stresses are uniformly zero (Tennekes et al., 1972). However, regions with strong shear production would result in an elliptical profile, which suggests a presence of coherent structures. As shown in figure 5.1.3-14 and the profile of the turbulence intensities given in figure 5.1.1-7, the region of large shear production appears to be between z/D = 1.92 and z/D = -1.92, which corresponds to the region in which the opposing jets interact. The joint histogram at z/D = 1.15 (figure 5.1.3-16) also supports the hypothesis of significant shear production as the profiles displayed an elliptical distribution in the $u_x u_z$ and $u_y u_z$ components.

still unclear since it has been known that transfer of energy in systems with buoyant forces has shown to favour axial and lateral transfers of energy (Piccirillo et al., 1997).

To further investigate the possible position of the shear layers, the LDA velocity measurements were used to compute the correlation coefficients and joint histograms of the fluctuating velocity components normalized by its root-mean squared values. These profiles are computed along the vertical measurements at x/D = 11.42 and y/D = 0. The cross-correlation coefficients are given in figure 5.1.3-14, and the joint histograms are given in figures 5.1.3-15 to 5.1.3-17 for z/D = 1.92, z/D =1.15, and z/D = 0.38 respectively. Regions of isotropic flows would result in contours of the joint histograms that appear as circles since no preferred direction can exist when the Reynolds stresses are uniformly zero (Tennekes et al., 1972). However, regions with strong shear production would result in an elliptical profile, which suggests a presence of coherent structures. As shown in figure 5.1.3-14 and the profile of the turbulence intensities given in figure 5.1.1-7, the region of large shear production appears to be between z/D = 1.92 and z/D = -1.92, which corresponds to the region in which the opposing jets interact. The joint histogram at z/D = 1.15 (figure 5.1.3-16) also supports the hypothesis of significant shear production as the profiles displayed an elliptical distribution in the $u_x u_z$ and $u_y u_z$ components.

Table 5.1.3-1: Summary of the Characteristics of the Experimental System[11] (using the Mean Centre Line Velocity). Please set section *Notations* for the units.	
Fluid	Water in both jets
Reynolds Number, Re (Hot jet)	22300
Mean jet centreline velocity U_x	0.262559
Q_o	0.0005576
M_o	0.0001464
B_o	0.000557601
ρ	988.7
$\rho^{12}{}_o$	992.25
ρ_a	992.25

[11] Please see table 3.1-2 for additional information of the experimental system

[12]Average of the density of the hot and cold jet, ie., the density at T=40°C

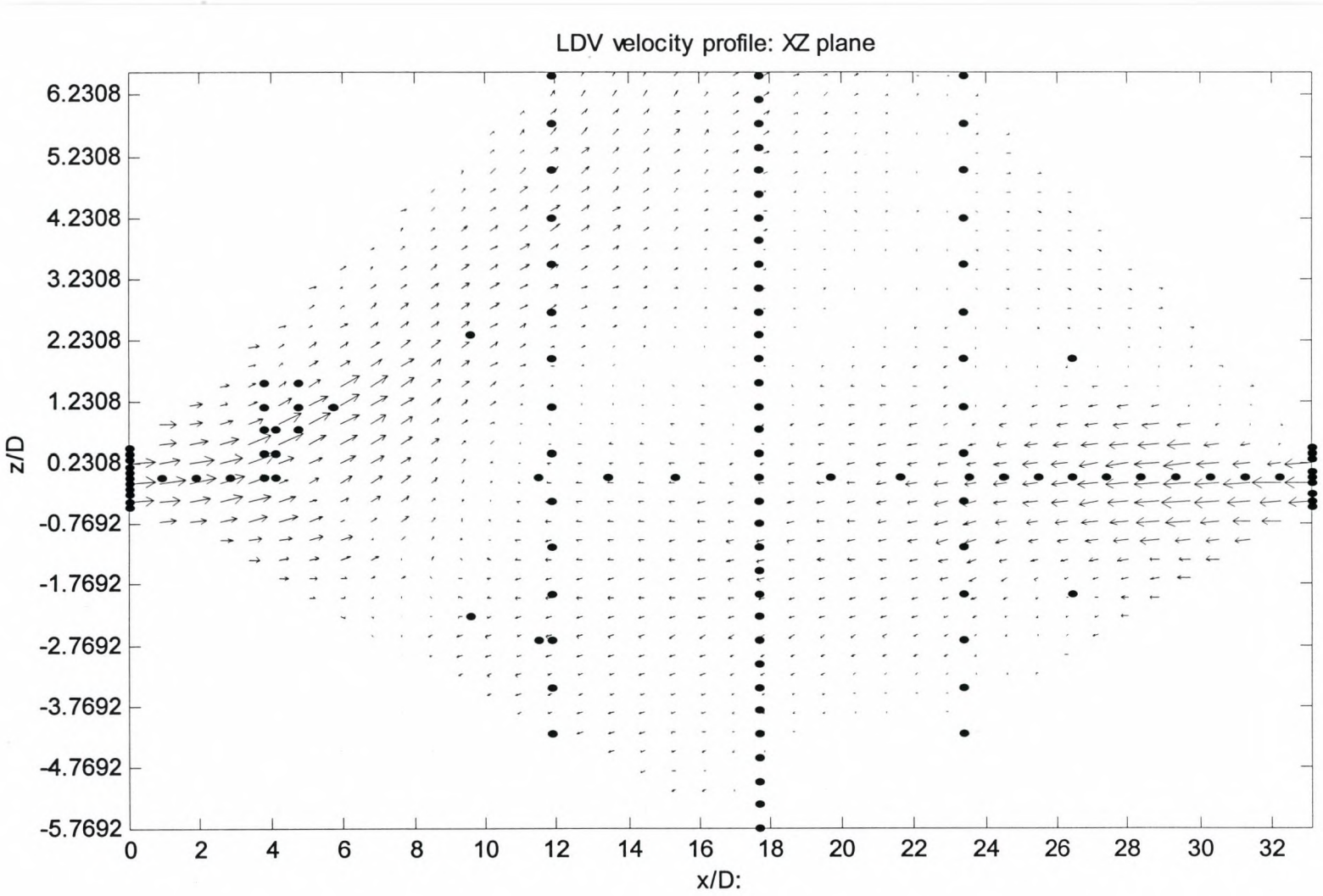

Figure 5.1.3-1 Mean velocity profile using LDV data along the XZ-plane. The position of the hot jet is at x/D = 0. The solid dots correspond to the measurement positions. The buoyant length scale is estimated to be at 5.79 jet diameters

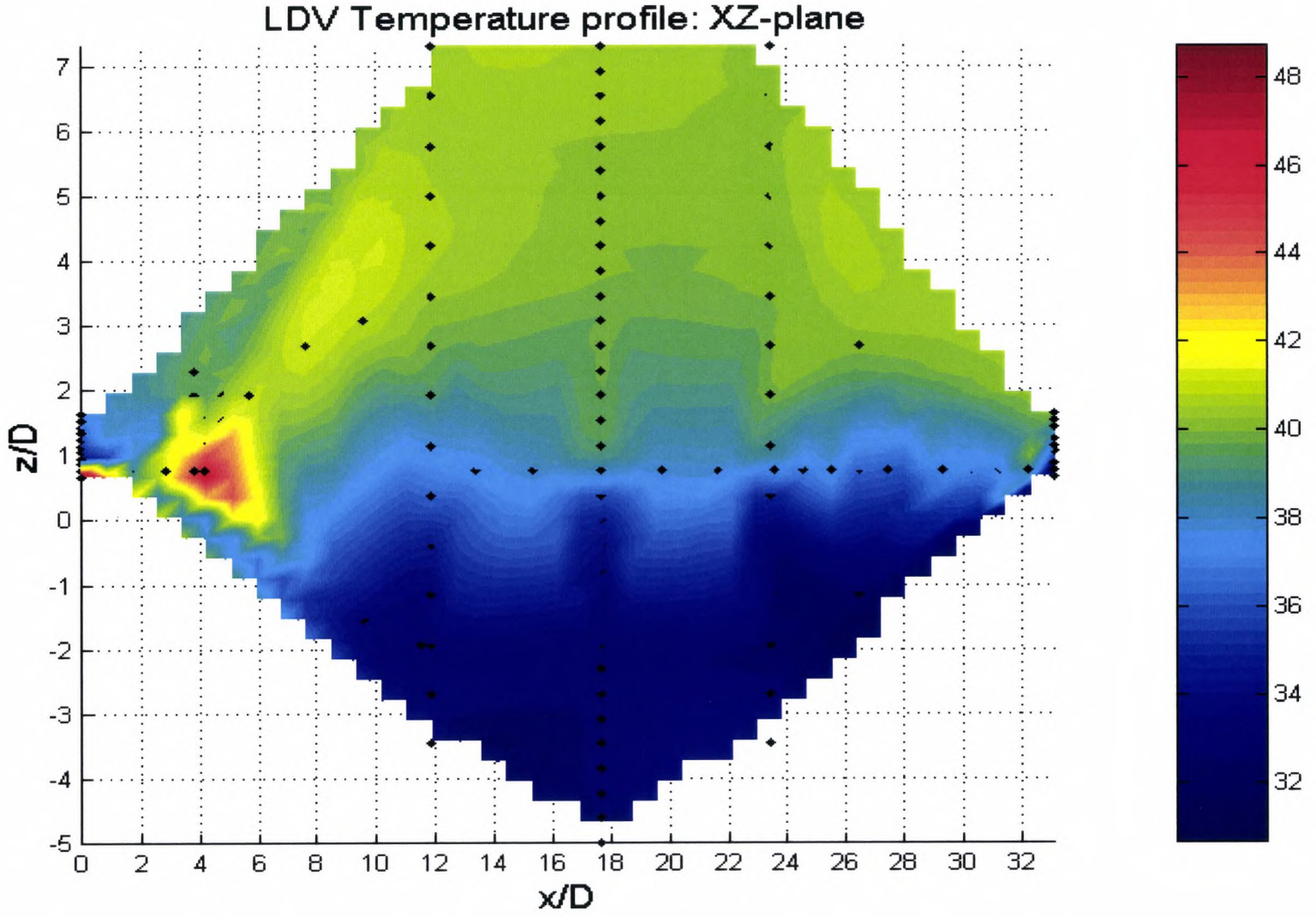

Figure 5.1.3-2 Mean temperature (°C) profile using the moving thermocouple along the XZ-plane. The position of the hot jet is at x/D = 0. The solid dots represent the measurement position. The buoyant length scale is estimated to be at 5.79 jet diameters

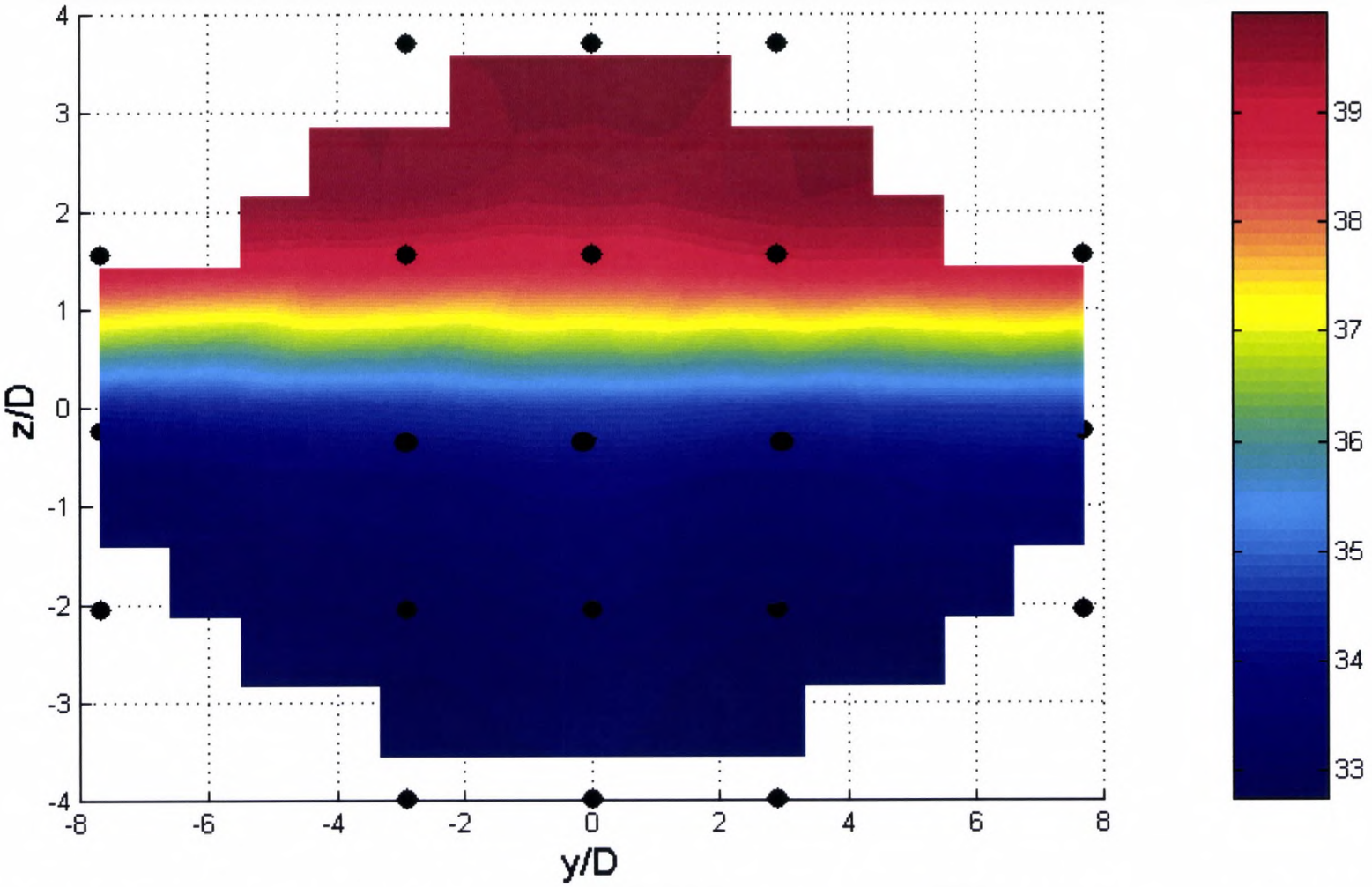

Figure 5.1.3-3 Mean temperature (°C) profile using fixed thermocouple measurements at the YZ-plane at x/D = 12.7. Solid dots correspond to the measurement locations and were used to interpolated the surrounding temperature values.

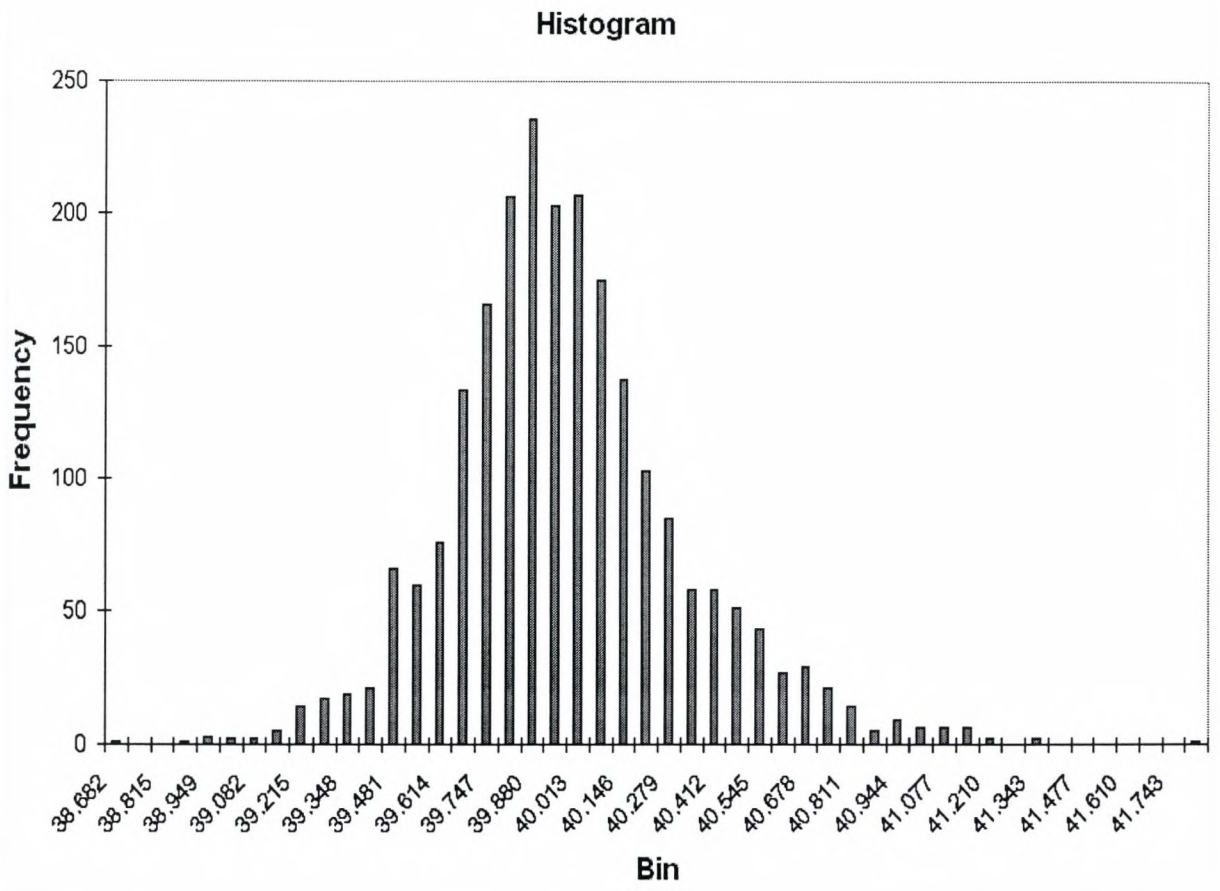

Figure 5.1.3-4 Temperature distribution at x/D = 12.7, z/D = 3.7,y/D = 0

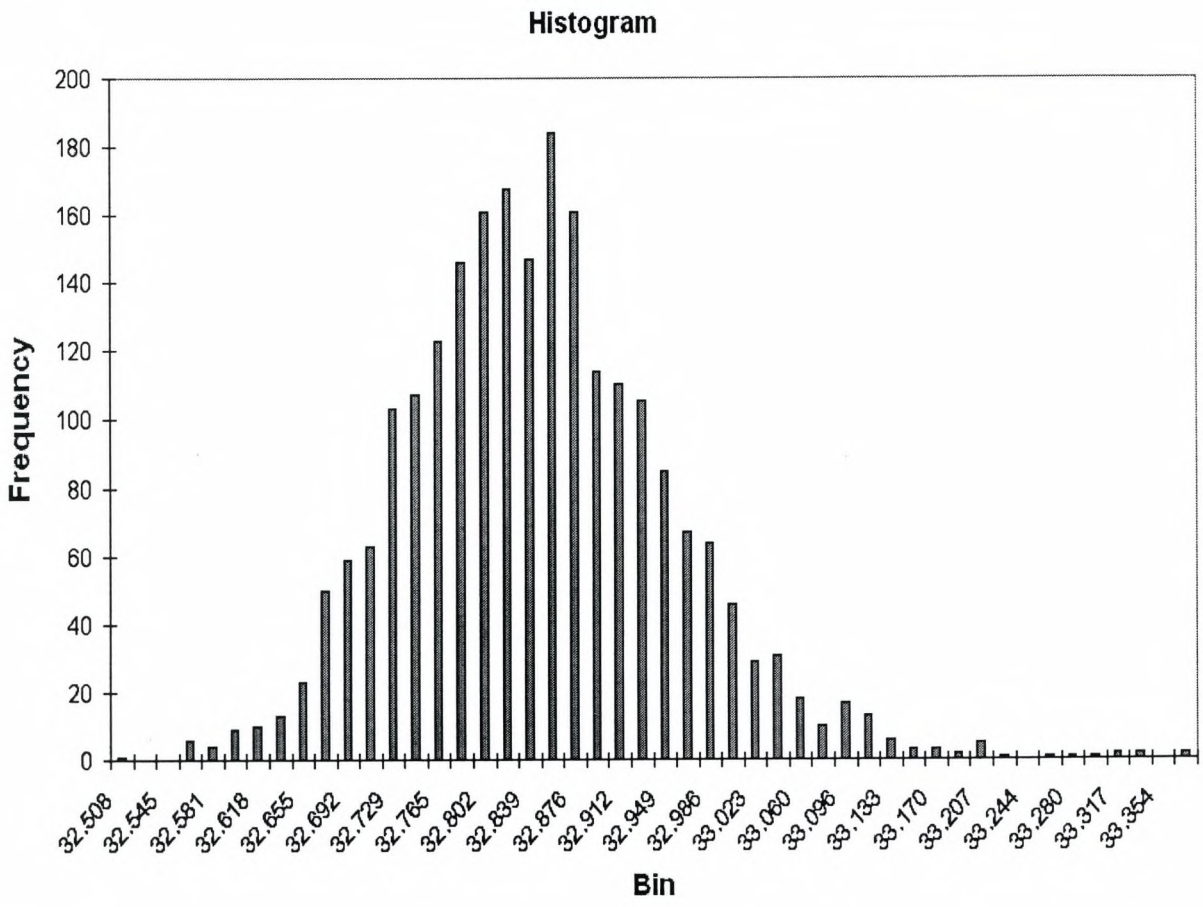

Figure 5.1.3-5 Temperature distribution at x/D = 12.7, z/D = -3.99, y/D = 0

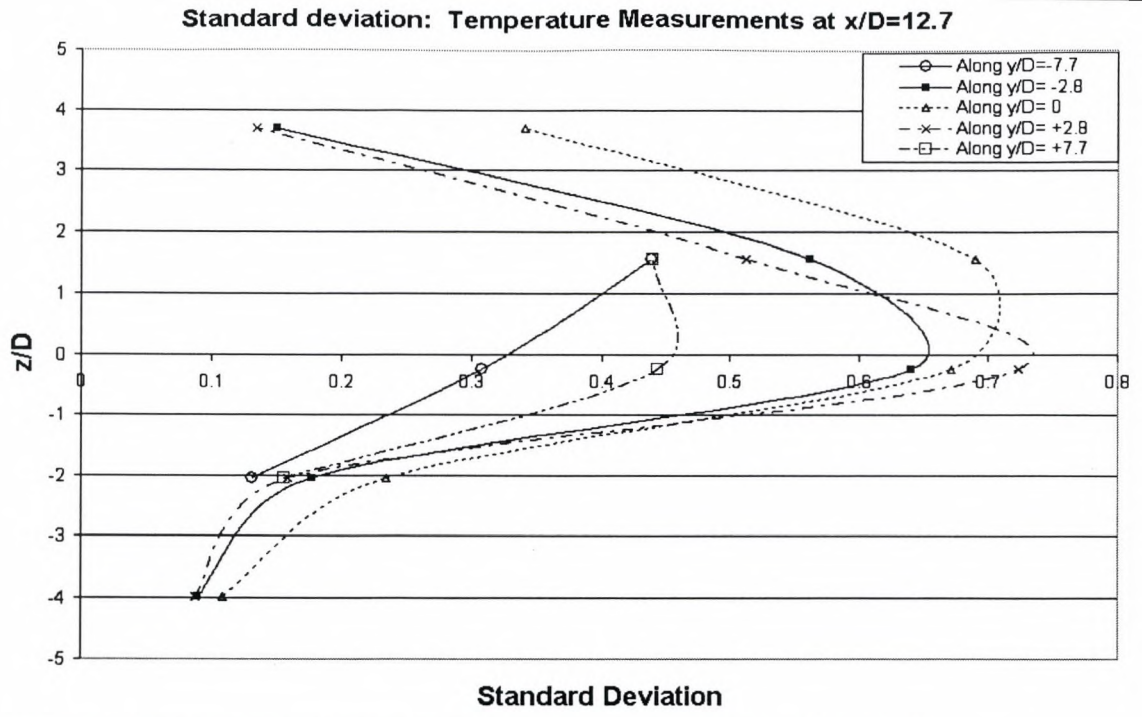

Figure 5.1.3-6 Standard deviation along the YZ-plane at x/D = 12.7

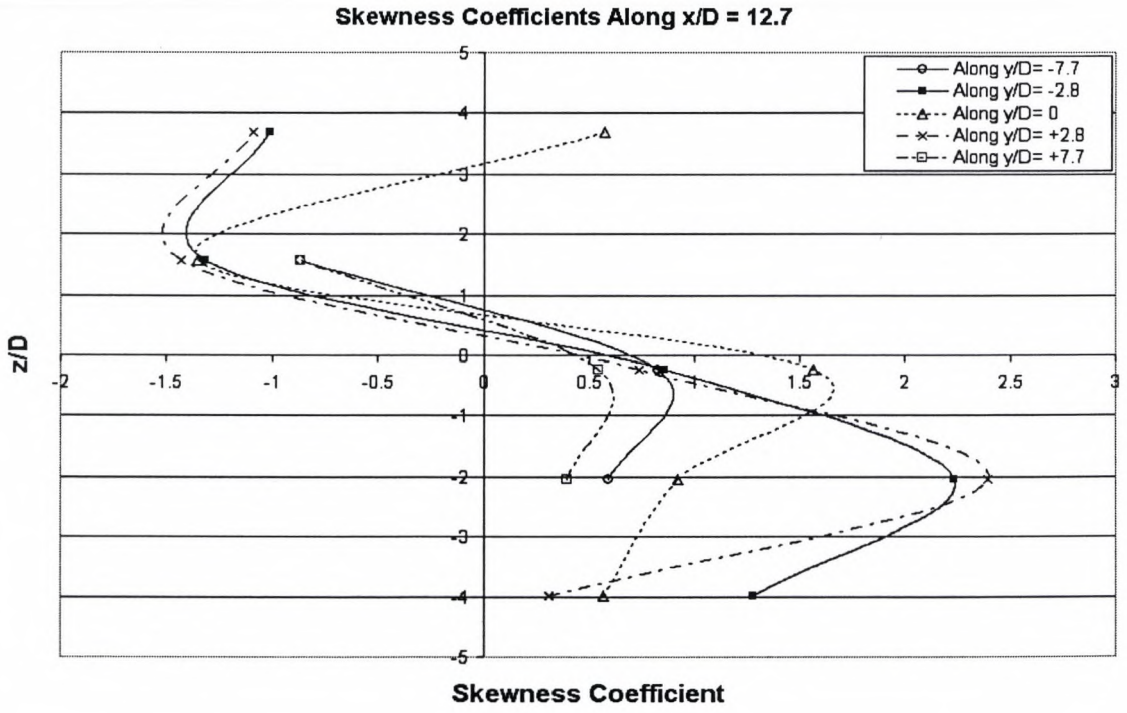

Figure 5.1.3-7 Skewness coefficients along the YZ-plane at x/D = 12.7

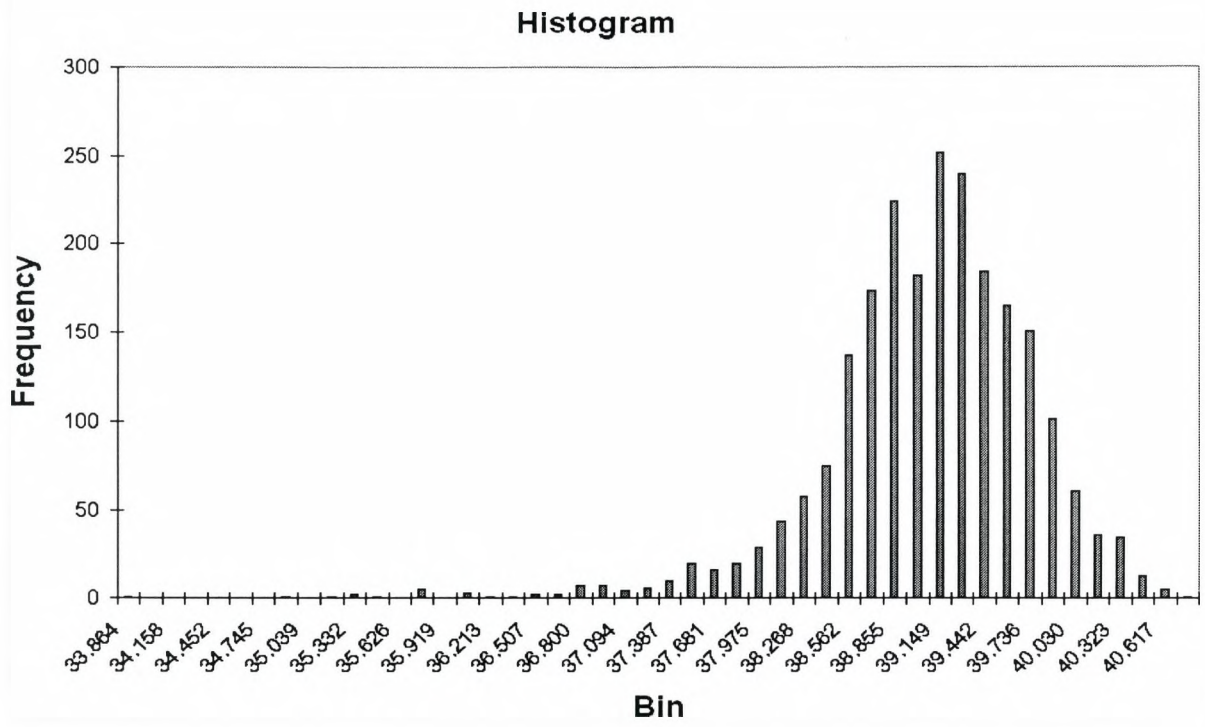

Figure 5.1.3-8 Temperature distribution at x/D = 12.7, z/D = 1.5, y/D = 0

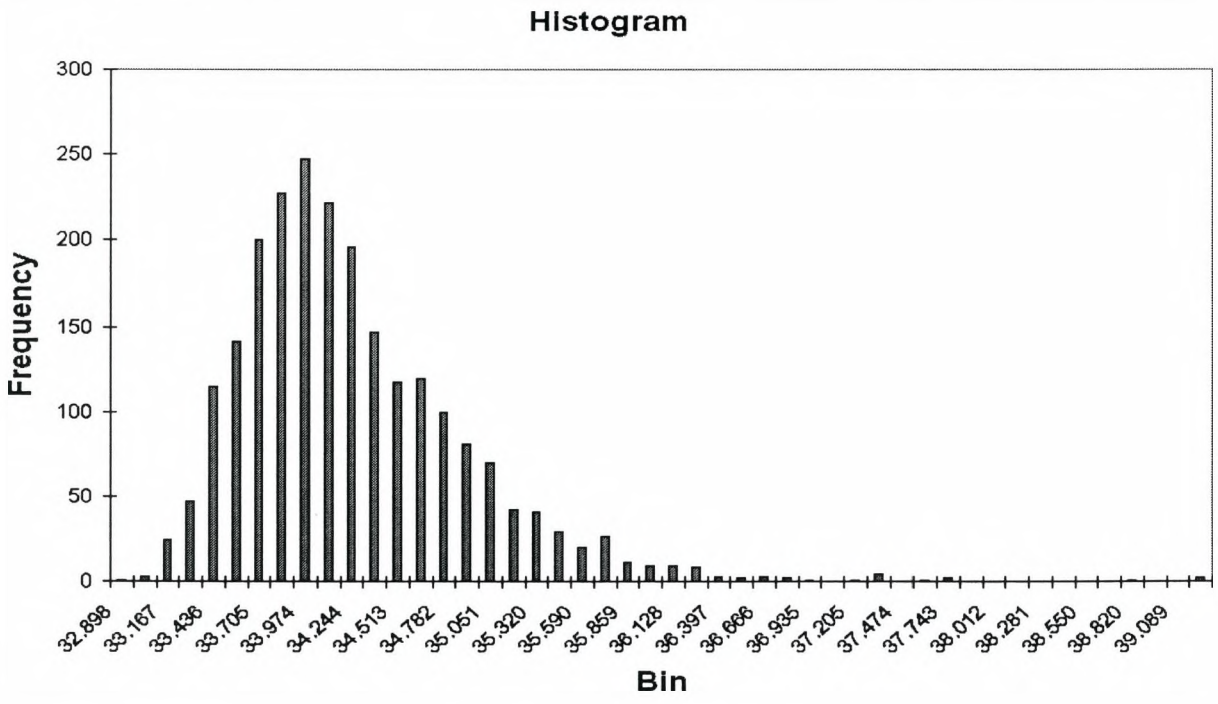

Figure 5.1.3-9 Temperature distribution at x/D = 12.7, z/D = -0.24, y/D = 0

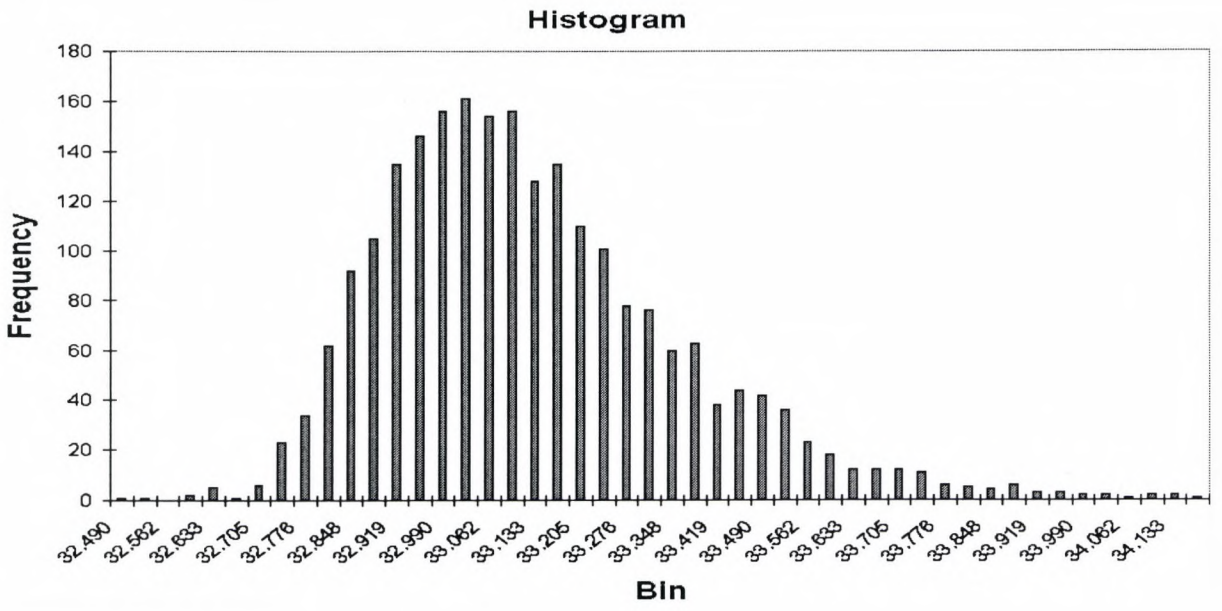

Figure 5.1.3-10 Temperature distribution at x/D = 12.7, z/D = -2.05, y/D = 0

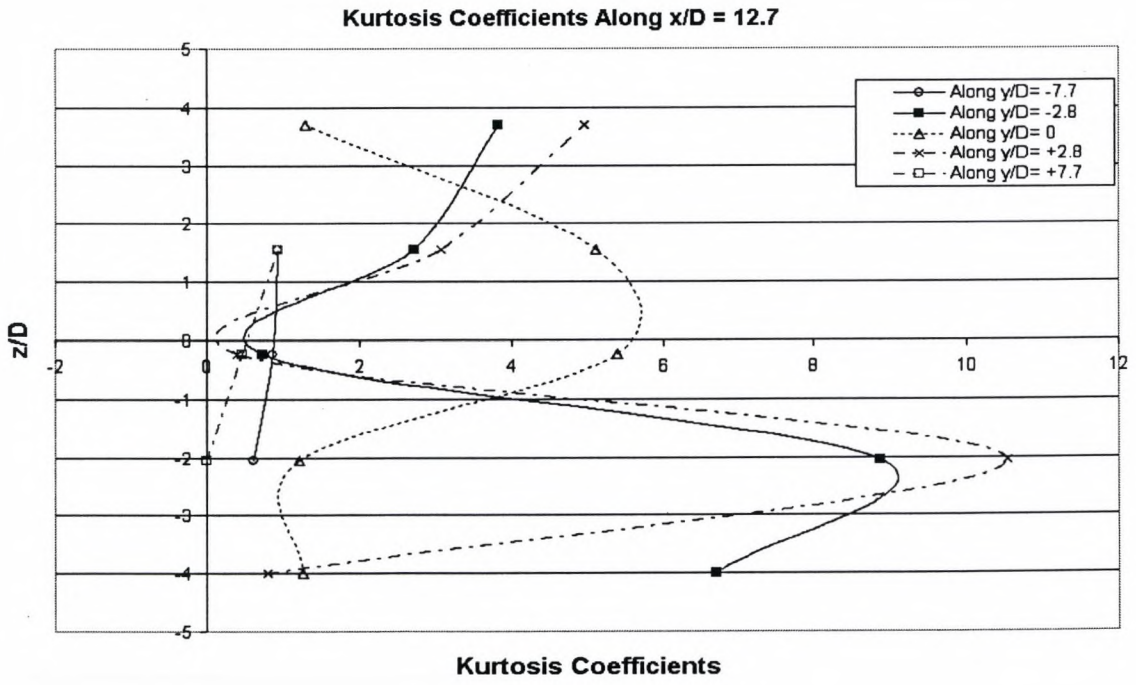

Figure 5.1.3-11 Kurtosis coefficients along the YZ-plane at x/D = 12.7

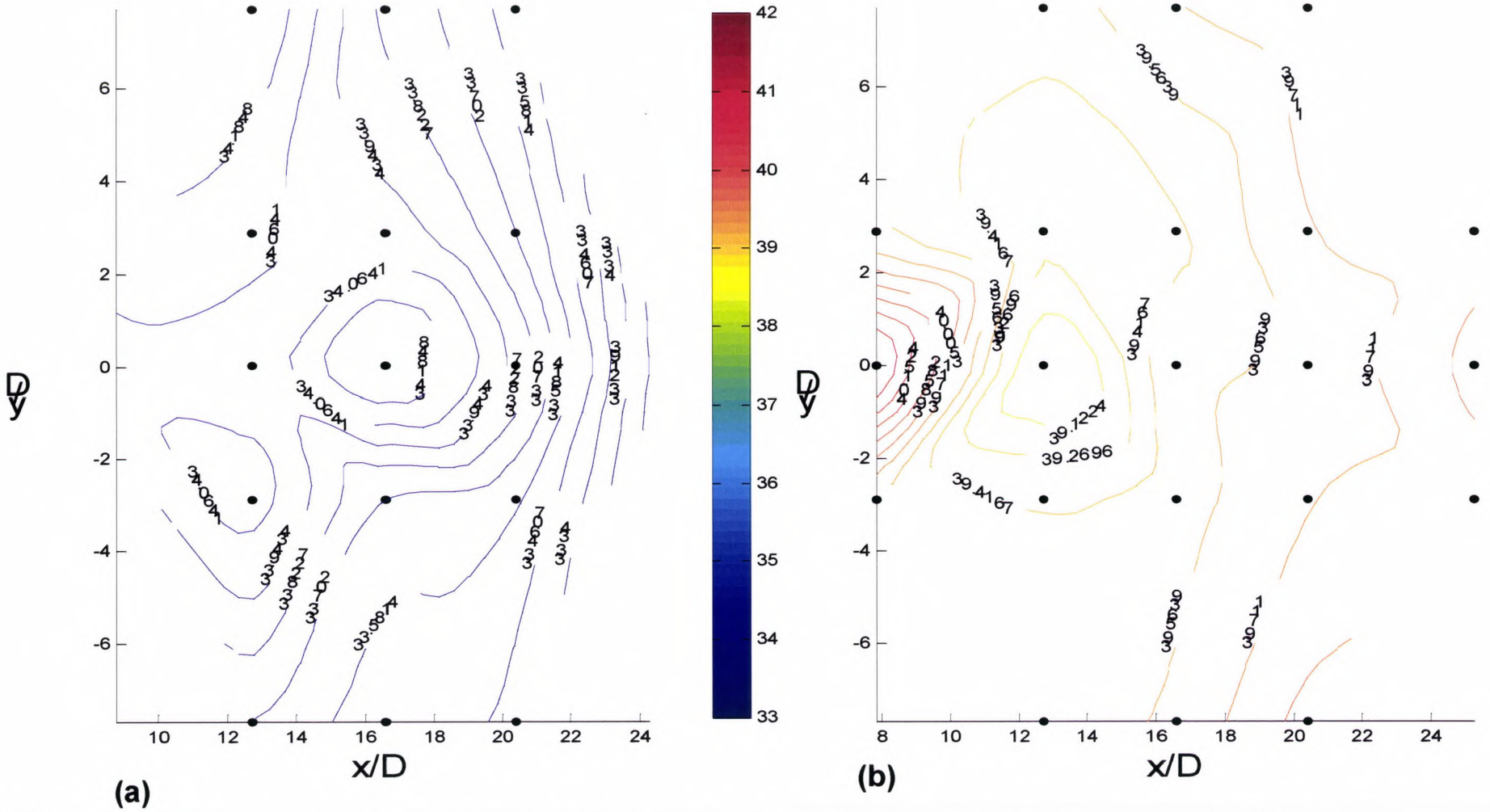

Figure 5.1.3-12 (a) Top-view of the mean temperature (°C) profile using fixed thermocouple measurements along the XY-plane at z/D = -0.0127. Solid dots correspond to the measurement locations (b) Top-view of the mean temperature (°C) profile using fixed thermocouple measurements along the XY-plane at z/D = 1.56. Solid dots correspond to the measurement locations.

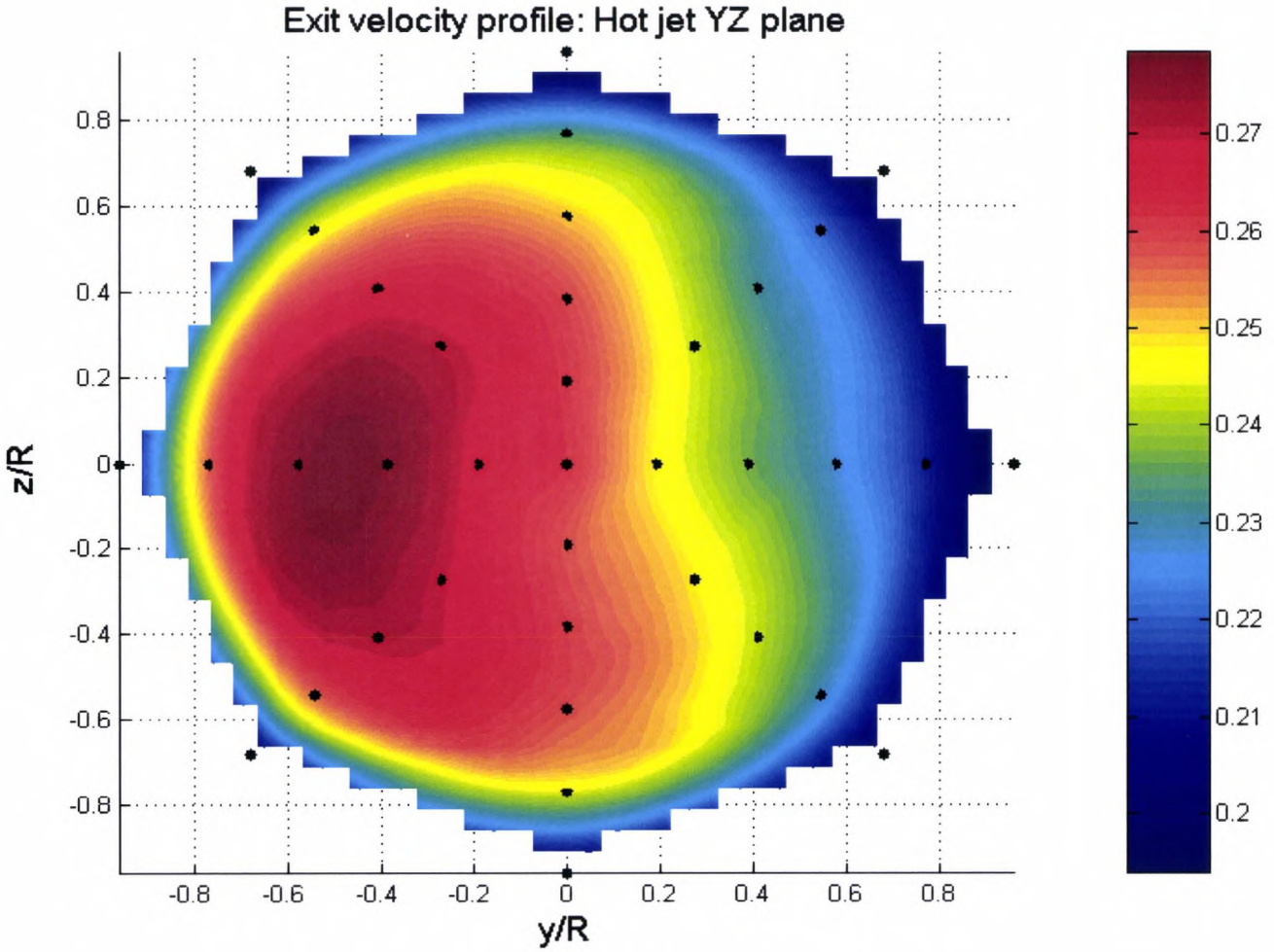

Figure 5.1.3-13 Mean exit velocity (m/s) profile in the hot turbulent jet using LDV measurements. Solid dots correspond to the measurement locations

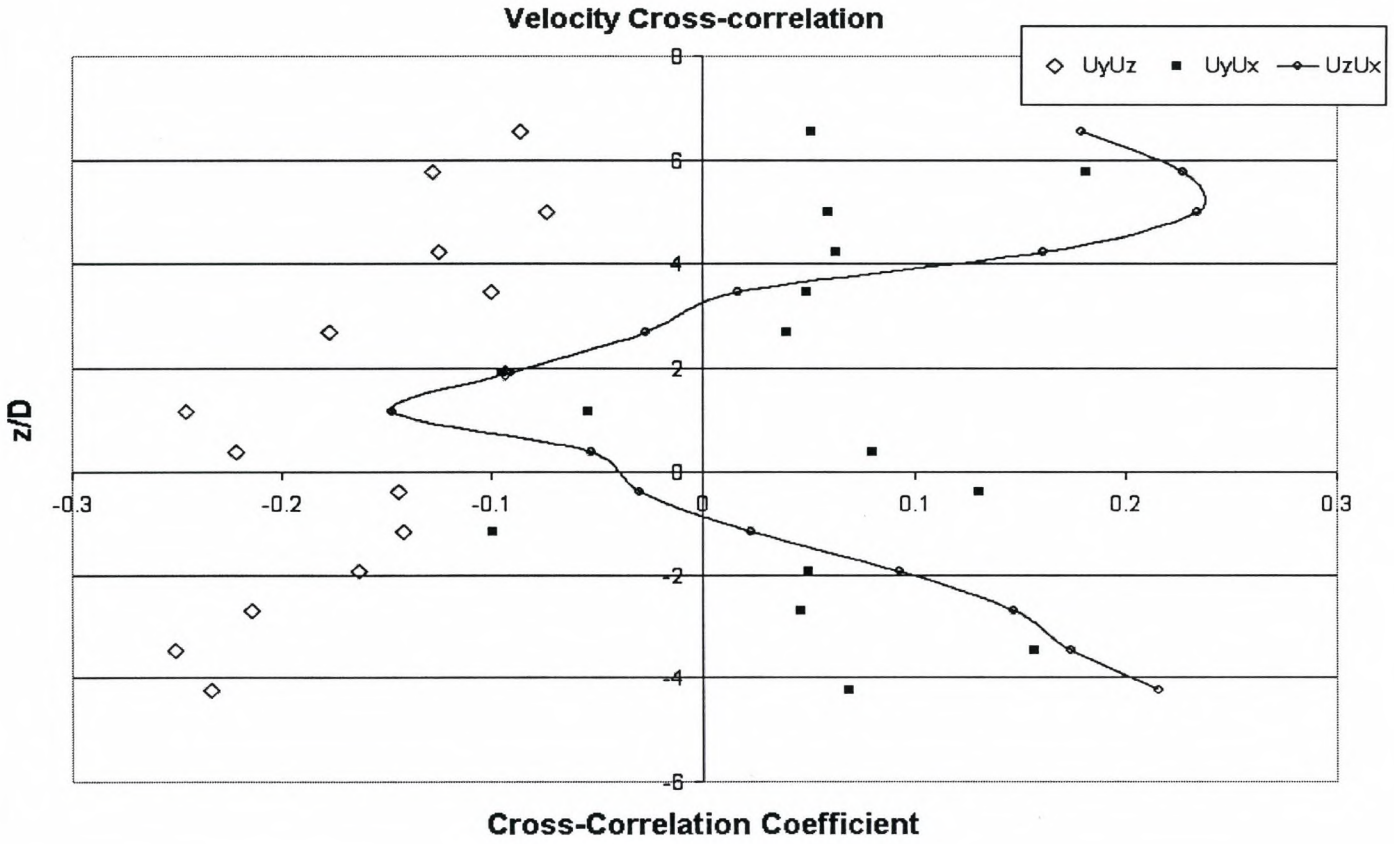

Figure 5.1.3-14 Cross-correlation coefficients along the YD-plane at x/D = 11.42.

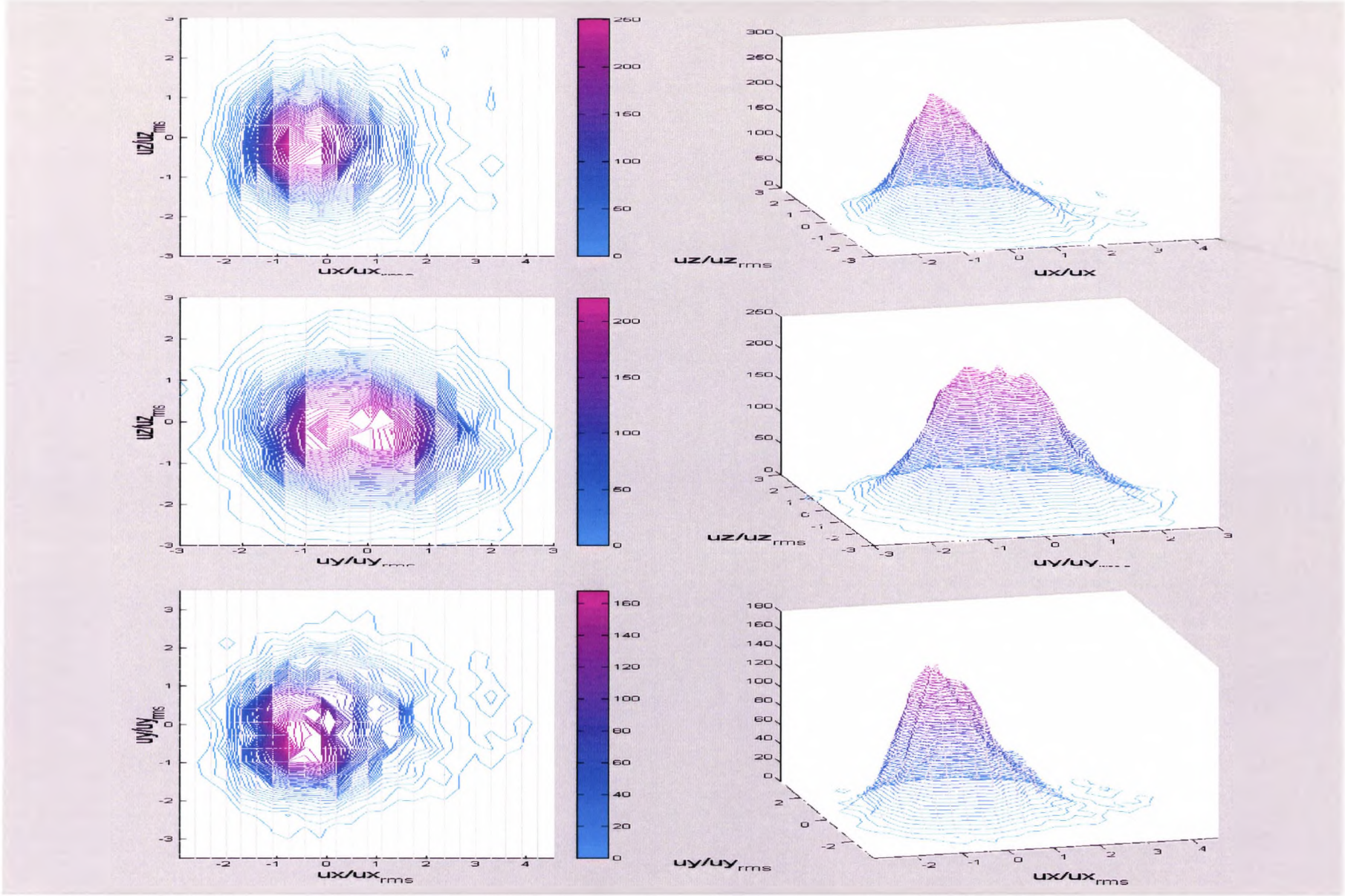

Figure 5.1.3-15 Joint probability distribution functions at z/D = 1.92, x/D = 11.425, y/D = 0

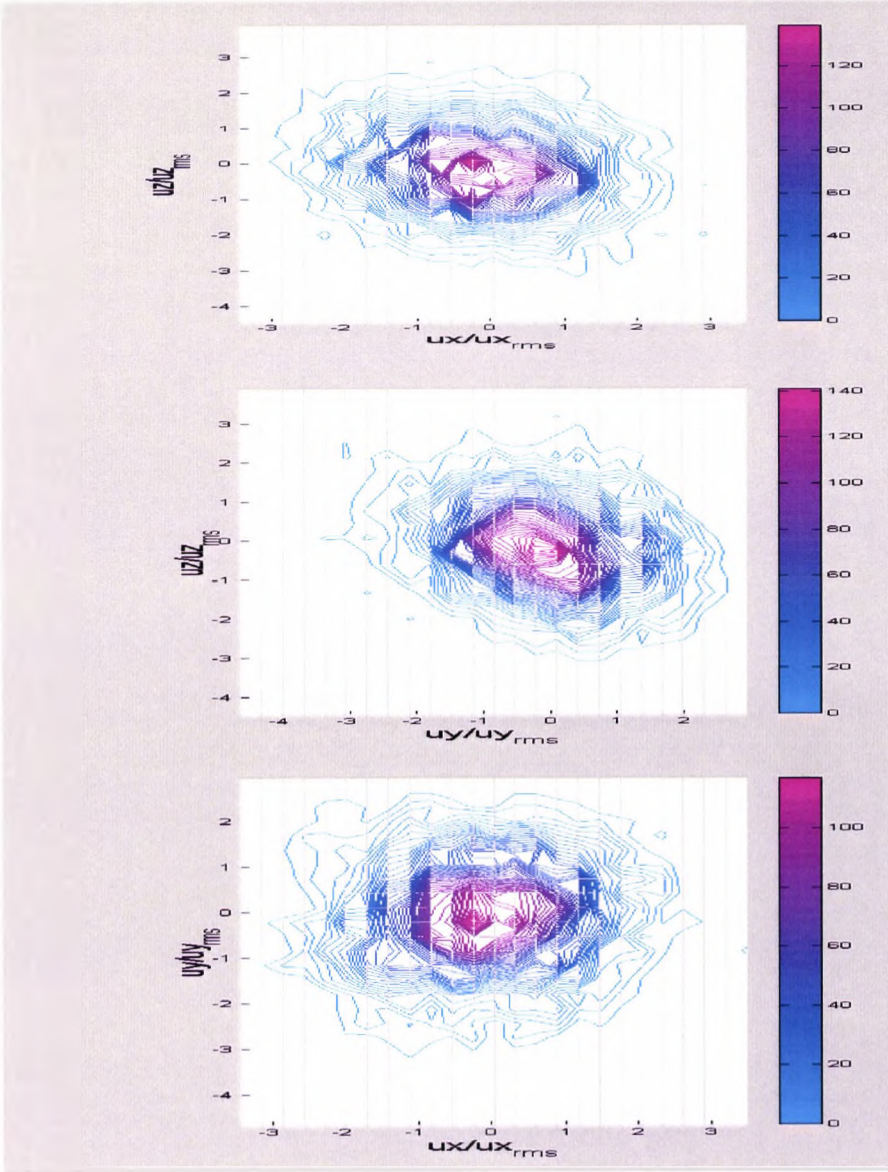

Figure 5.1.3-16 Joint probability distribution functions at z/D =

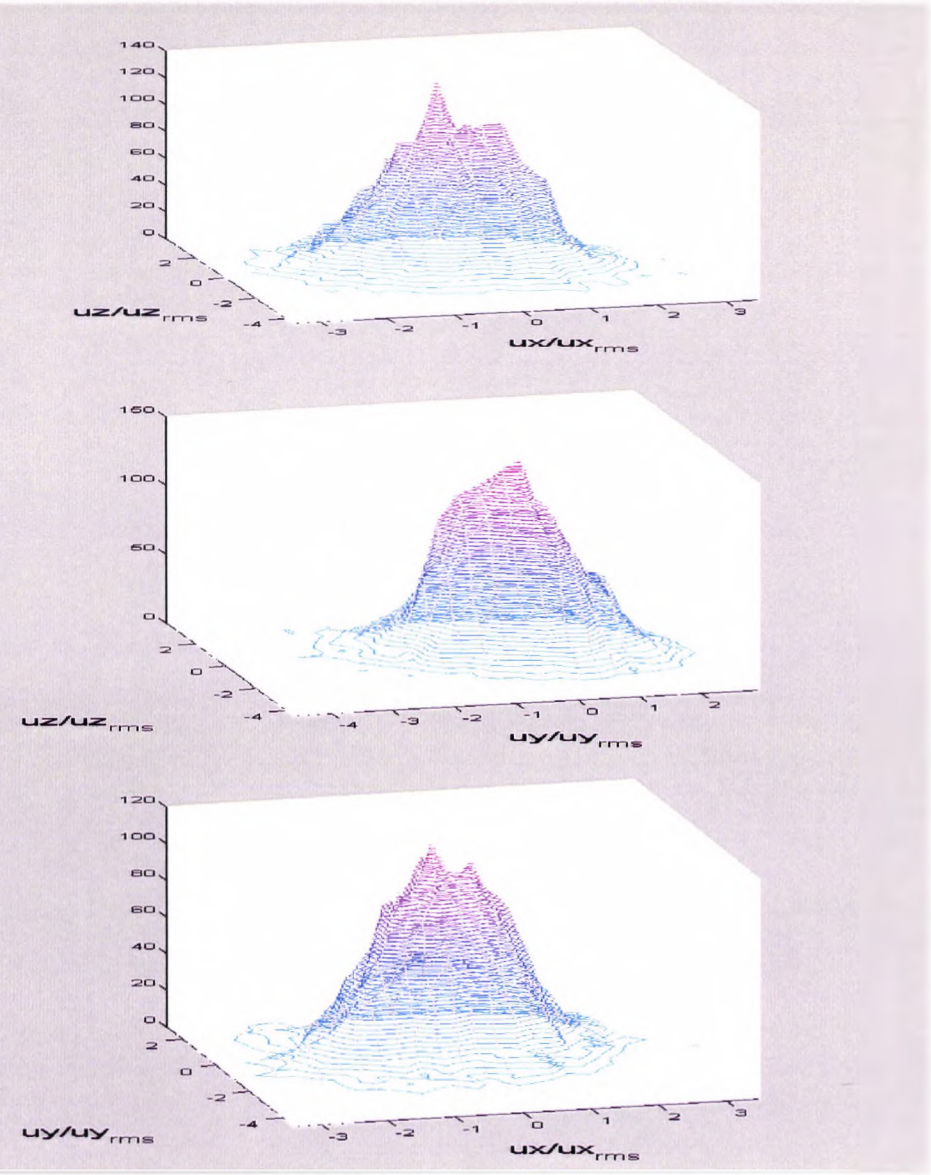

= 1.15, x/D = 11.425, y/D = 0

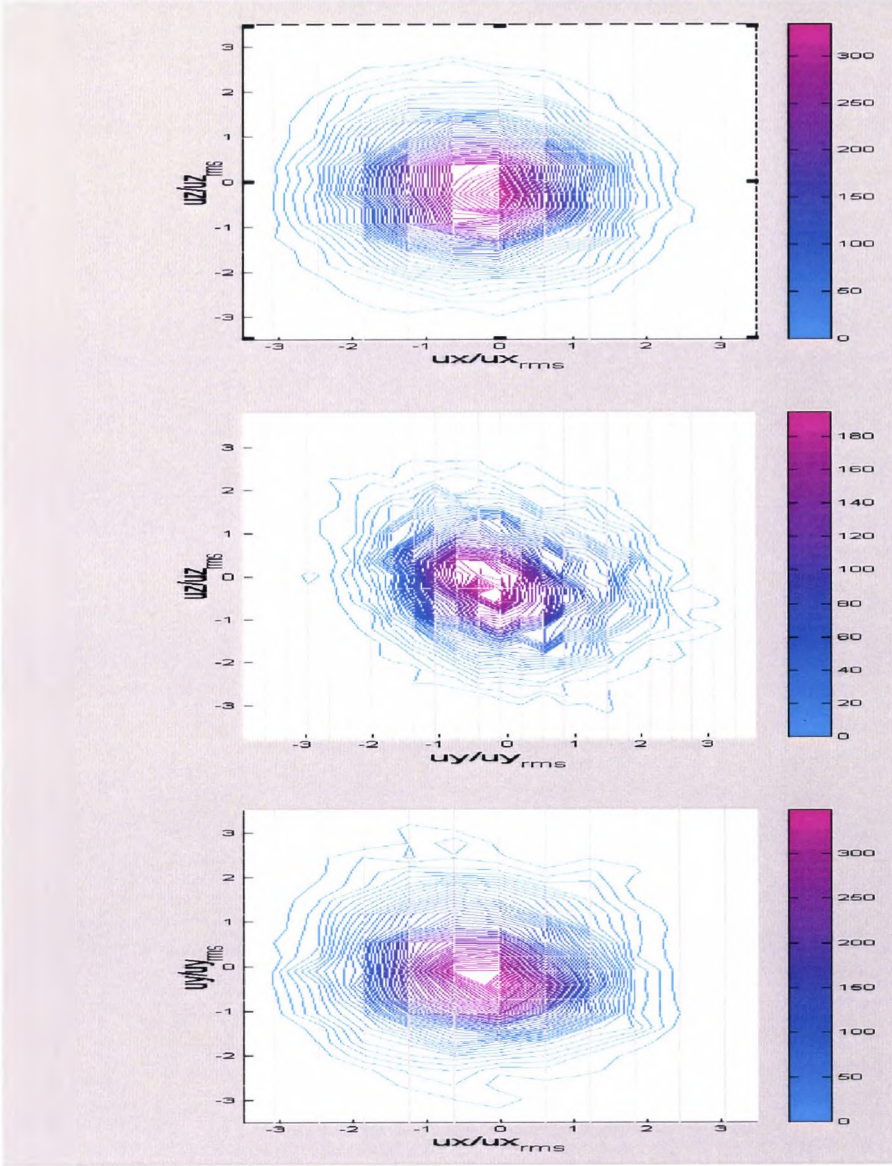

Figure 5.1.3-17 Joint probability distribution functions at z/D =

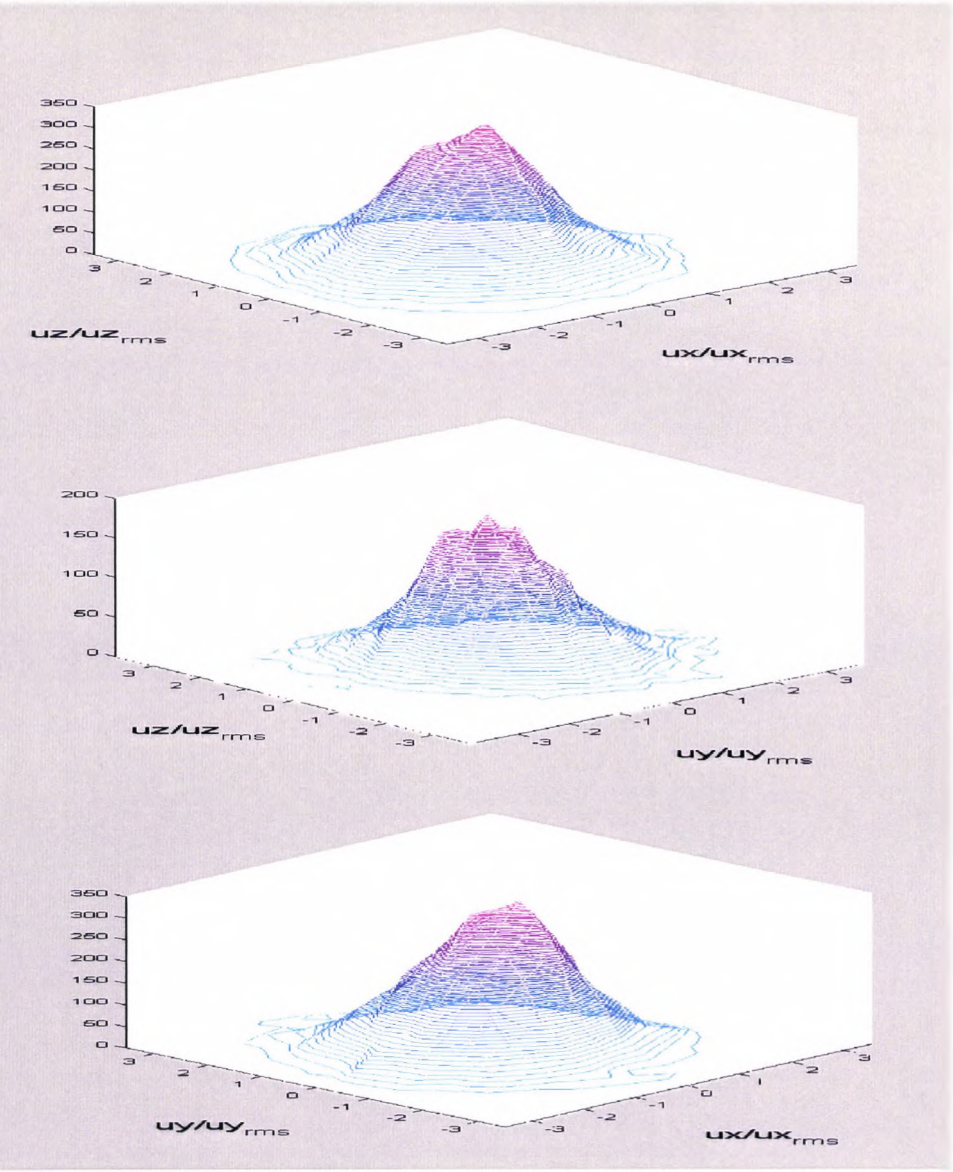

= 0.38, x/D = 11.425, y/D = 0.

5.2 Coherent Structure Identification and Characterization

The presence of coherent structures is suspected to play a significant role in process of influencing the temperature distributions in the flow. Thus, methods for the detection and characterization of these structures are desirable. The following two sections will investigate the applicability of the power spectra density profiles and the WAG algorithm for the detection of the coherent structures. A conclusion will be made as to whether these conventional tools are applicable under an irregularly sampled velocity LDA data set.

5.2.1 Spectral Analysis

The spectral profiles act as an added tool for the preliminary step in assessing whether or not periodic structures appear at the measurement point. The appearance of periodic (or quasi-periodic) structures would allow the analyst to identify optimal regions in the flow for more in depth study such as the application of varying coherent structure identification techniques to extract quantitative information. Profiles of the PSD obtained using the method introduced in section 4.3 is given in figures 5.2.1-1 to 5.2.1-2 with the remaining profiles given in Appendix E.

Obtaining the PSD through the techniques presented in section 4.2.1 implies that one first obtained the ACF. Possessing the ACF allows one to estimate the

Taylor microscale by using a 2nd order parabolic fit. The results have already been presented in section 5.1.1 and appear in figure 5.1.1-15.

Coherent Structure Identification

Figures 5.2.1-1 to 5.2.1-4 illustrate cases in which noise in the signal has contributed to the introduction of artificial information. Three frequency components appear to exist at 12 Hz and 30 Hz. Using dimensional and physical arguments, a characteristic frequency of an eddy structure passing a given measurement position can be estimated using the following (Ewing, 2002)

(5.2.1-1) $$f^* \approx \frac{(0.4 \cdot l)}{0.6 \cdot U_c} \approx 1\,Hz$$

where *l* is the local characteristic length scale and U_c is the centreline velocity. Thus, the frequency components greater than 10 Hz do not appear to be physically real but rather artifacts introduced by the signal. However, the process of diagnosing the possible faults of the signal is not trivial. The identification of noise in an LDA system is complex since it has many areas during its validation and recording of a velocity signal to manifest itself. However, the assessment from section 5.1.1 suggests the existence of low data rates and noise in the signal (evidence of multiple validation issues). The effects of low data rate in the measurement system as shown in table 5.1.1-1 and can be understood from the equation given below

(5.2.1-2) $$N_p = N_t \cdot \frac{\Delta\tau}{t_o} = T_m\left(\frac{\Delta\tau}{t_o^2}\right)$$

where N_p is the average total number of lag-products in each slot width used in the computation of the ACF, N_t is the total number of velocity measurements in the time series, T_m is the total measurement time, $(\Delta\tau/t_o)$ corresponds to the probability of finding a value within a slot width $\Delta\tau$ since $(1/t_o)$ is the mean data-rate (van Maanen, 2000). Thus, it can be seen that the total number of products N_p is proportional to the data rate squared and low data rate results in a low number of observations in a particular slot to estimate the correlation coefficient. The resulting consequence is a high variance estimate that essentially determines the 'noise-level' in the PSD estimate. Higher noise levels are degrade the interpretation of the PSD as they obscure the properties of the small-scale structures in the flow (van Maanen, 2000).

Thus, the spectral plots do not appear to suggest the existence of any periodic or quasi-periodic coherent structures. However, the effects of noise and low data-rates in the measurement data cannot make this conclusion absolute. The methodology of obtaining the ACF/PSD using the local normalization with fuzzy correlation appear to be sound (Benedict et al., 1998), however the quality of the output of the tool remains to be dependent on the quality of the LDA data.

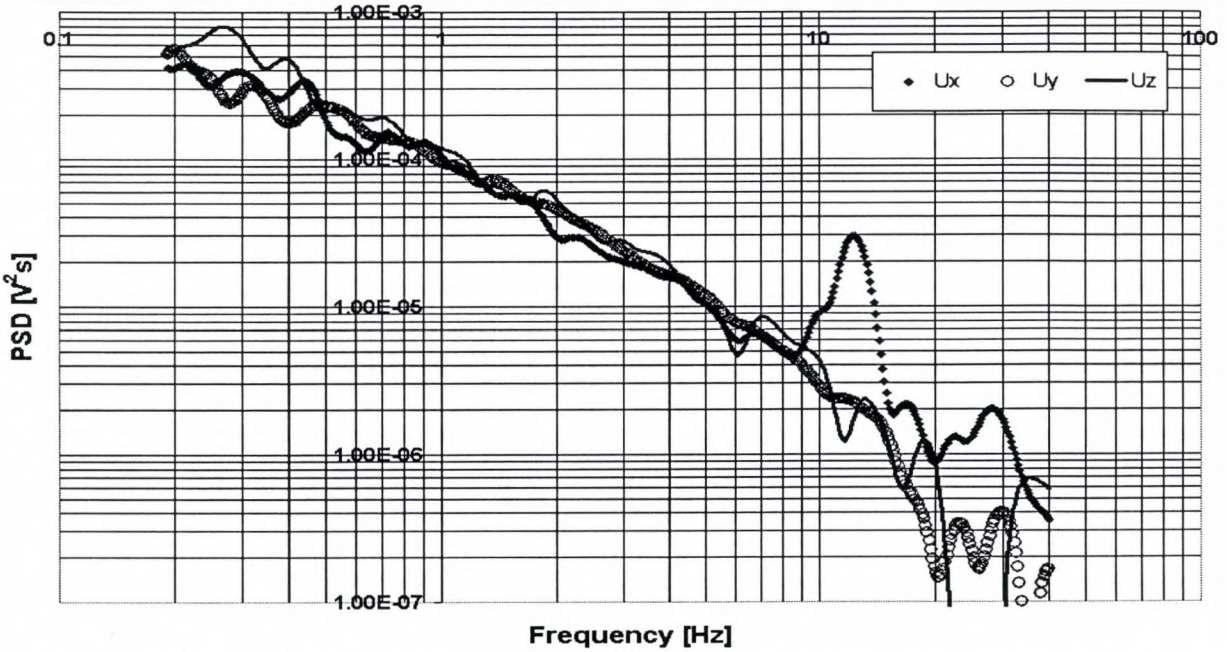

Figure 5.2.1-1 Power Spectral Density profile at z/D = 5.0, x/D = 11.42, y/D = 0.

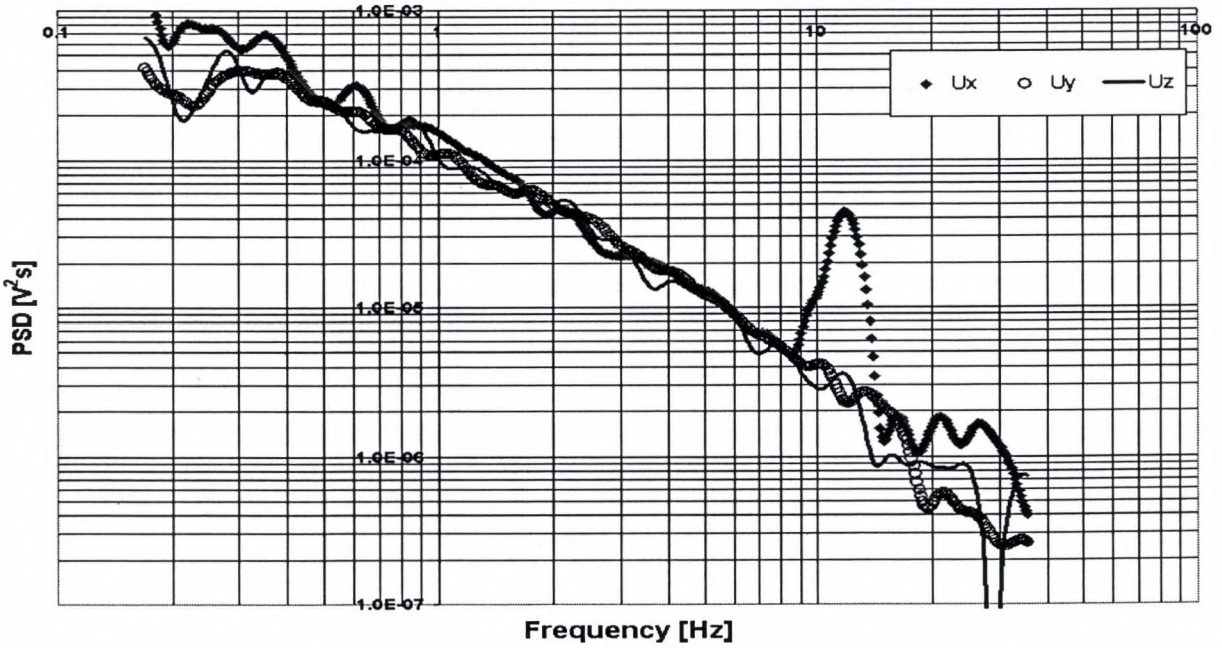

Figure 5.2.1-2 Power Spectral Density profile at z/D = 4.23, x/D = 11.42, y/D = 0.

5.2.2 Window Average Gradient (WAG)

Technical issues were encountered when applying a detection algorithm to a non-ideal signal. Modifications to the algorithm were discussed in section 4.3. The WAG algorithm does not appear to be an ideal detection scheme in an irregularly sampled data set as a closer inspection revealed that many events appear to elude the detection algorithm due to the irregularly sampled nature of data. However, mean properties of the periods in which an event was detected were still achievable using the assumptions presented in section 4.3. A threshold of 75% of the RMS value of the vertical fluctuating component was used for all measurement positions. The results of the detected events are presented in the following section.

The turbulence properties were obtained during a detected realization with an intermittency factor of approximately 16%. The value for this intermittency factor appears to be reasonable. This finding can be understood due to the following:

1. Intermittency decreases with increasing distance from the jet exit due to structural decay (Clark et al., 1981).
2. Smaller structures may also appear due to the effects of stratification (Atsavapranee et al., 1997).

Furthermore, the local characteristic velocity was taken to be the local mean maximum velocity U_m, which corresponded to the axial centreline velocity of the hot jet of 0.081cm/s. This process was completed since the mean velocity of the

entrained fluid into a vortex core is proportional to the characteristic velocity, and thus it was used to non-dimensionalize the following results.

Mean Properties of the Detected Structures

An investigation of the mean properties of the coherent structure allows one to assess whether a preferred motion exists for the coherent structure. The incoherent components appear to have values similar to those of the conventionally computed values. This result can be understood since the intermittency factor was low (typically 16% at z/D = 1.15) resulting in the flow to be essentially dominated by the incoherent (or at least, the undetected) fluid.

The axial velocity profile is given in figure 5.2.2-1. It appears that only a small deviation from the conventionally computed value was observed. This result suggests that the coherent structure has an axial velocity that increased only slightly and in the direction of the flow. The axial velocity profile was also able to suggest that the two jets are shearing each other in the region between z/D = 1.92 and z/D = 0.38 where a change in velocity direction is evident.

Figure 5.2.2-2 illustrates the mean transverse direction of a detected realization. The effects of the detection algorithm may explain the behaviour of the results since the detection scheme triggered on the passage of a coherent structure was based on sudden changes in the upward or downward direction. Thus, it

appears that the two effects averaged each other out, resulting in a mean value that is nearly equivalent to the conventionally computed value.

Figure 5.2.2-3 provides the lateral velocity component in the flow. For an axisymmetrical jet, the lateral velocity should be approximately be zero. For the given system, it appears that a slight bias exists for measurement positions at z/D = 1.15 and downwards towards the cold jet at z/D = -1.92. A possible (or at least partial) explanation for this deviation may be due to the results indicated in figure 5.1.3-13 which suggests that the jet exit velocity is not perfectly distributed at the centre of the jet but has a much faster exit velocity in the negative y/R position. However, the true cause for the deviation remains unclear.

Momentum Transfer

As discussed in section 2.1, Reynolds stresses are essential features in a turbulent flow for the transfer of momentum and its contribution to the turbulent kinetic energy. Figures 5.2.2-4 to 5.2.2-9 illustrate conditionally averaged Reynolds stresses for the shear and normal components. To quantify a coherent structure's contribution to the mean transfer of momentum, one can use equation 4.2-11 and 4.2-12, which is the ratio of the conditionally averaged shear stress as obtained from a coherent structure, to the conventionally computed value.
The results are shown in figures 5.2.2-10 and 5.2.2-11 for the shear and normal components respectively.

It is interesting to observe the results obtained from the conditionally averaged values of the Reynolds shear stresses in the $-u_x u_z$ direction as shown in figure 5.2.2-4. Significant turbulence production appears to be present at x/D = 1.15 when a coherent structure was detected.

In addition, the shear stress of $-u_y u_z$ as shown in figure 5.2.2-5 also appears to be significant in the interaction zone. This result may be consistent with the work presented by Piccirallo et al. (1997) which suggests that the effect of buoyancy forces was the suppression in the transfer of vertical velocity energy but less suppression in the axial and lateral direction. However, the present result would require further investigation to properly conclude this effect.

Figure 5.2.2-10 provides quantitative values for the contribution that each detected event makes to the mean flow. It is interesting to note that at the interaction zone (x/D = 1.15), the passage of a coherent structure resulted in a contribution of approximately 30% to the transfer of momentum in both the $-u_x u_z$ and $-u_y u_z$ components.

Results from the conditionally sampled Reynolds normal stresses were shown in figures 5.2.2-7 to 5.2.2-9. As expected, the normal stresses had values that were generally much smaller than those of the Reynolds shear stresses. However, the dominant component was the normal stress in the transverse direction (figure 5.2.2-8), which shows a contribution to the mean flow of nearly 32%. These results are in agreement with results obtained by Bonnet et al. in

the collaborative test of the plane, incompressible, fully developed turbulent two-stream mixing layer who found a contribution of 40% in the Reynolds shear stress $-u_y u_z$ component (Bonnet et al., 1998). The smaller values obtained in the present experiments as compared to those from Bisset et al. may be expected due the significant effects of stratification which were noted previously to lead to reduction in the size of the vortex structure.

Contributions that a detected realization had to the turbulent energy in the u_i component of turbulent energy were also investigated using equation (4.2-10). These results are summarized in figure 5.2.2-11 and suggest that the axial u_x velocity component in general was the main contributor to the turbulent energy. However, at the interaction zone of z/D = 1.15, it was the lateral u_y which resulted in the most significant gain. The data suggests that the transverse component made a contribution that was approximately eight times larger than that of the axial or the vertical components. Again, this result appears to be consistent with the current model of the effects of stratification on the shear flow (Piccirallo et al., 1997).

The turbulent kinetic energy of the flow is obtained using the equation given below:

(5.2.2-1) $$\overline{\frac{1}{2}q^2} = \frac{1}{2}\left(\overline{u_x^2} + \overline{u_y^2} + \overline{u_z^2}\right)$$

The results suggest that the detected event has a significant amount of turbulence kinetic energy.

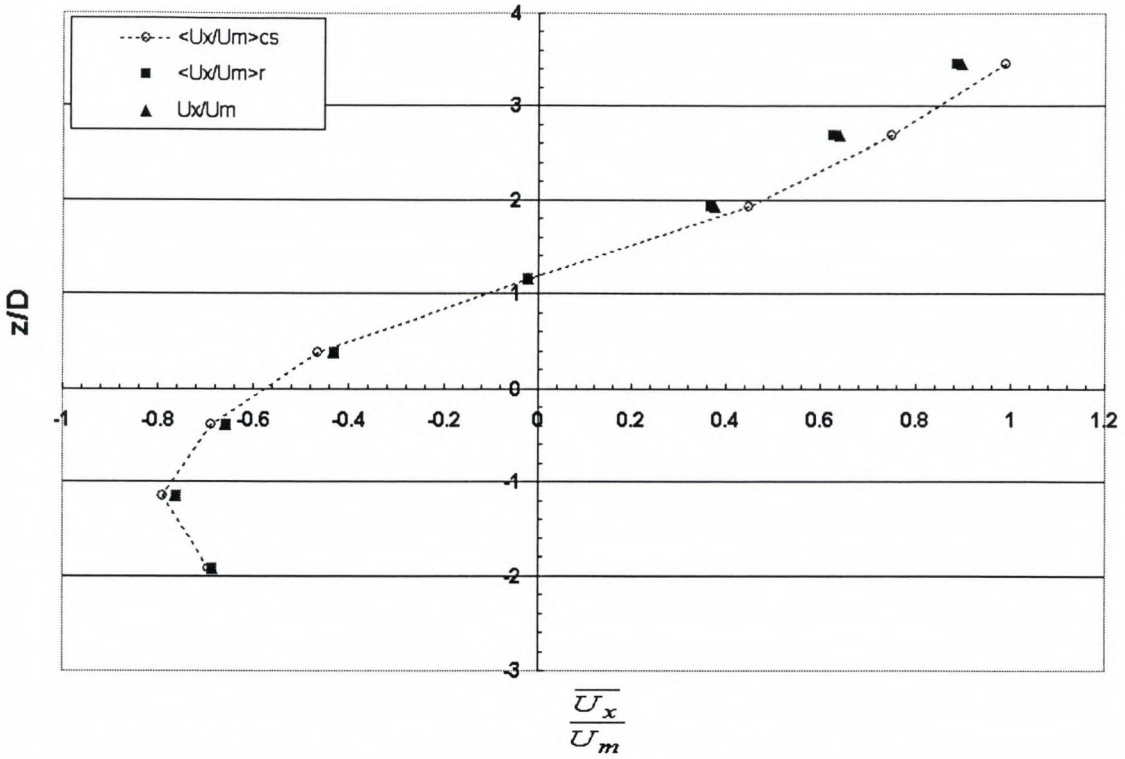

Figure 5.2.2-1 Mean axial velocity Ux along x/D = 11.425, y/D = 0. Measurements were taken at different time periods. Lines are drawn for visual aid purposes only.

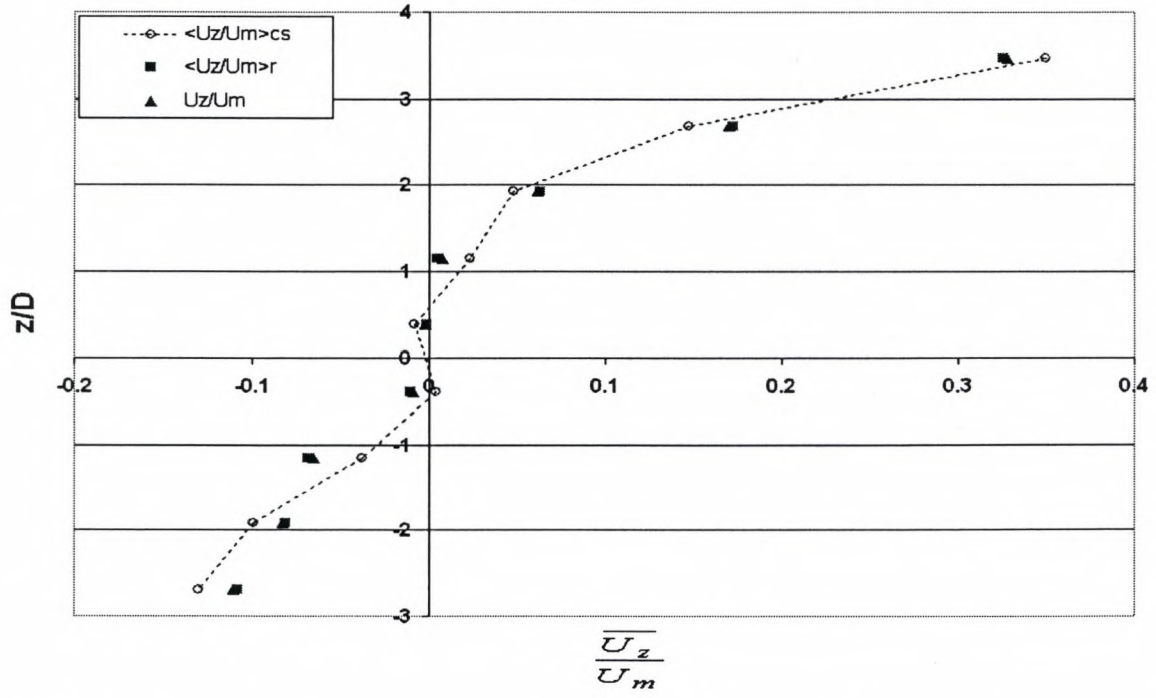

Figure 5.2.2-2 Mean transverse velocity Uz along x/D = 11.425, y/D = 0. Measurements were taken at different time periods. Lines are drawn for visual aid purposes only.

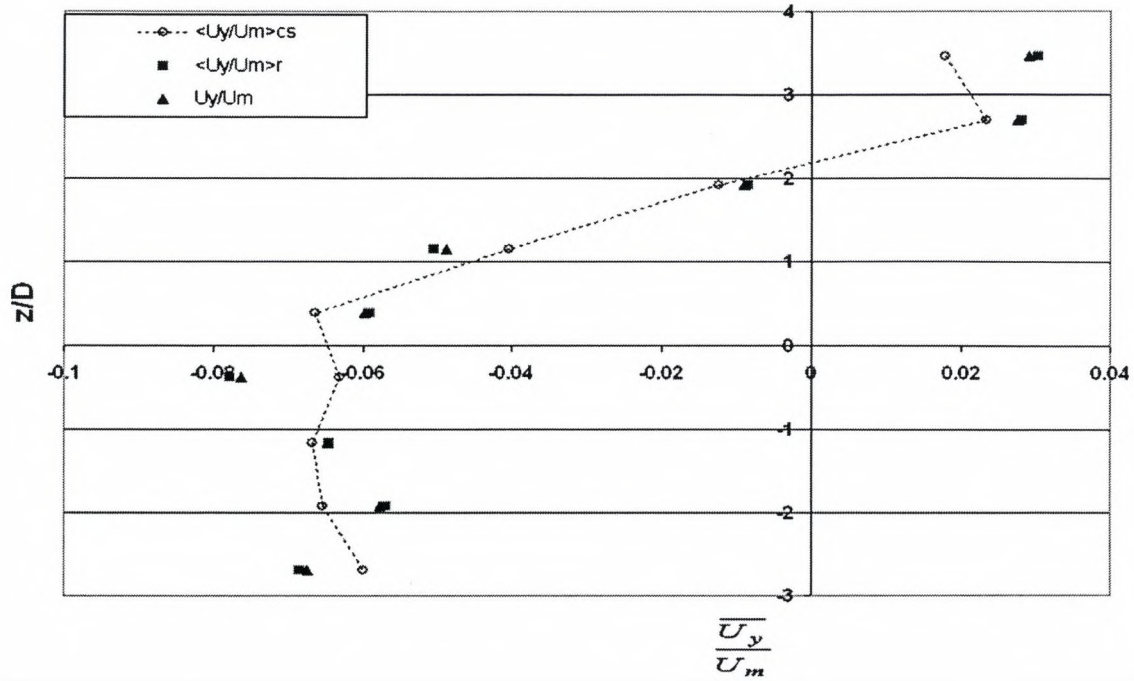

Figure 5.2.2-3 Mean lateral velocity along x/D = 11.425, y/D = 0. Measurements were taken at different time periods. Lines are drawn for visual aid purposes only.

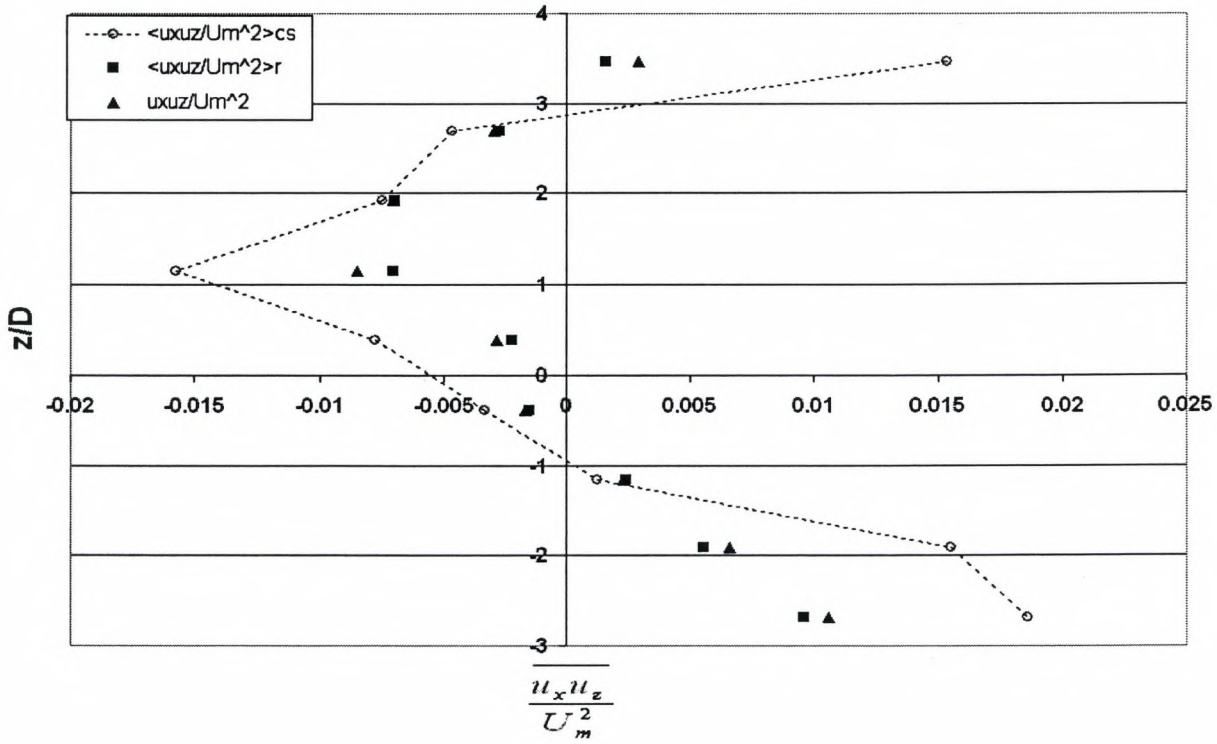

Figure 5.2.2-4 Reynold Shear Stress UxUz along x/D = 11.425, y/D = 0. Measurements were taken at different time periods. Lines are drawn for visual aid purposes only.

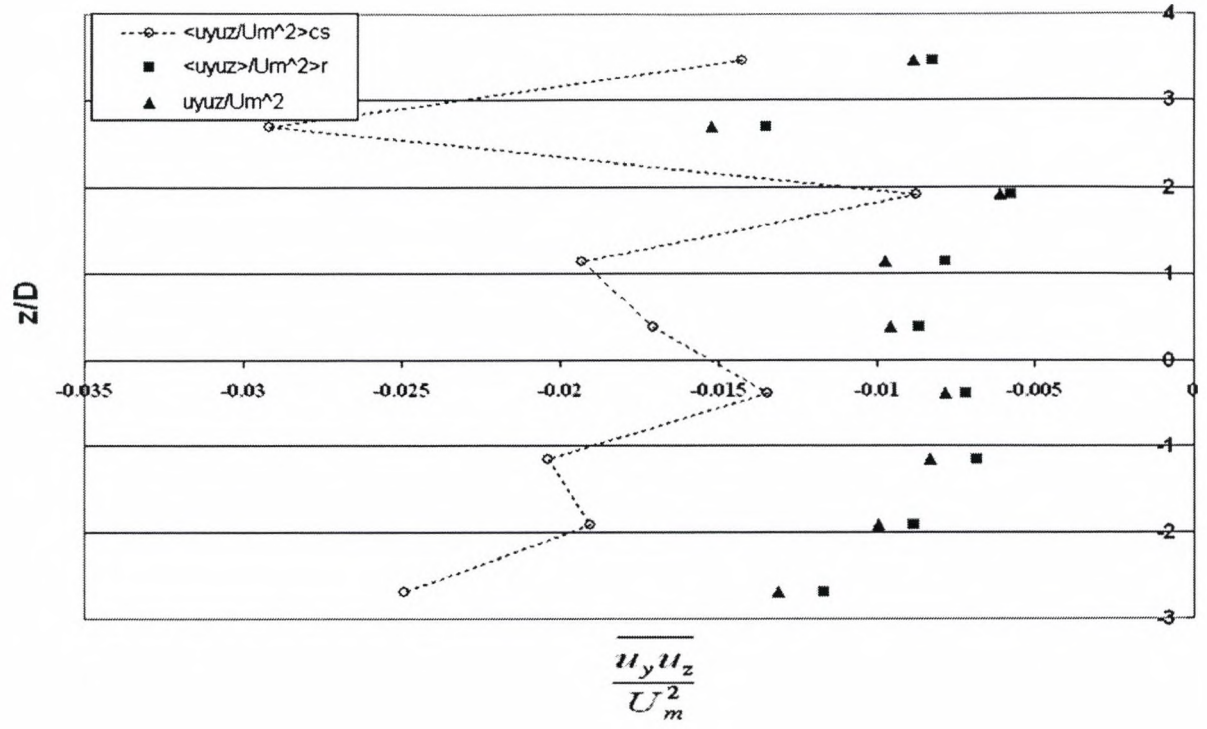

Figure 5.2.2-5 Reynolds Shear Stress UyUz along x/D = 11.425, y/D = 0. Measurements were taken at different time periods. Lines are drawn for visual aid purposes only.

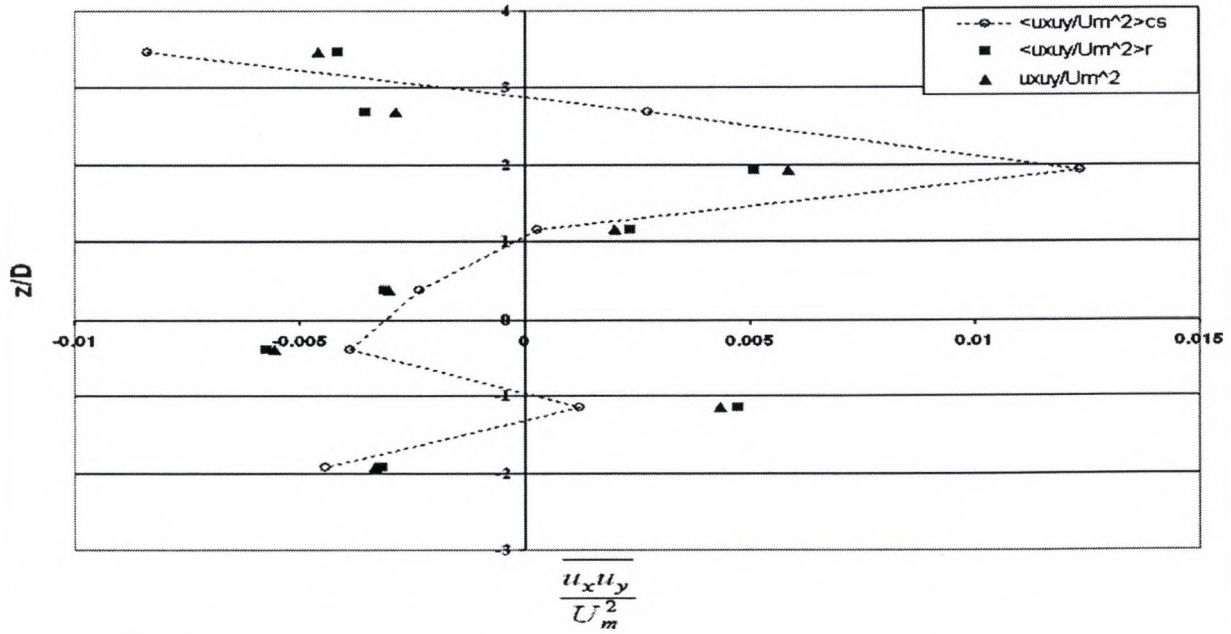

Figure 5.2.2-6 Reynolds Shear Stress: UxUy along x/D = 11.425, y/D = 0. Measurements were taken at different time periods. Lines are drawn for visual aid purposes only.

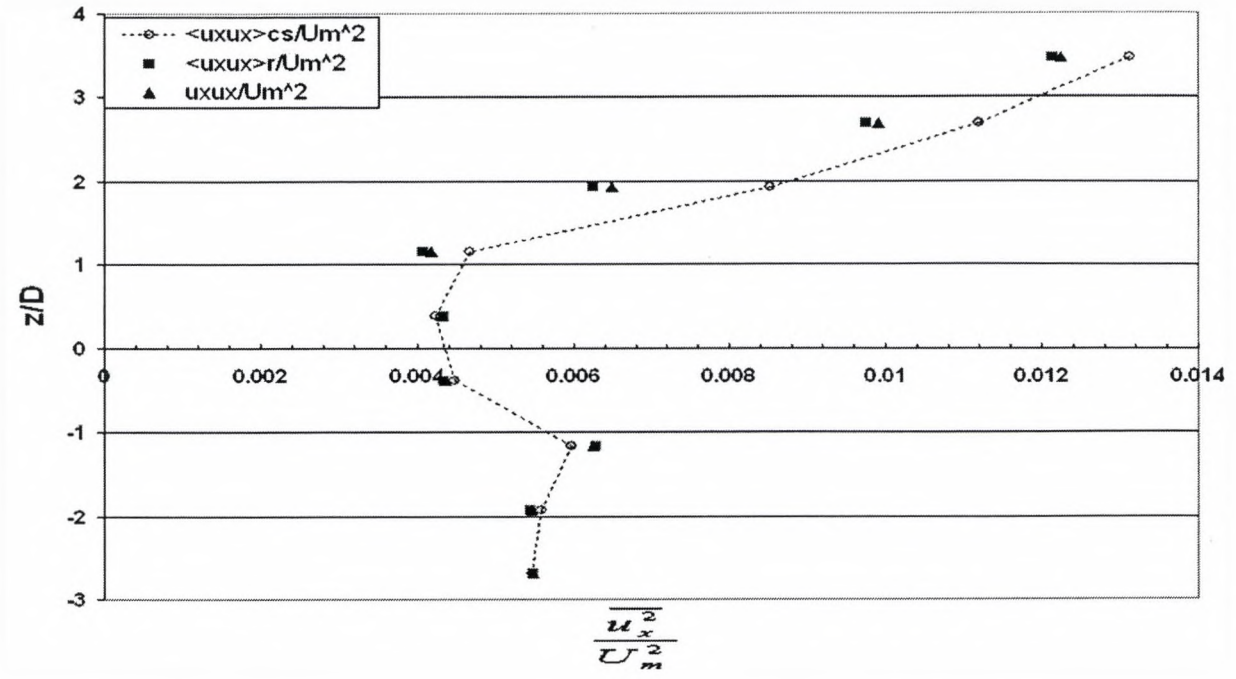

Figure 5.2.2-7: Reynolds Normal Stress in the axial component along x/D = 11.425, y/D = 0. Measurements were taken at different time periods. Lines are drawn for visual aid purposes only.

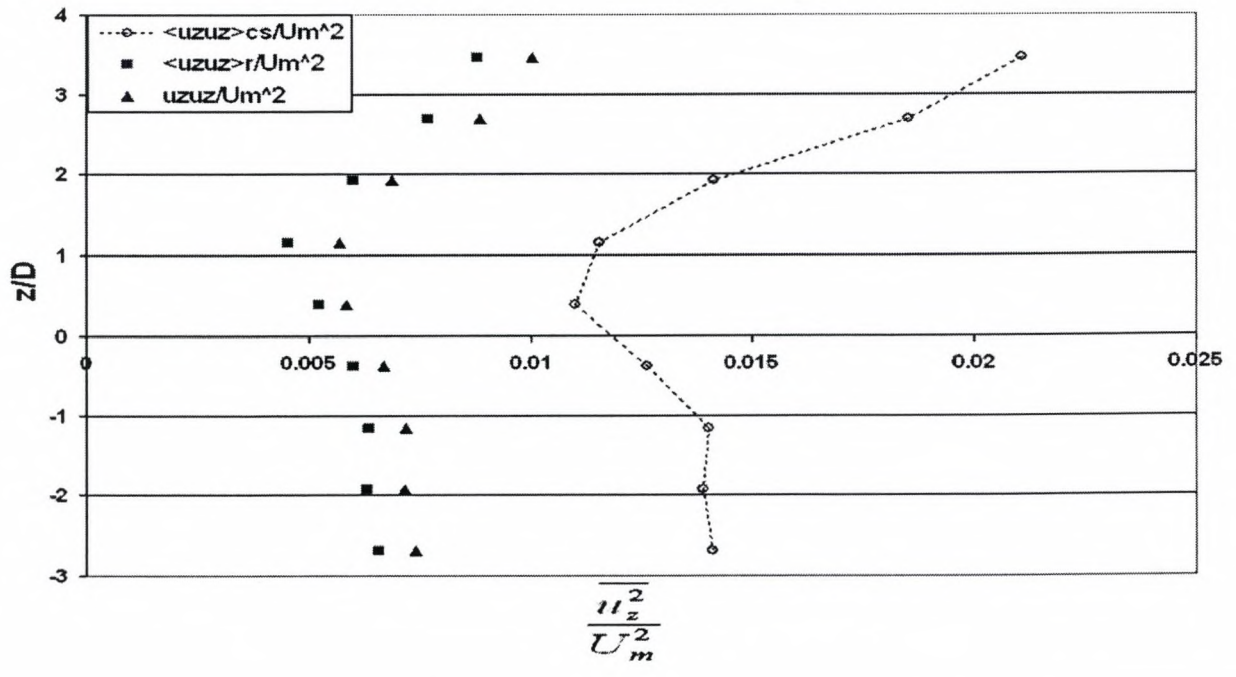

Figure 5.2.2-8 Reynolds Normal Stress of the transverse component along x/D = 11.425, y/D = 0. Measurements were taken at different time periods. Lines are drawn for visual aid purposes only.

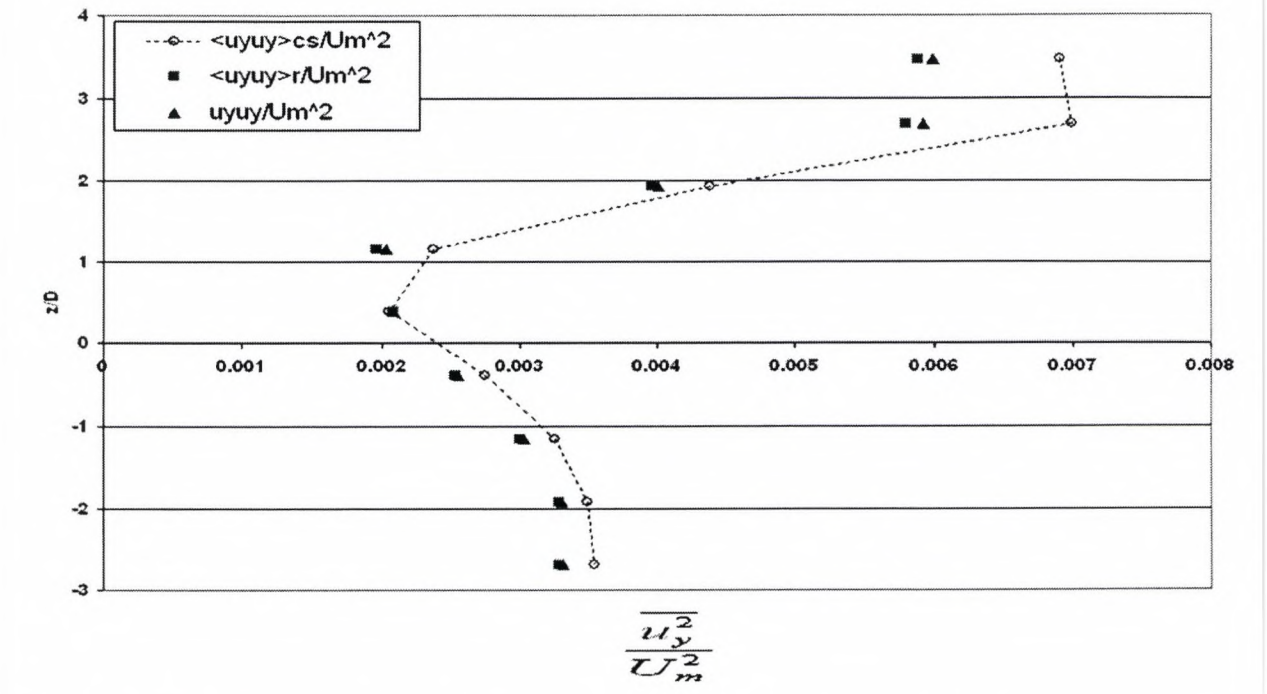

Figure 5.2.2-9 Reynolds Normal Stress of the lateral component along x/D = 11.425, y/D = 0. Measurements were taken at different time periods. Lines are drawn for visual aid purposes only.

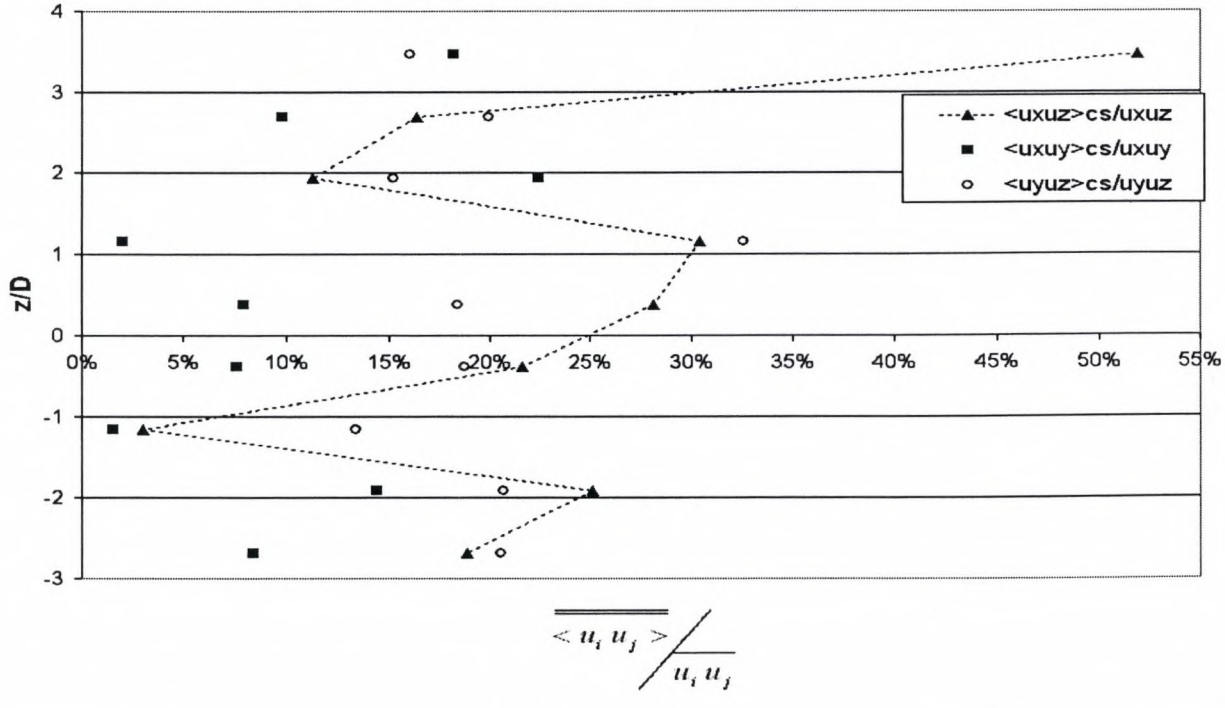

Figure 5.2.2-7 Contribution to Shear stress (absolute): along x/D = 11.425, y/D = 0. Measurements were taken at different time periods. Lines are drawn for visual aid purposes only.

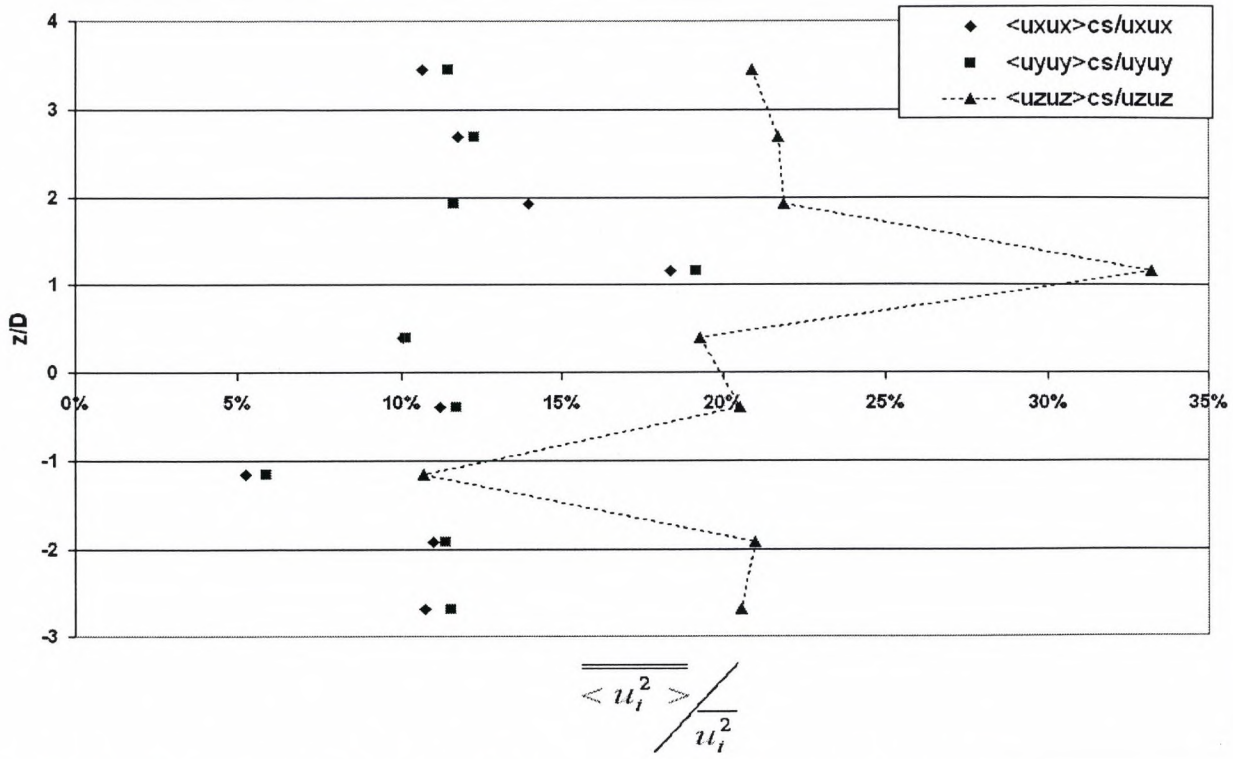

Figure 5.2.2-10 Contribution to Normal Stress (absolute) along x/D = 11.425, y/D = 0 . Measurements were taken at different time periods. Lines are drawn for visual aid purposes only.

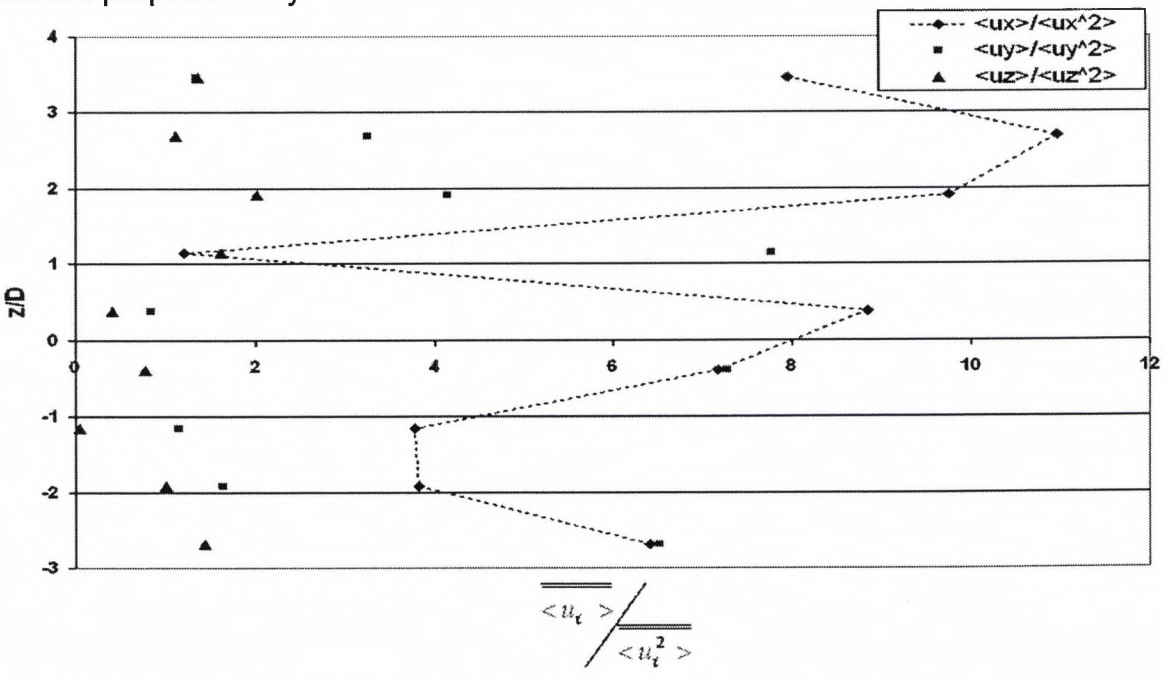

Figure 5.2.2-11 Contribution to turbulent kinetic energy (absolute) along x/D = 11.425, y/D = 0. Measurements were taken at different time periods. Lines are drawn for visual aid purposes only

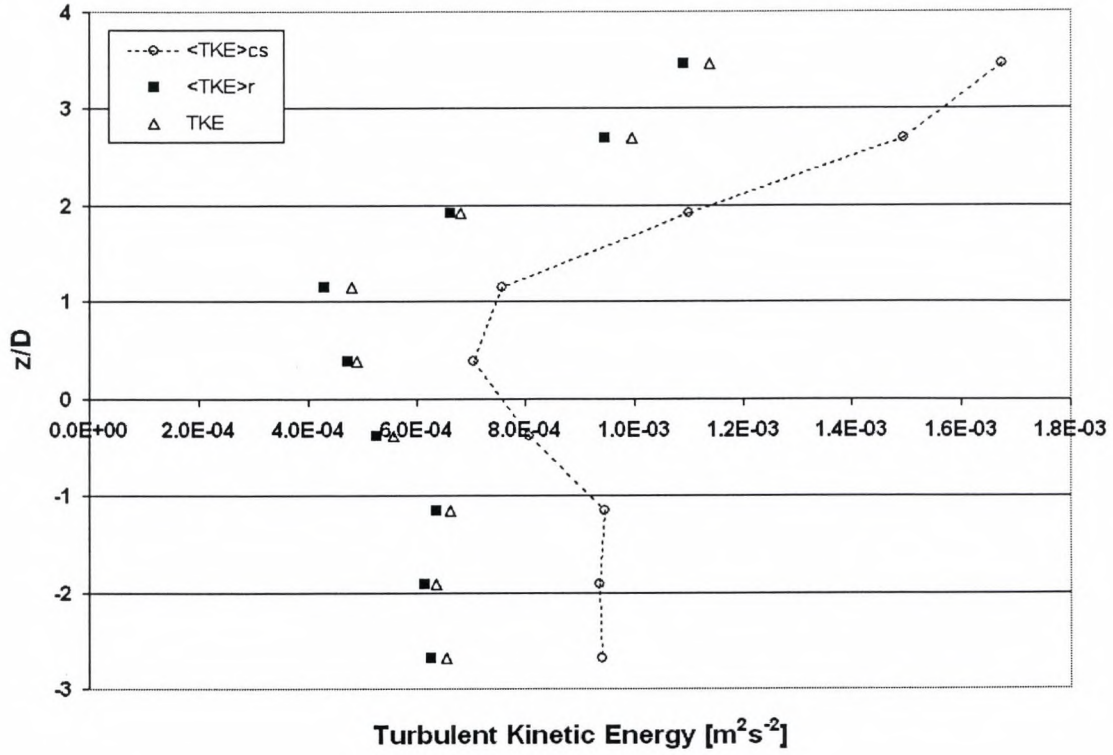

Figure 5.2.2-12: Turbulent kinetic energy of the flow along x/D = 11.425, y/D = 0. Measurements were taken at different time periods.

6.0 Conclusions

Experimental Data Assessment

- The current experimental design and low sampling frequencies in the velocity and temperature measurements are fully sufficient in obtaining the mean statistical properties of the flow.
- Further retrieval of smaller scale turbulence properties and the study of the intermittent behavior of the hot/cold jet interaction were limited due to the spatial and temporal limitations in the measurements.
- The qualitative assessment of the velocity LDA data suggests that measurement data appear to be sufficient in regions of low turbulence intensities (z/D = 6.5 to z/D = 2.7). As the measurements approached the interaction region of two jet shear layers (z/D = 1.92 to z/D = -1.92), problems associated with significant velocity bias, multiple validation issues and low data rates did not allow proper retrieval of turbulence properties such as the Taylor microscale and integral time scale.
- As the LDA measurements approached the interaction region (z/D = 1.92 to z/D = -1.15), the data rate significantly degraded and thus a lower mean Nyquist frequency was determined (as low as 4 Hz at z/D = -1.15).
- The grid spacing between thermocouples was not optimal. For the stationary thermocouples, the measurements were not located in the region, which properly captures the interaction of the hot and cold jet shear layers.
- A sampling frequency of 0.2 Hz in the thermocouple measurements was lower than the characteristic frequency of the jet (5 Hz at the jet exit and 1 Hz

at the interaction region of two jet shear layers) and thus the retrieval of turbulence time and spatial scales could not be completed without the risk of aliasing effects.

- For the moving thermocouple, the large spatial separation (77% of the jet diameter) was insufficient to apply a reliable conditional sampling statistical model to explain the intermittent behavior of the interacting shear layers.
- The interaction of two jet shear layers (x/D = 12.7) resulted in significant stratification that appears to span nearly two jet diameters in the vertical direction from z/D = 1.7 to z/D = -0.28. A contributing factor to the stratification in the vessel is the design of the experiment. It appears that the top region of the jet was designed with four flow exits, which results in a bias to maintain the temperature of the cold jet by draining only the hotter fluids.
- Temperature distributions exhibited significant skewness and large variances at temperature measurements near the interaction zone of two jet shear layers. The non-uniform distribution may be a result of entrainment of fluids from one jet shear layer into the other. However, a bimodal distribution could not be observed which is most likely due to the coarse sampling frequency and due to the fact that the measurements were not located in the region of the interaction of the two jets.

Coherent Structure Identification

- Spectra profiles were inconclusive in the detection of periodic or 'quasi-periodic' structures. Possible effects due to noise resulted in a degraded ACF and PSD estimate.
- The methodology of obtaining the PSD under an irregularly sampled data set using the local normalization with fuzzy correlation, appears to be sound (Benedict et al., 1998). However the quality of the output of the tool remains to be dependent on the quality of the LDA data.
- The WAG algorithm was affected by the irregularly sampled data when the LDA data had significant delays between one record data point to the next. Consequently, an ambiguous estimate of the time duration of a passing structure resulted and led to a higher probability that an event would elude the detection scheme.
- For all detected realizations using the WAG algorithm, the presence of coherent structures was suggested to appear at the interaction region of two shear layers with an intermittency factor of 16.4%.
- The results suggest that approximately 30% of the mean momentum transfer across the jet in both $-\overline{u_x u_z}$ and $-\overline{u_y u_z}$ components were due to the presence of the coherent structures.
- In addition, the contribution that a coherent structure had to the turbulent kinetic energy in the lateral component was nearly 8 times larger than the contributions to the axial or transverse direction. These results are consistent with the results obtained by Piccirillo et al. (1997) who suggested that the

effects of buoyancy suppressed vertical transfer of energy in the fluctuating velocity component, but less in both the axial and lateral directions.

7.0 Recommendations

- A decrease in the spatial positions of the stationary thermocouples is recommended. Currently, the thermocouples are spaced nearly two jet diameters apart. It has been shown that the effects of a high Reynolds number and stratification result in 1) short survival times of a coherent structure, and 2) a reduced vortex size. Thus, a spatial grid less than half a jet diameter may be appropriate.
- Additional stationary temperature measurements in the region between z/D = 1.56 and z/D = -0.24 would be ideal to capture the behavior of the interaction of the two jet shear layers.
- Decreasing the spatial position between the moving thermocouple and the LDA velocity measurements to less than half a jet diameter and increasing the sampling frequency of the thermocouple to approximately the same sampling frequency as the LDA measurements would be beneficial in developing a temperature/velocity statistical model.
- Figure 3.1-5 illustrates that the lateral velocity measurements could be better utilized if measurements were taken closer to z/D = 1.15. This result may assist in evaluating whether or not coherent structures in a stratified flow are biased to transfer lateral energy.
- The non-ideal performance of the WAG algorithm applied under the irregularly sampled data set suggests that the development of tools that

explicitly account for the irregularly sampled data such as the second-generation wavelet transform (Swelden, 1995) should be investigated.

- The development of a Monte-Carlo simulation to simulate an LDA signal would be beneficial to better verify the reliability of a coherent structure identification tool in an irregularly sampled setting.
- Since the application of Hot-wire Anemometers are non-ideal for flows with significant flow reversal and strong temperature gradients, the application of the particle image velocimetry (PIV) may provide an alternative technique for the retrieval of quantitative turbulence properties in highly turbulent flows.

8.0 References

Adrian, RA., (1978) *Estimation of LDA Signal Strength and Signal-to-Noise Ratio* TSI Quarterly, v.IV, No.1

Atsavapranee, P., Gharib,M., (1997) *Structures in stratified plane-mixing layers and the effects of cross-shear* J.Fluids Mech. v.342 p.53-86.

Auburn, S. Boisson, HC., Bonnet, JP., (2002) *Further Characterization of large-scale coherent structure signatures in a turbulent-plane mixing layer.* Exp.Fluids v.32. p.136

Aubry, N, Holmes, O., Lumley J., Stone, E., (1988) *Dynamics of coherent structures in the wall region of a turbuelnt boundary layer.* J.Fluid Mech. v.192. p.115-173

Benedict, LD., Nobach, H., Tropea,C., (2000) *Estimation of turbulent velocity spectra from laser Dopplerdata* Meas.Sci.Technol. v.11 p.1089-1104

Benedict, LH., Nobach, H., Tropea, C., (1998) *Benchmark tests for the estimation of power spectra from LDA signals* Proc. 9th Int.Symp.on Applications of Laser Technology to Fluid Mechanics (Lisbon) paper 32.6.

Bisset, DK., Antonia., RA., Browne, L., (1990) *Spatial organization of large structures in the turbulent far wake of a cylinder* J.Fluid Mech. v.218 p.439-461.

Bonnet, JP., Deville, J., Glauser, N., Antonia, RA., Bisset, DK., Cole, DR., Fiedler, HE., Garem, JH., Hilberg, J., Jeong, J., Kevlahan, NKR., Ukeiley, LS., Vincendeau, E., (1998) *Collaborative testing of eddy structure identification methods in free turbulent shear flows.* Exp. Fluids v.25. p.197-225.

Bonnet, JP., Glauser, N., (editors) (1993) *Eddy structure identification in free turbulent shear flows Proc. IUTAM symp – Poitiers Octover 1992* Kluwer Academic Publishers, Dordrecht, p.311-324.

Boussinesq, J., (1903) *Theorie Analytique de la Chaleur. V.2 Gauthier-Villars Paris*

Breidenthal, R., (1980) *Response of plane shear layers and wakes to strong three-dimensional disturbances. Phys Fluids* v.23 p.1929.

Broersen, P.M.T., Waele, S.de., Bos., R., *The accuracy of time series analysis for Laser Doppler Velocimetry* 10th International Symposium on Application of Laser Techniques to Fluid Mechanics, Lisbon., July 10-13, 2000

Brown, GL., Roshko, A., (1974) *On density effects and large structure in turbulent mixing layers* J.Fluid Mech. v.64. p. 775-816.

Clark., AR., Hussain, F. (1981) *On the coherent structure of the axisymmetric mixing layer: a flow visualisation study.* J.Fluid Mech. v104. p.263-294

Erdmann, JC., Gellert, RI.,(1976) *Particle Arrival Statistics in Laser Doppler Anemometry of Turbulent flow* Applied Physics Letters, v.29 p.408-411.

Ewing, D., (2002) *Private communication,* Hamilton, Canada.

Feller, W., (1966) *An introduction to Probability Theory and its applications vol.I* (New York: Wiley).

Ferre, J., Giralt, F (1993) *A comparison of different analytical techniques for identifying structures in turbulence. In: Eddy structure identification in free turbulent shear flows Proc. IUTAM symp – Poitiers October 1992 (Bonnet JP, Glauser, M editors) Kluwer Academic Publishers, Dordrecht, p.181-194.*

George,W., Beuther, PD., Lumley,JL., (1979) *Processing of Random Signals* Proc.Dynamic Flow Conf.

Gerz, T., Schumann, U., Elghobashi, SE., (1989) *Direct numerical simulation of stratified homogeneous turbulent shear flows.,* J.Fluid Mech. v.200. p563-594.

Glauser, MN., George, WK (1987) *An orthogonal decomposition of the axisymmetric jet mixing layer utilizing cross-wire velocity measurement* Proc 6th Symp Turbulent Shear Flows, Toulouse

Glauser, MN., George, WK (1992) *Application of multipoint measurements for flow characterization.* Exp. Thermal Fluid Sci. v.5 p.617-632.

Hussain, F. (1986) *Coherent structures and turbulence* J.Fluid Mech. v.173 p303-356

Kevlahan, N., Hunt., J., Vassilicos, J., (1993) *A comparision of different analystical techniques for identifying structures in turbulence. In: Eddy structure identification in free turbulent shear flows Proc. IUTAM symp – Poitiers Octover 1992 (Bonnet JP, Glauser, M editors) Kluwer Academic Publishers, Dordrecht, p.311-324.*

Khartabil, H.F., (2001a) *Buoyancy Testing Facility Description and Commissioning* AECL documentFFC-32000-CSO-003, FFC-FCT-329 (Rev.0)

Khartabil, H.F., (2001b) *Interaction of Two-Non-isothermal Round Jets: Test Plan.* AECL document.FFC-32000-TP-004, FFC-FCT-330 (Rev.0)

Khartabil, H.F., (2001c) *Interaction of Two-Non-isothermal Round Jets: Test Report.* AECL document FFC-32000-TR-004, FFC-FCT-328 (Rev.0)

Konrad, JH., (1976) *An experimental investigation of mixing in two-dimensional turbulent shear flows with applications to diffusion-limited chemical reaction. PhD. Thesis,* California Institute of Technology

Lachance, Y.F.,(1999) *Moderator Test Facility - Data Acquisition and Storage System Description* , FFC-FCT-146-,MTF-00M61-90200, February.

Lee, P.E., (1999) *The TSI Three-dimensional Laser Doppler Velocimetry System: Experimental Set-up, Operating Procedure and Data Analysis* FFC-FCT-240, RC-2309, October.

Lehmann, P., Schone, A., (1997) *Estimation of the Signal-to-Noise Ratio of Laser Doppler Signals* Proceedings of the 7th International Conference "Laser Anemometery: Advances and Applications", Karlsruhe (Germany), p99 -106.

Mayo, W., Shay, MT., Ritter, S., (1974) *Digital estimation of turbuelence power spectra from burst counter LDV data.* Proc. 2nd Int. Workshop on Laser Velocimeter (Purdue University, 1974) p.16-26.

Mayo, W., (1978) *Spectrum measurements with laser velocimeter* Proc.Dynamic Flow Conf. p.851-868

Menon, R., Lai,WT., (1991) *Key Considerations in the Selection of Seed Particles for LDV measurements.* Fourth International Conference on Laser Anemometry Cleveland, Ohio.

Mumford, JC., (1982) *The structure of the large eddies in fully developed turbulent shear flow. Part 1. The plane jet.* J.Fluid Mech. v.118. p.241.

Nobach, H., Muller, E., Tropea, C., (1998) *Correlation estimator for two-channel, non-coincidence laser-Doppler anemometer.* In Proc.9th Int. Symp. on Appl. of Laser Techn. to Fluid Mechanics, Lisbon, Portugal, paper 32.1.

Otnes, RK., Enochson, L., (1978) *Applied Time Series Analysis volume 1: Basic Techniques.* Wiley-Interscience Publication, New York.

Pawlak, G., Armi, L., (1998) *Vortex dynamics in a spatially accelerating shear layer* J.Fluid Mech. v.376. p.1-35.

Perry, A., Chong, MS., (1986) *A series expansion study of the Navier-Stokes equations with application three-dimensional separation patters.* J.Fluid Mech. v.173 p.273-223.

Piccirillo, P., Van Atta, CW., (1997) *The evolution of a uniformly sheared thermally stratified turbulent flow* J.Fluid Mech. v.334, p 61-86.

Reynolds, AJ., (1974) *Turbulent Flows in Engineering* John Wiley & Sons, London.

Rodi, W. (1982) *Turbulent Buoyant Jets and Plumes* HMT The science and Application of Heat and Mass Transfer Reports, Reviews and Computer Programs Pergamon Press New York.

Rohr., J., Itsweire, E., Helland, K., Van Atta, C., (1988) *Growth and decay of turbulence in a stably stratified shear flow.,* J.Fluid Mech. v.195. p.77-111.

Shinpaugh, KA., Simpson, RL., Wicks, AL., Ha, SM., Fleming, JL., (1992) *Signal Processing Technique for Low Signal-to-Noise Ration Laser Doppler Velocimetry Signals* Exp. in Fluids, v.12, p.319-328.

Sweldens, W., (1996) *The lifting scheme: A construction of second generation wavelets* SIAM J.Math. Anal., v.29 p.511 – 546.

Tennekes, H., Lumley, JL., (1972) *A first course in turbulence* MIT press.

Thoroddsen, S., Van Atta,C., (1992) *The influence of stable stratification on small-scale anisotropy and dissipation of turbulence in stably stratified fluid.* J.Geophys. Res.. v.97 p.3647-3658.

Tummers, M.J., Passchier, D.M., (2000) *Estimation of the spectral density function from randomly sampled LDA data* 10th International Symposium on Applications of Laser Techniques to Fluid Mechanics

Turner, JS., (1973) *Buoyancy effects in fluids* Cambridge University Press Great Britain.

van Maanen HRE., Tummers MJ., (1996) *Estimation of the autocorrelation function of turbulent velocity fluctuations using the slotting technique with local normalisation* Proceedings 8th Int. Symp. on Applications of Laser Technology to fluid Mechanics (Lisbon) paper 36.4

van Maanen, HRE., Oldenziel, A., (1998) *Estimation of turbulence power spectra from randomly sampled data by curve-fit to the auto-correlation function applied to laser-Doppler anemometry.* Meas.Sci.Technol., v.9 p458-467.

van Maanen, HRE, (2000) *Preliminary Diagnostic Testing of LDA Data-sets* 10th International Symposium on Application of Laser Techniques to Fluid Mechanics, Lisbon., July 10-13

Appendix A Experimental Procedure

Experimental plan taken from Khartabil, 2001b.

Step	Activity
A.1	Prepare a list of velocity measurement positions.
A.2	Fill loop with deionised water (or check the desired water level if the loop is already full), perform loop checks (leaks, instrument readings, loop controls). Start the LDV system for warm-up.
A.3	Start the loop using the procedure in [4]. Set the desired nozzle flowrates. Set the temperature for both nozzles to the average of the desired inlet temperatures, to establish the desired initial conditions for the transient part of testing. Wait for loop conditions to stabilize. Start collecting data using the 0.2 Hz scan-rate. Wait for about 10 minutes.
A.4	Using the DAS buoyancy-control screen [4], divert the flows for both nozzles from the vessel and into the return lines. Set the desired temperatures for both nozzles using the procedure in [4].
A.5	Wait until the nozzle temperatures stabilize. Using the procedure in [4], divert the nozzle flows back into the vessel. Continue collecting data, and wait for conditions to stabilize before collecting any velocity measurements. Steps A.3 to A.5 provide repeat transient runs for each test condition.
A.6	Position the LDV measurement volume at the zero reference (geometric centre along the axes of the nozzles, as shown in Figure 4). Check the positions indicated by the FIND software.
A.7	Using the LDV FIND software, set the maximum collection time to 5 minutes. Set the maximum sample size to 30,000.
A.8	Start collecting velocity measurements at the locations specified in step A.1.
A.9	Shut down the loop and the LDV system. Retrieve and analyse the data. Check the results and identify any problems (e.g., wrong LDV settings, unstable loop conditions).
A.10	Repeat steps A.1 to A.9 for subsequent days of testing.
A.11	Following test completion, analyse and document the results in a test report; initiate the review process.
A.12	The procedure is complete.

Note: steps A.1, and A.6 to A.7 are performed only for tests requiring velocity measurements.

Appendix B The Time Interval Distribution (TID)

Under ideal flow conditions, tracer particles are random but homogeneously distributed and follow along the same line will result in a time interval distribution, which obeys a Poisson distribution given in equation (3.2-1).

$$P(\Delta t) = \frac{1}{t_o} e^{\frac{-\Delta t}{t_o}} \qquad (3.2\text{-}1)$$

The profile of the ideal case is plotted on a semi-log plot and given in figure B-1. The procedure used in this report to obtain the TID presented in this report is given in table B-1 and based on the following considerations.

1. The choice of the bin size and resolution were done in an attempt to obtain the greatest number of observations per bin to reduce the statistical variance.
2. The range of 4 to $5t_o$ was used to ensure that a sufficient number of observations were obtainable in the lowest number of bins.
3. The bin resolution was justified as long as it was not less than the resolution of the clock to avoid empty bins.

Table B-1: Procedure for obtaining the normalized TID profiles used in this report
1. Estimate the mean t_o as the total measurement time divided by the total number of samples
2. Establish a distribution range of approximately $5t_o$
3. Obtain a bin resolution of ~5%t_o by using 100 bins in the TID
4. Normalize the distribution by the largest number of observation in the TID
5. Plot the TID under a semi-log scale
6. Obtain a linear fit through the data to obtain a new estimate of t_o
7. Deviations from the linear fit suggests deviations from the ideal

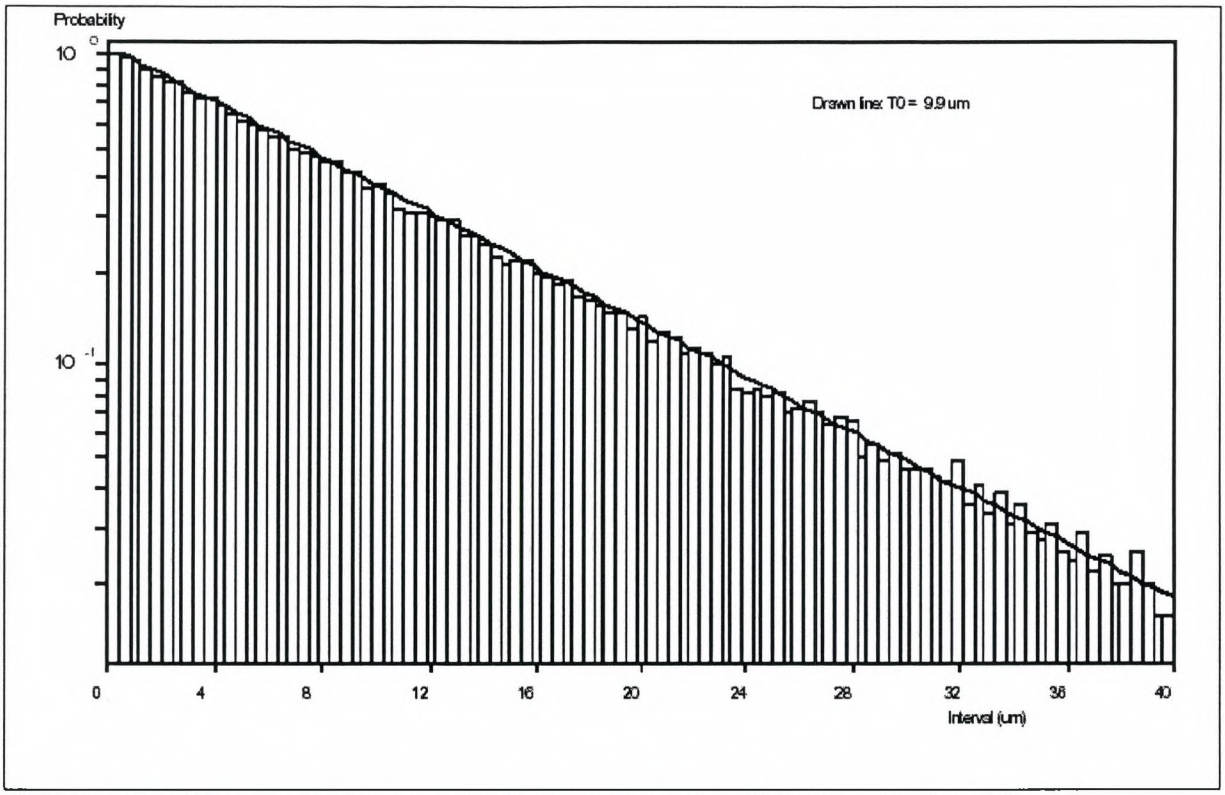

Figure B-1 The ideal Time Interval Distribution function [Illustration taken from van Maanen, 2000]

Appendix C Estimating the ACF/PSD from Irregularly Sampled Data

Two essential concepts made the application of the slotting correlation method possible. The first is the well-known aspect that for a stationary random fluctuation system, the auto covariance function and the power spectrum are each other's Fourier Transforms, given in (C-1) and (C-2) respectively (George, 1979).

(C-1) $$\rho(\tau) = \int_0^\infty F(\omega)\cos(\omega\tau)d\omega$$

(C-2) $$F(\omega) = \frac{2}{\pi}\int_0^\infty \rho(\tau)\cos(\omega\tau)d\tau$$

Secondly, when the flow is homogeneously distributed with tracer particles in a volume of fluid, one can then expect the arrival time-interval of a particle to follow an exponential distribution (Erdmann et al., 1976, Feller, 1966). The implication is that the LDA will provide a high number of short-time interval samples, thus allowing one, in principle, to obtain small-scale information regardless of the data-rate (van Maanen, 1998). These realizations allowed Mayo to formally introduce the slotting correlation technique for estimating PSD from the ACF (Mayo, 1974, 1978).

An overview of the traditional slotting correlation algorithm is given in figure C-1. The discretized auto-correlation function of a random sample is expressed in (C-

3) where the numerator term is the sum of all cross products $u_i u_j$ having a lag time in the interval given in (C-4), and $H(k\Delta\tau)$ is the specific number of cross products appearing within a given slot. The variance is also defined and given in (C-6).

(C-3) $$\hat{\rho}(k\Delta\tau) = \frac{\sum \{u_i u_j\}(k\Delta\tau 0)}{\overline{u(t)^2} H(k\Delta\tau)}; \quad k = 0,1,...,(M-1)$$

(C-4) $$\text{Slot interval}: \left\{k - \frac{1}{2}\right\}\Delta\tau < (t_i - t_j) < \left\{k + \frac{1}{2}\right\}\Delta\tau$$

(C-5) $$\Delta\tau = \frac{\tau_{\max}}{(M-1)}$$

(C-6) $$\overline{u(t)^2} = \frac{1}{N}\sum_{i=1}^{N} u_i^{\,2} = \text{Variance of u(t)}$$

Here, $\Delta\tau$ is the slot width based on the maximum lag time τ_{max} used in the ACF, and M is the total number of slots. Note however, that based on the discussion given in section 3.2, the slot width cannot be smaller than the processor dead time or else empty slots will occur, resulting in erroneous estimates for these particular bins. The $(t_i - t_j)$ term corresponds to the lag time between u_i and u_j. Once the discretized ACF is available, the spectral estimate can be given as

(C-7) $$F_1(\omega) = \frac{\Delta\tau}{\pi}\left\{\frac{1}{2}\hat{\rho}(0) + \sum_{k=1}^{M-1}\hat{\rho}(k\Delta\tau)w(k\Delta\tau)\cos(k\omega\Delta\tau)\right\}$$

where ω is the angular frequency and $w(k\Delta\tau)$ is the lag-window function which is used in an attempt to reduce the spectral leakage and system noise.

Significant drawbacks are generally associated with the traditional slotting technique (Benedict et al., 2000, van Maanen et al., 1996). As a result, the success of the slotting correlation algorithm has never been properly achieved. Improvement on these deficiencies has been proposed and applied by van Mannan and Tummers (1996) by assuming the flow was stationary, and by replacing the variance estimate of equation (C-6) with a local variance estimate particular to each slot given as the following:

(C-8) $$\overline{u(t)^2} = \left(\overline{u(t)^2} \cdot \overline{u(t+\tau)^2}\right)^2 = \frac{\left(\sum \{u_i^2\}(k\Delta\tau)\sum \{u_j^2\}(k\Delta\tau)\right)^{1/2}}{H(k\Delta\tau)}$$

The third term of (C-8) is presented to explicitly outline that the local variance is particular for each slot based on the number of cross-products available. Thus, $H(k\Delta\tau)$ is again defined as the number of cross products appearing within a given slot. The auto-correlation function scaled to the local variance is then given as the following

(C-9) $$\tilde{\rho}(k\Delta t) = \frac{\sum \{u_i u_j\}(k\Delta\tau)}{\left(\sum \{u_i^2\}(k\Delta\tau)\sum \{u_j^2\}(k\Delta\tau)\right)^{1/2}}; \quad k = 0,1,\ldots,(M-1)$$

This technique is referred to as the local normalization algorithm (van Maanen et al., 1996). The PSD is then estimated using (C-7) where (C-9) replaces (C-3). The local normalization technique as introduced thus far, achieved significant improvements in the estimation of the ACF and PSD for small lag times. However, as the lag time increased, the correlation with itself decreases. As a result, the variance of the correlation coefficient (and hence the ACF) significantly increases. Large lag times resulted in an undesirably large variance that was

comparable to the results of the traditional slotting technique (Benedict et al., 1998)

The benchmarking experiment (Benedict et al., 2000) allowed Nobach and van Maanen to realize that the merging of both the local normalization with a fuzzy slotting technique provided a synergistic result. This proposal was due to the fact that local normalization was most effective at small lag times whereas the fuzzy slotting technique achieved a reduced variance estimate at a constant rate at all time lags. Thus, the end result as compared to the traditional slotting correlation technique was an improved, low variance estimate of the ACF and PSD at all lag times.

To apply the fuzzy slotting technique, one computes the usual velocity lag products, however, each lag product is allowed to contribute (with a weighted value) to two slots simultaneously. More weight is given to a lag product if it is closer to the centre of the actual slot. The improvement in the variance estimate can be understood by noticing that the number of cross products appearing in each slot increases. The larger number of samples available increases the statistical confidence level of the estimate of the correlation coefficient within a given slot. Thus, this result consequently decreases the variance in the estimate of the ACF and PSD (Nobach et al., 1998).

The presence of velocity bias has been shown to be the culprit to inducing large variance estimation (Tummers et al., 2000). Thus, the estimation of the ACF and

PSD requires an adequate account of the velocity bias by applying the correction term. The most often used corrector is the transit time ξ, which can be included in the computation of each cross product as given below

(C-10) $$\tilde{\rho}(k\Delta t) = \frac{\sum \{u_i u_j \xi_{ti} \xi_{tj}\}(k\Delta\tau)}{\left(\sum \{u_i^2 \xi_{ii} \xi_{ti}\}(k\Delta\tau) \sum \{u_j^2 \xi_{ii} \xi_{ti}\}(k\Delta\tau)\right)^{1/2}}; \quad k = 0,1,...,(M-1)$$

Using the local normalization technique, the velocity bias affected the ACF estimate by distorting the estimate of the Taylor micro-scale (Benedict et al., 1998).

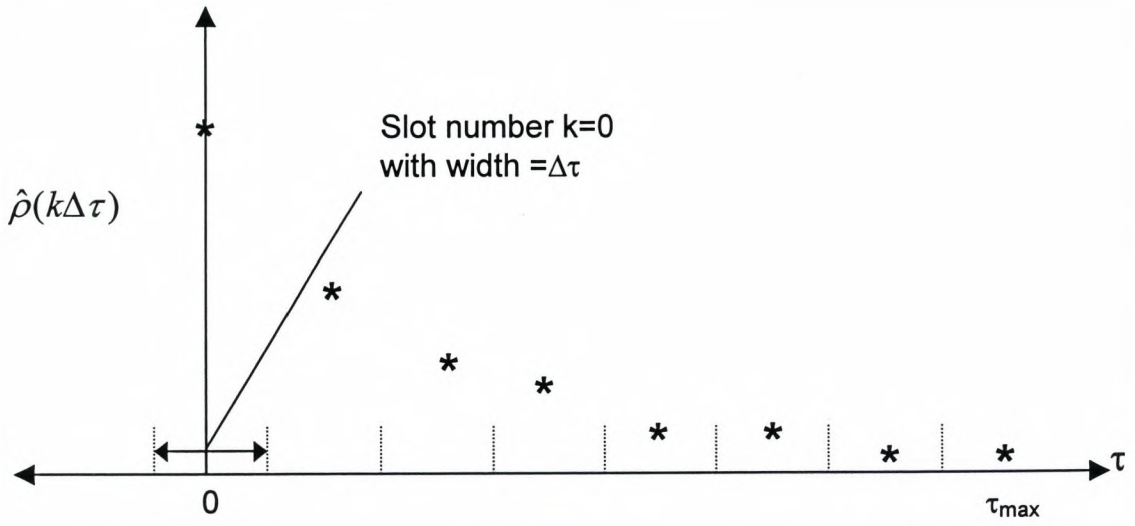

Figure C-1: A visual depiction of the autocorrelation function using the irregularly sampled data. In this example, M=8 and * corresponds to the mean cross-correlation coefficient at slot k.

Appendix D Time Interval Distribution of the Experimental Data

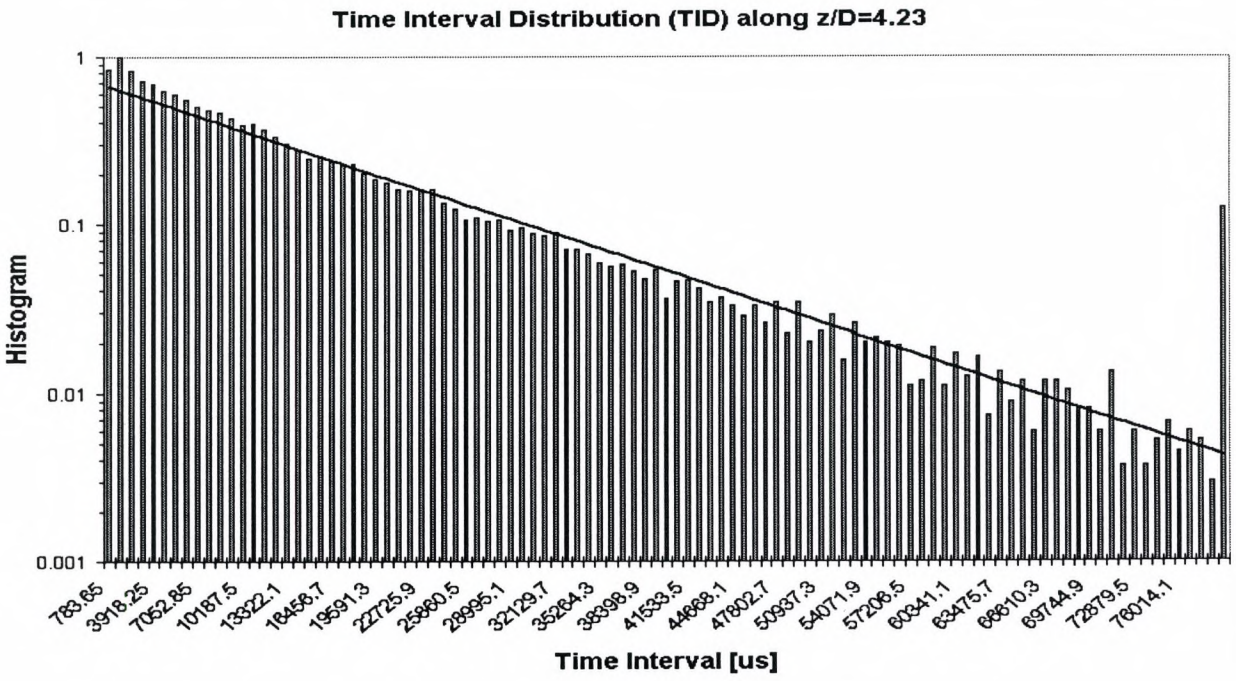

Figure D-1 Time Interval Distribution (TID) at z/D = 4.23

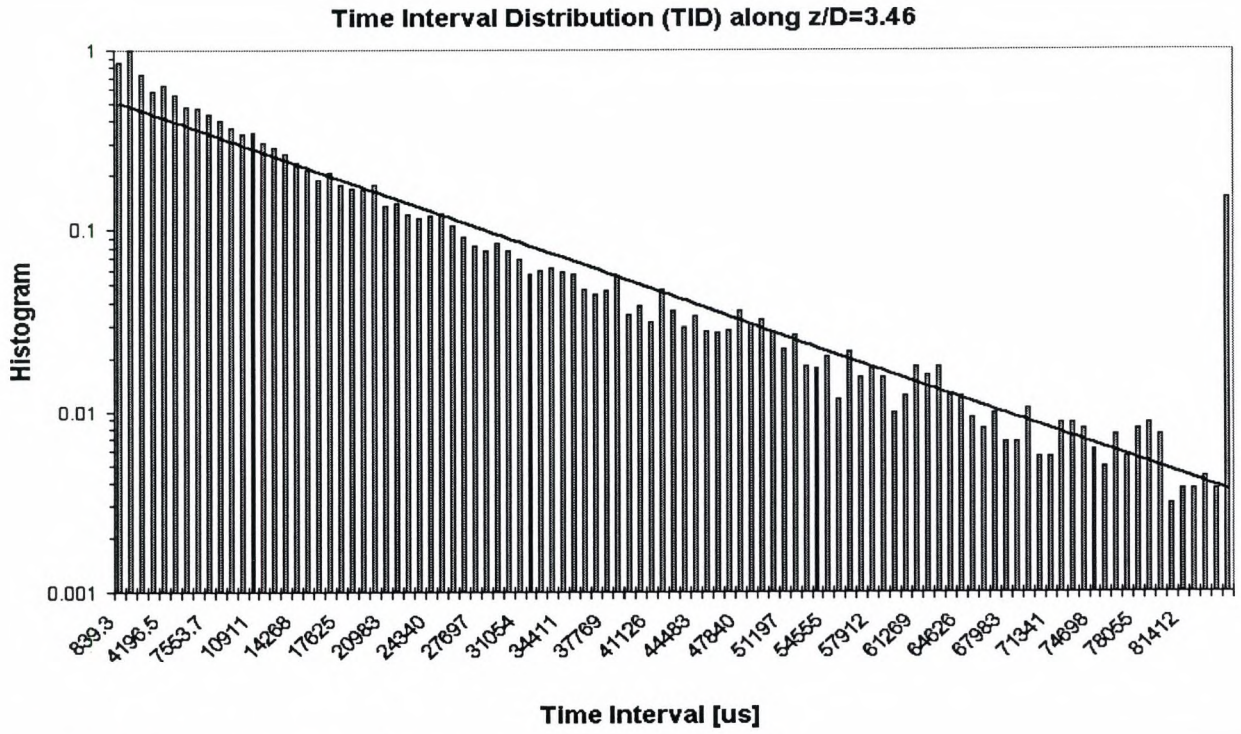

Figure D-2 Time Interval Distribution (TID) at z/D = 3.46

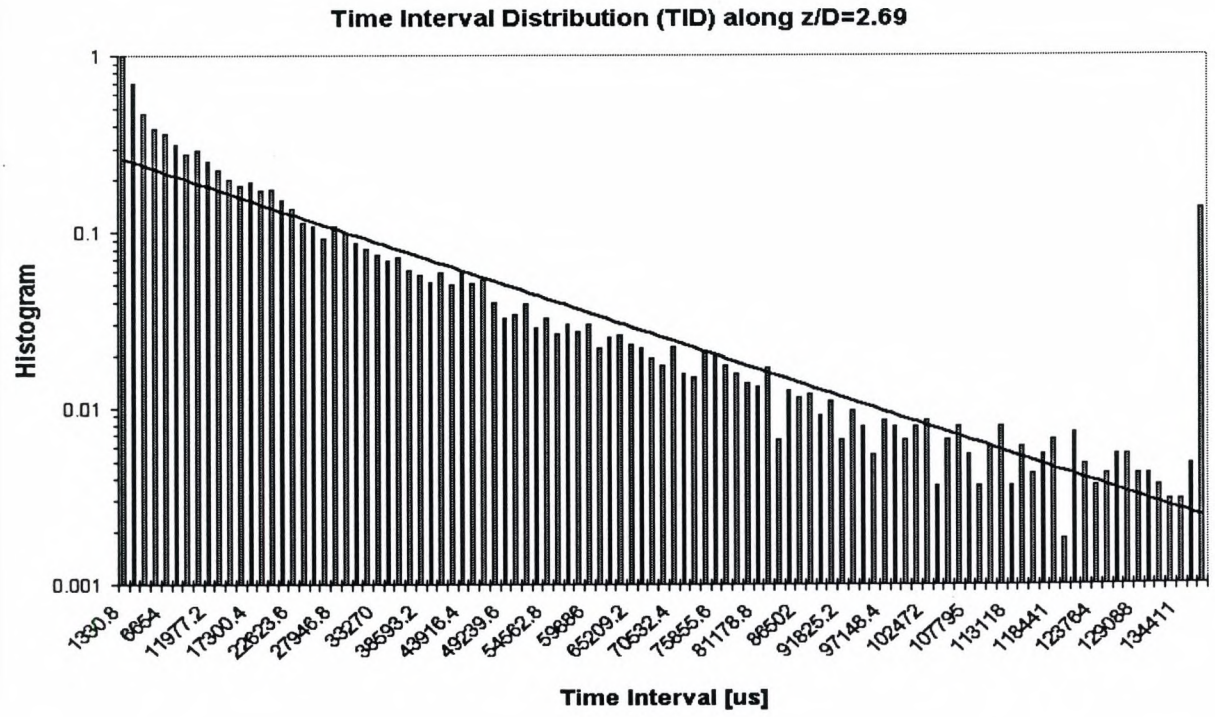

Figure D-3 Time Interval Distribution (TID) at z/D = 2.69

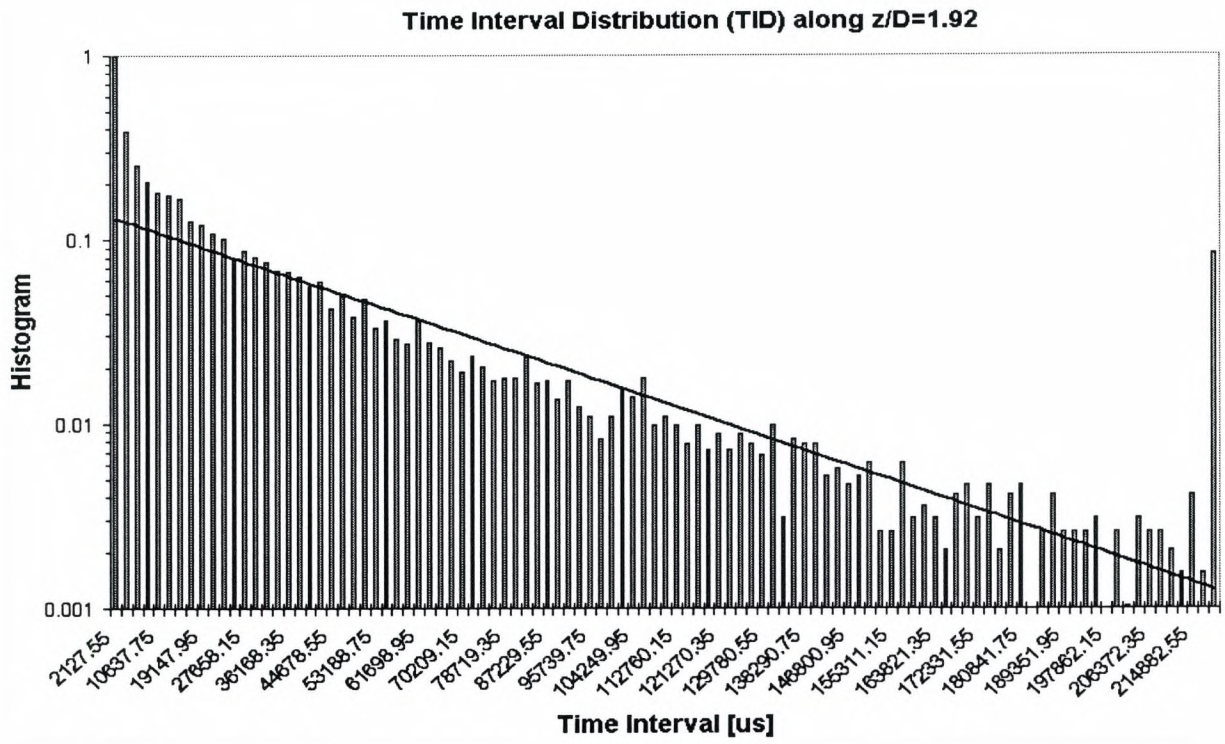

Figure D-4 Time Interval Distribution (TID) at z/D = 1.92

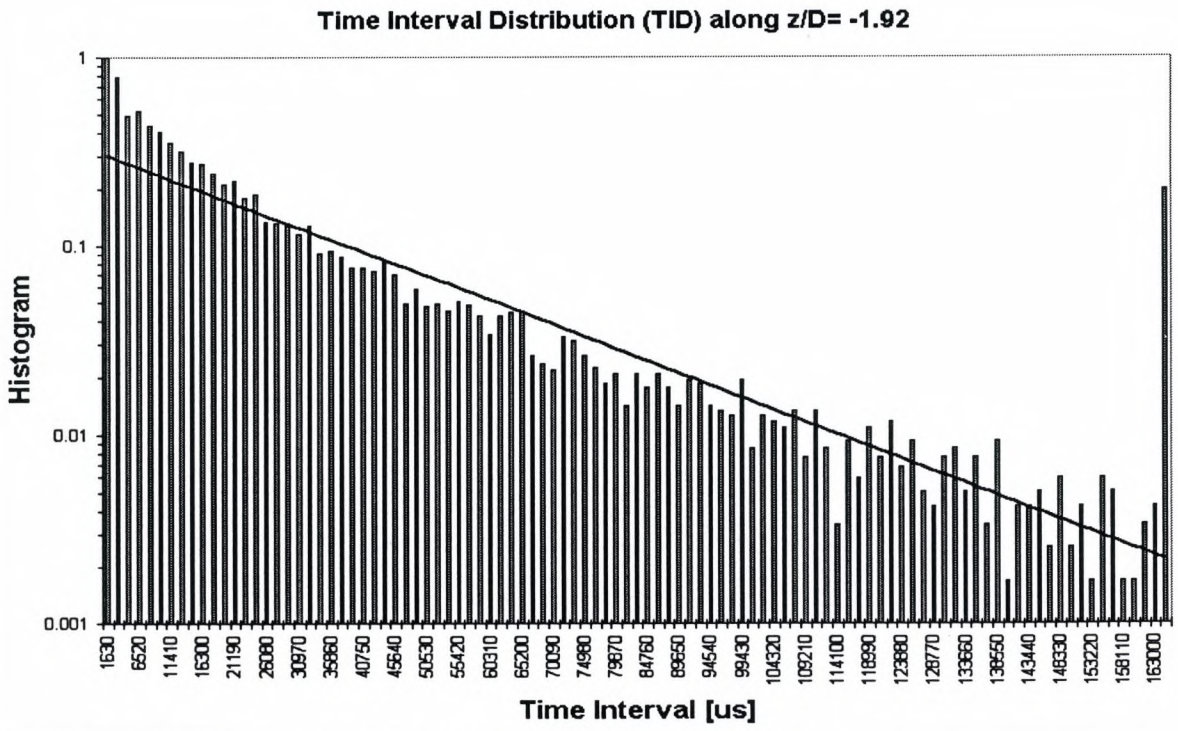

Figure D-5 Time Interval Distribution (TID) at z/D = -1.92

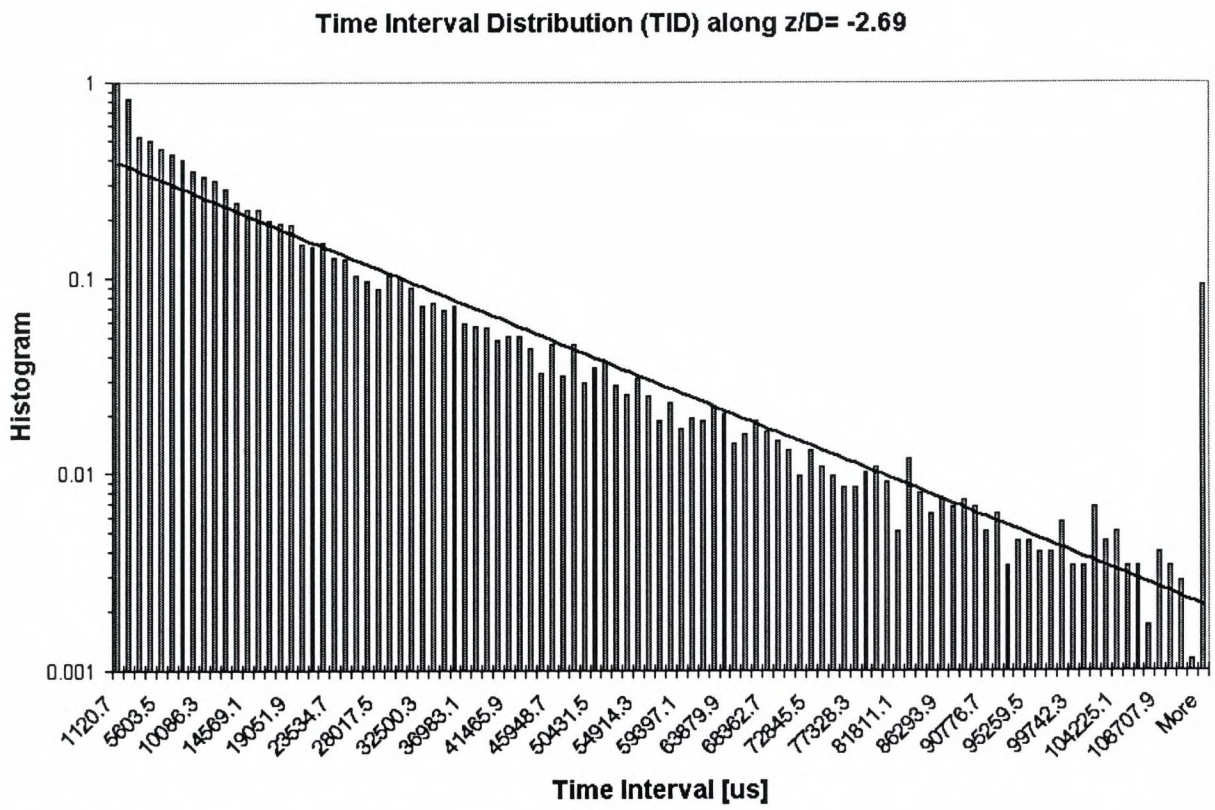

Figure D-6 Time Interval Distribution (TID) at z/D = -2.69

Appendix E Experimental Temperature Distributions

These profiles correspond to the measurements along the YZ-Plane at x/D = 12.7 and correspond to the points in figure 5.1.3-3.

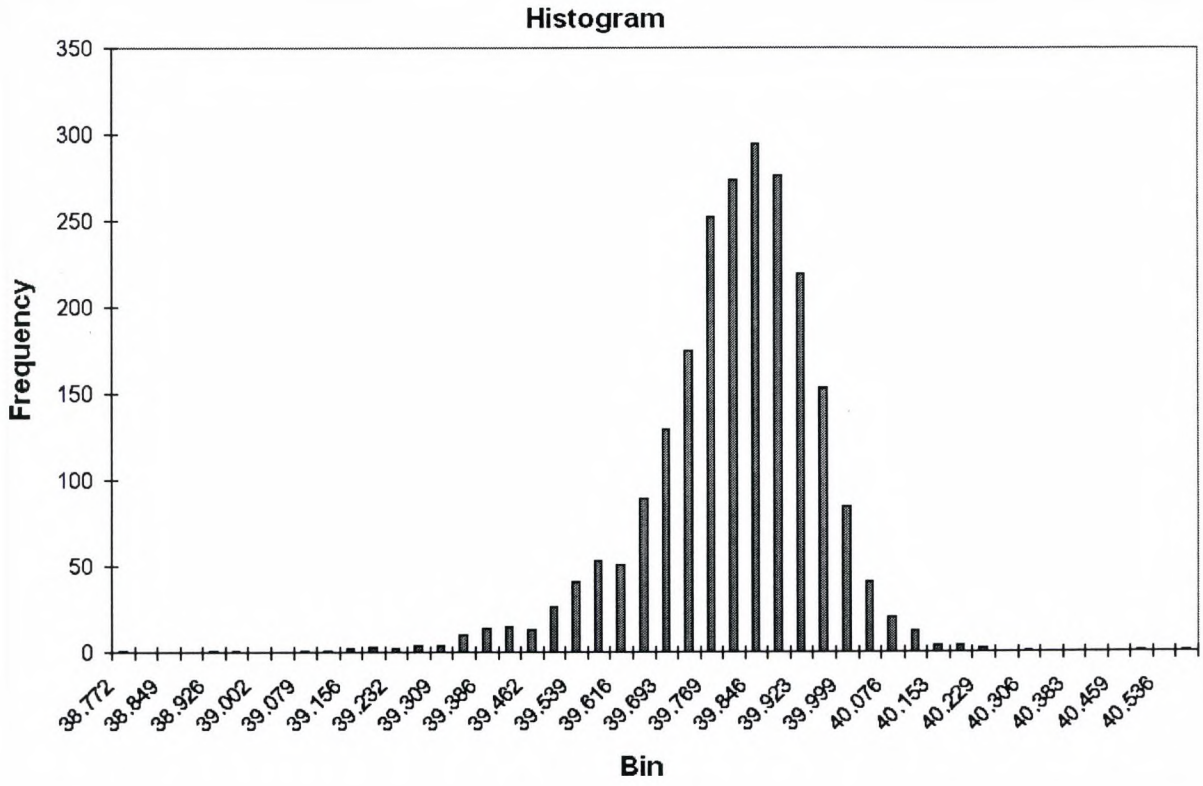

Figure E-1 Temperature distribution at x/D = 12.7, z/D = 3.7, y/D = -2.9

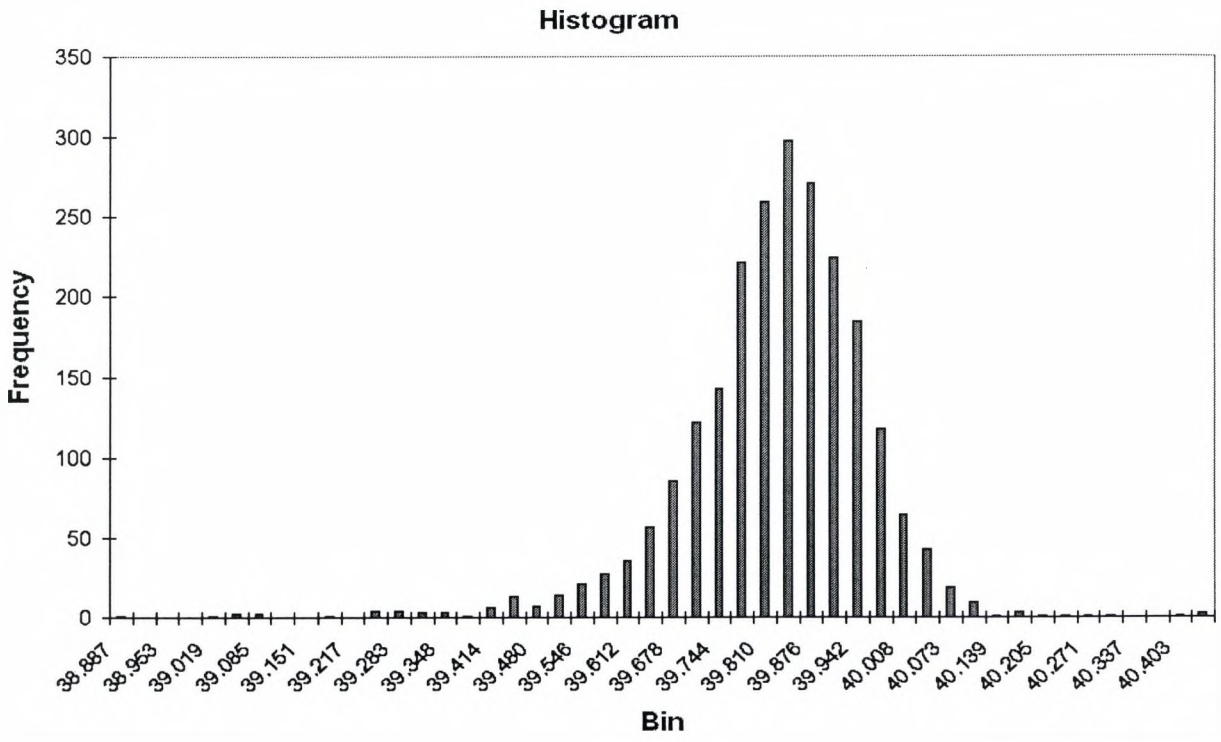

Figure E-2 Temperature distribution at x/D = 12.7, z/D = 3.7,y/D = +2.9

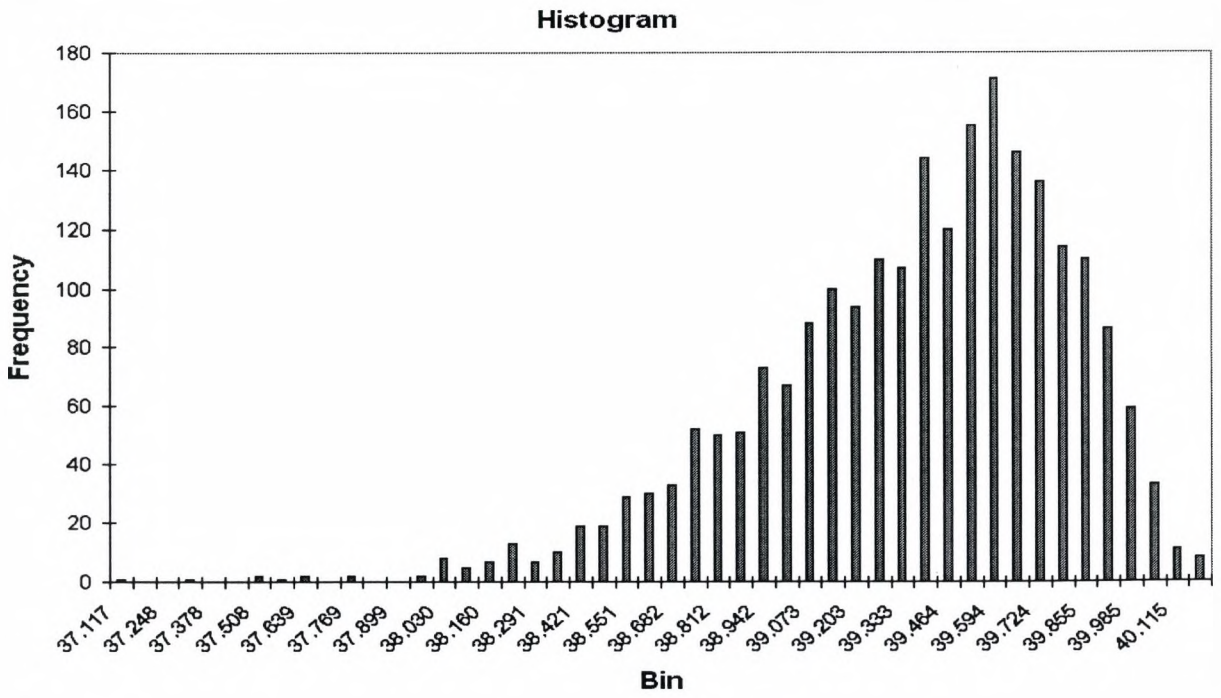

Figure E-3 Temperature distribution at x/D = 12.7, z/D = 1.5, y/D = -7.7

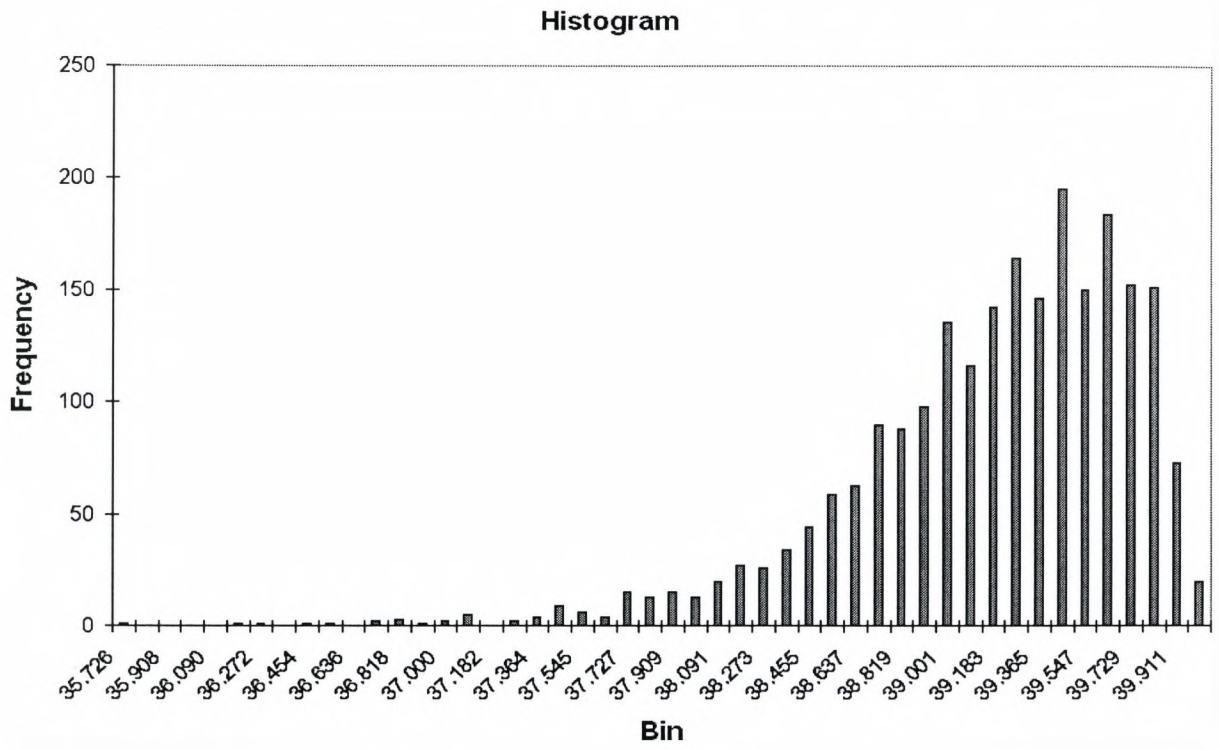

Figure E-4 Temperature distribution at x/D = 12.7, z/D = 1.5, y/D = -2.9

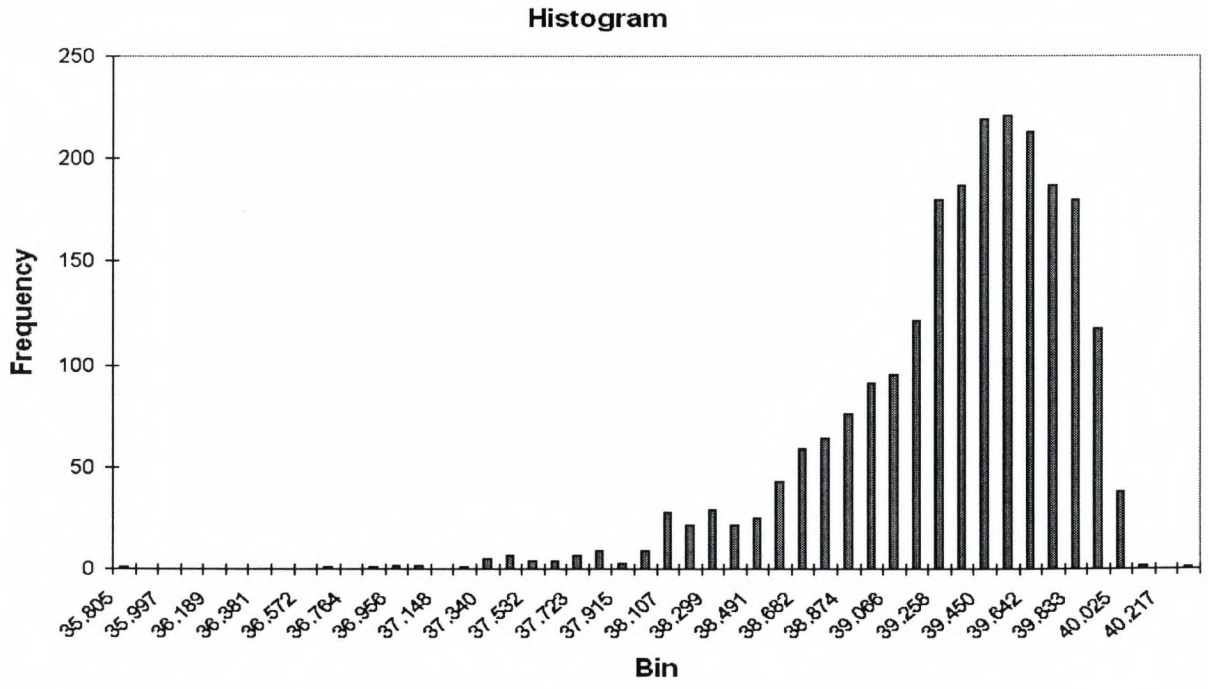

Figure E-5 Temperature distribution at x/D = 12.7, z/D = 1.5, y/D = +2.9

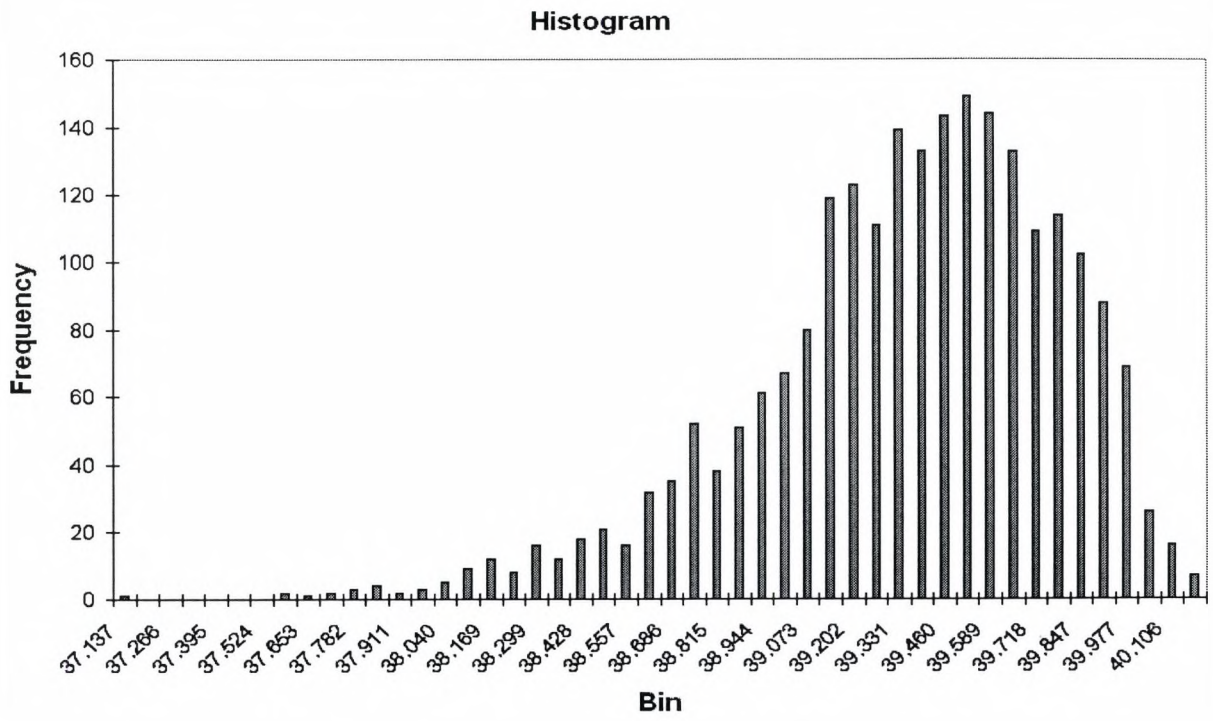

Figure E-6 Temperature distribution at x/D = 12.7, z/D = 1.5, y/D = +7.7

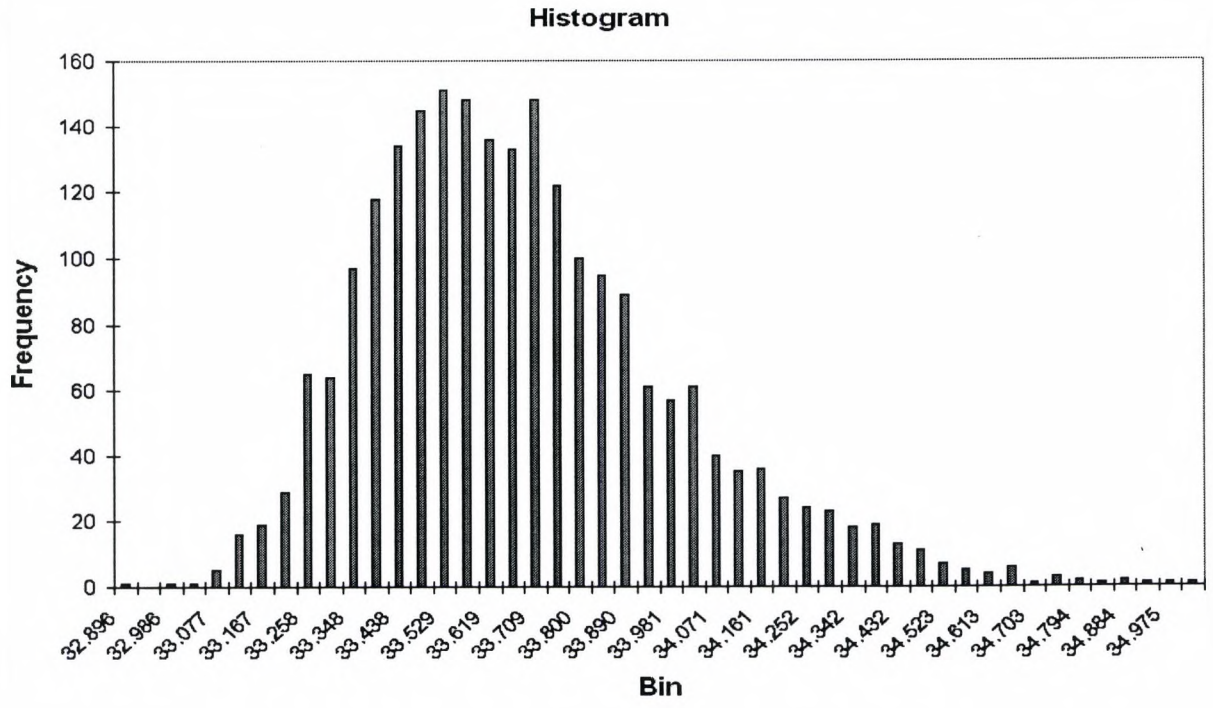

Figure E-7 Temperature distribution at x/D = 12.7, z/D = -0.24, y/D = -7.7

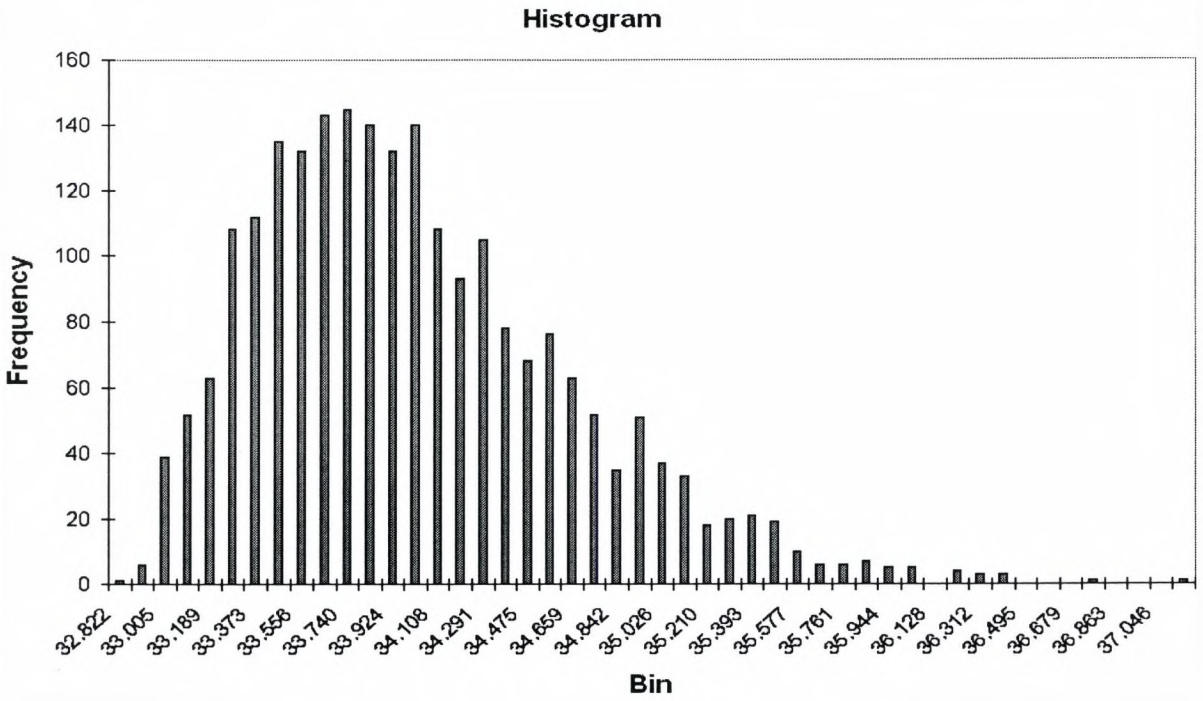

Figure E-8 Temperature distribution at x/D = 12.7, z/D = -0.24, y/D = -2.8

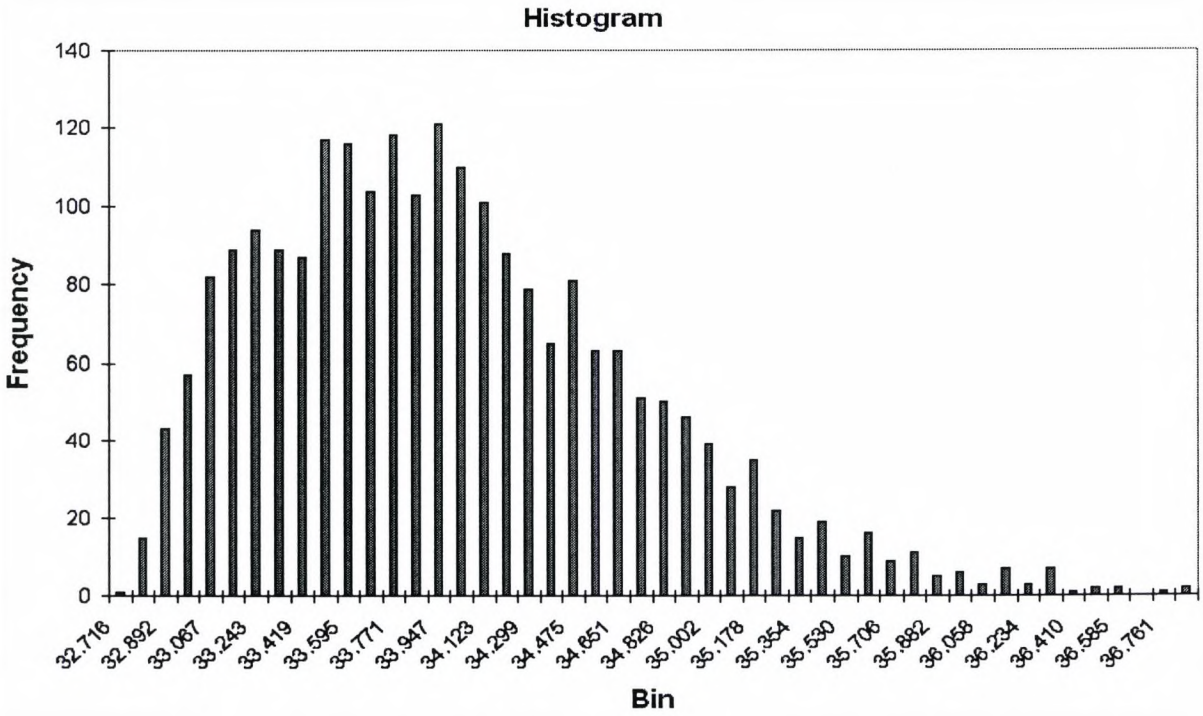

Figure E-9 Temperature distribution at x/D = 12.7, z/D = -0.24, y/D = +2.8

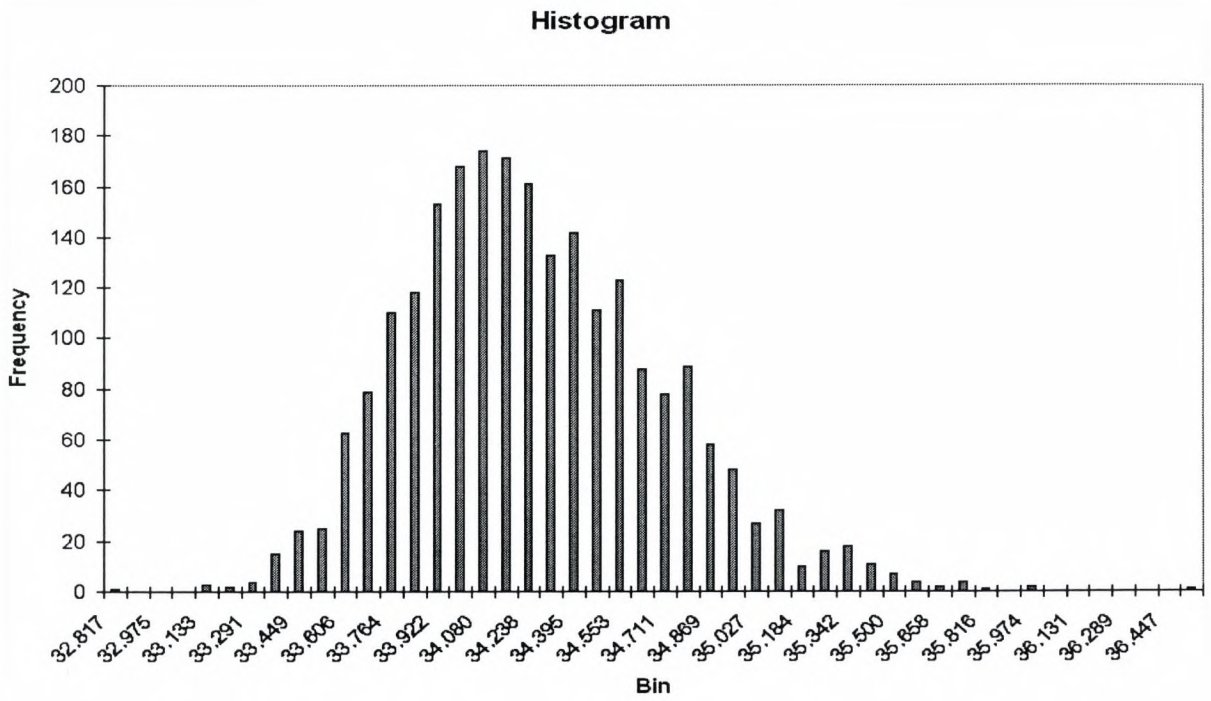

Figure E-10 Temperature distribution at x/D = 12.7, z/D = -0.24, y/D = +7.7

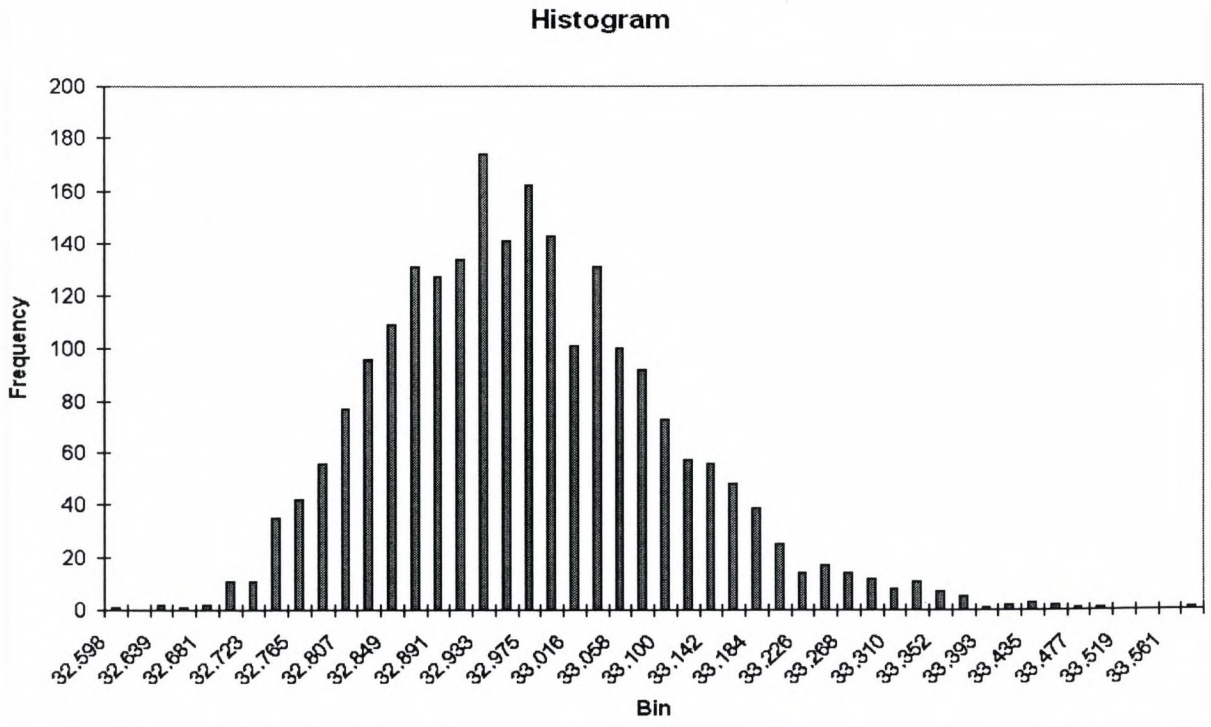

Figure E-11 Temperature distribution at x/D = 12.7, z/D = -2.05, y/D = -7.7

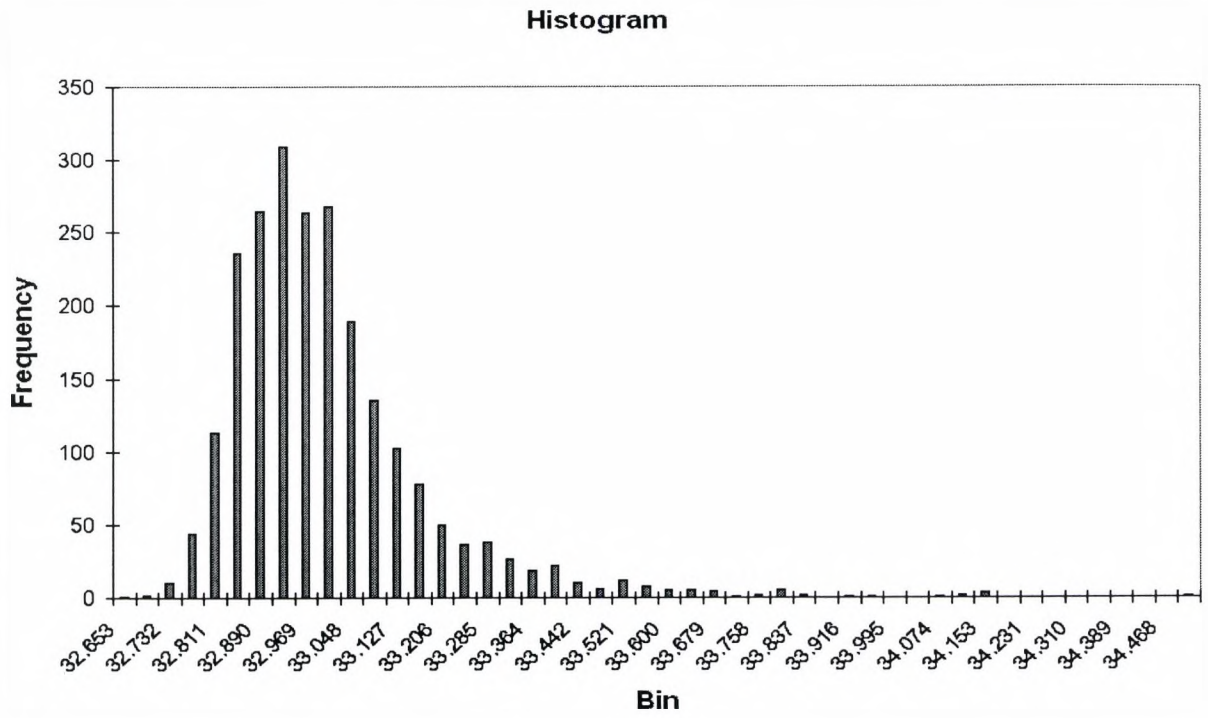

Figure E-12 Temperature distribution at x/D = 12.7, z/D = -2.05, y/D = -2.8

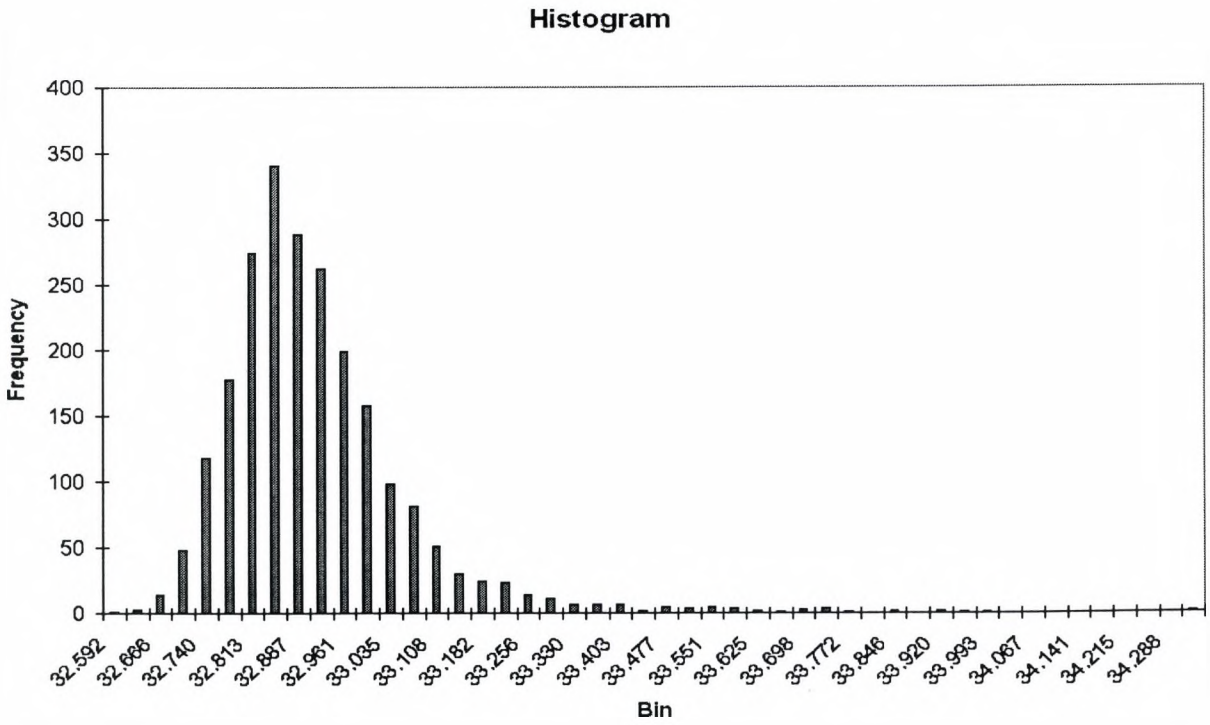

Figure E-13 Temperature distribution at x/D = 12.7, z/D = -2.05, y/D = +2.8

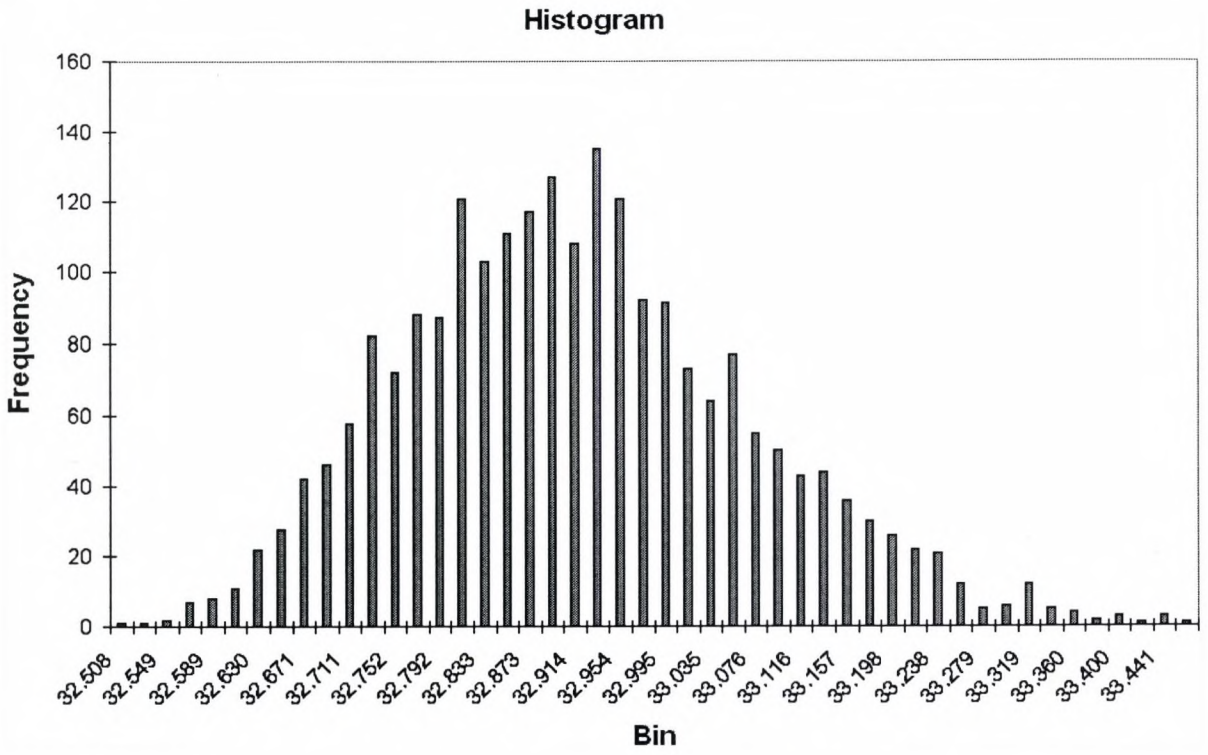

Figure E-14 Temperature distribution at x/D = 12.7, z/D = -2.05, y/D = +7.7

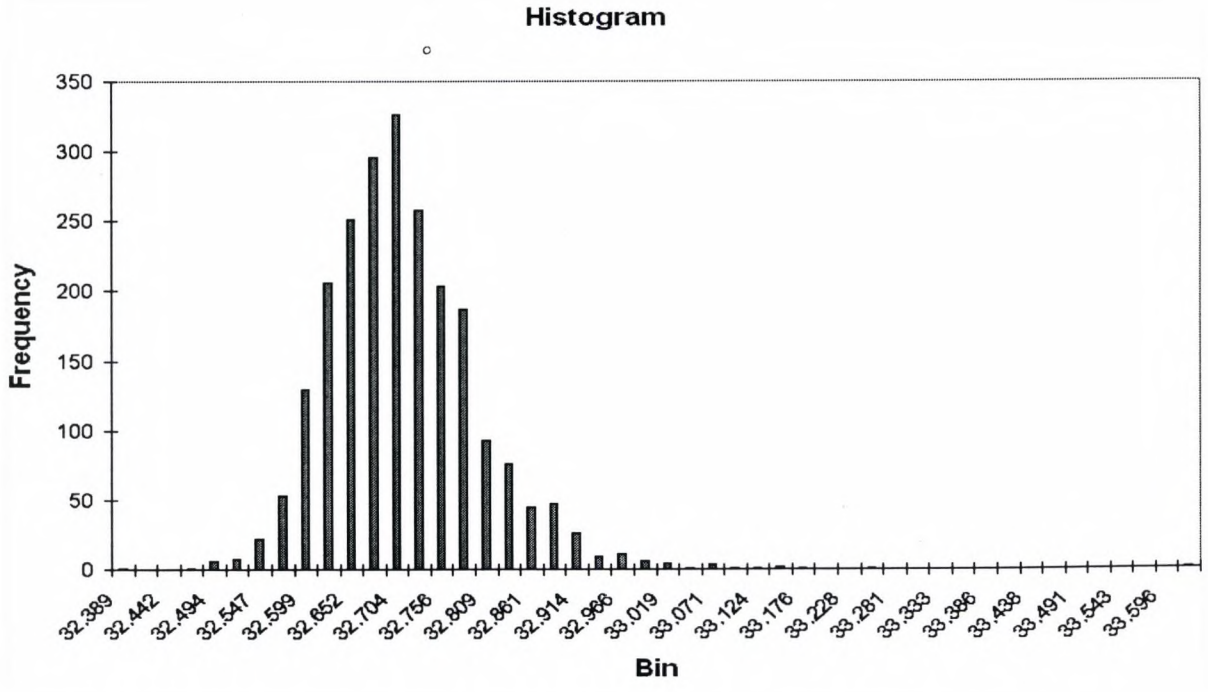

Figure E-15 Temperature distribution at x/D = 12.7, z/D = -3.99, y/D = -2.8

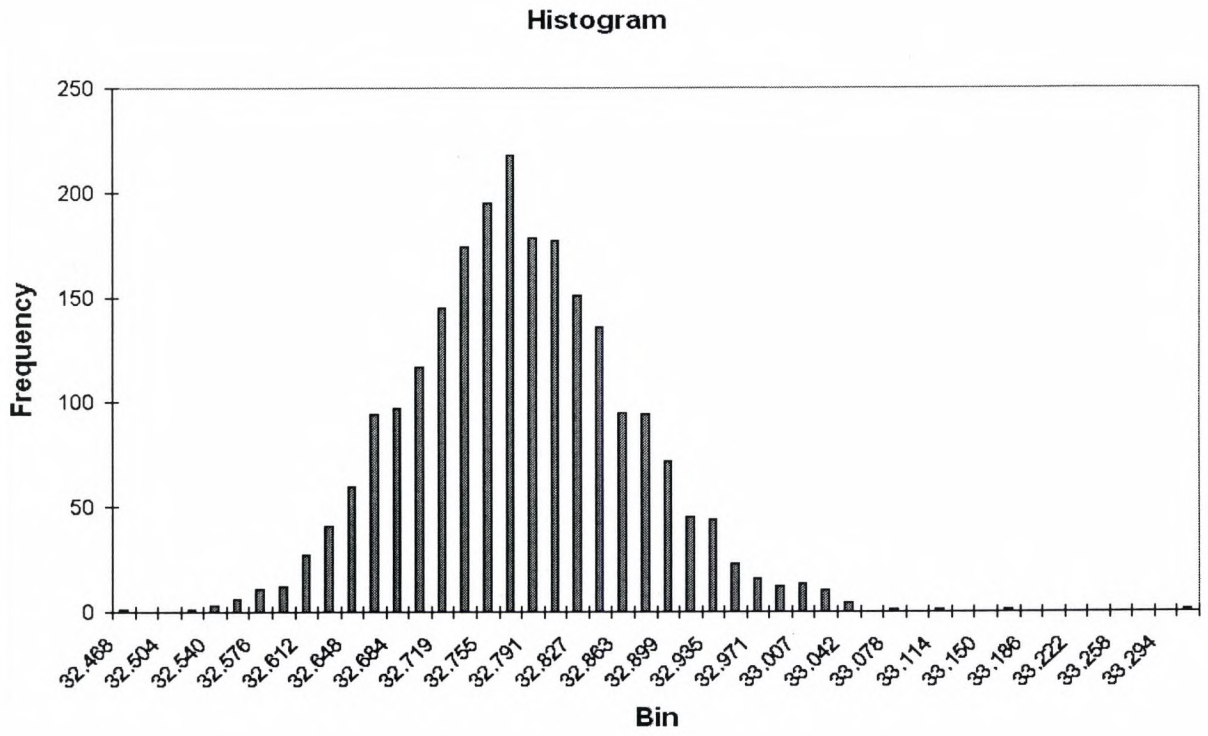

Figure E-16 Temperature distribution at x/D = 12.7, z/D = -3.99, y/D = 2.8

Appendix F Experimental PSD profiles

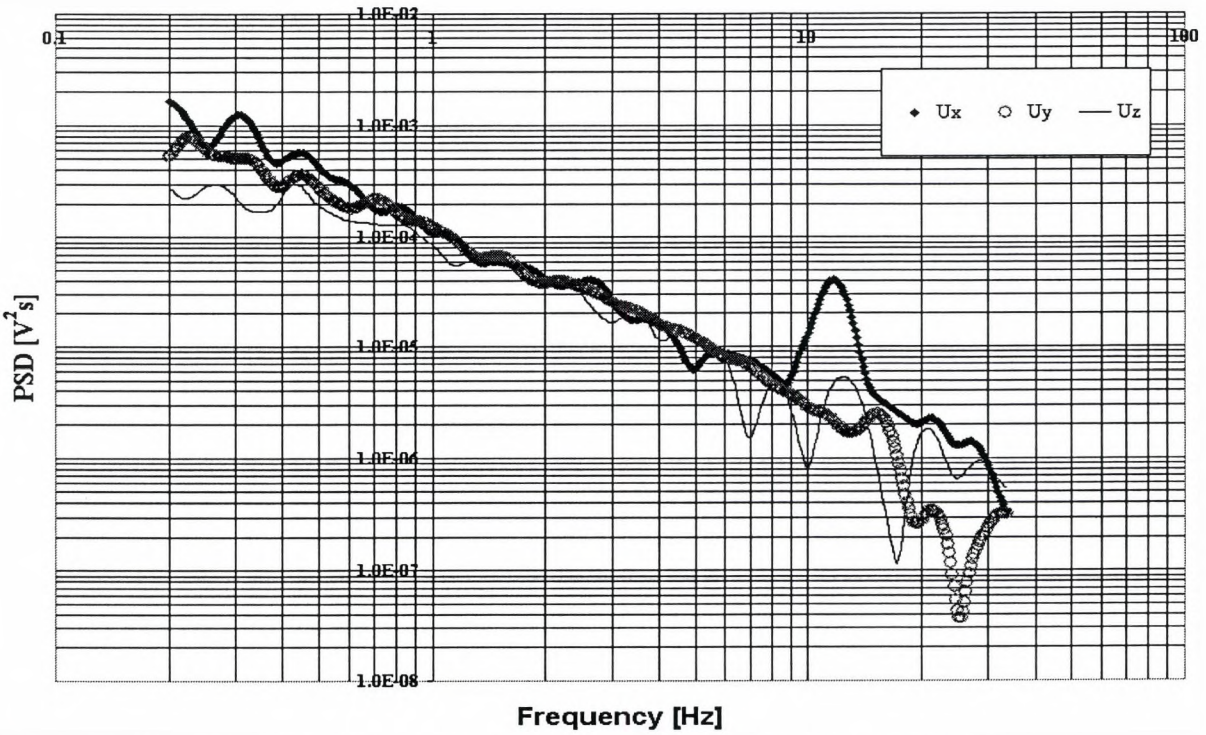

Figure F-1 Power Spectral Density profile at z/D = 3.46, x/D = 11.42, y/D = 0.

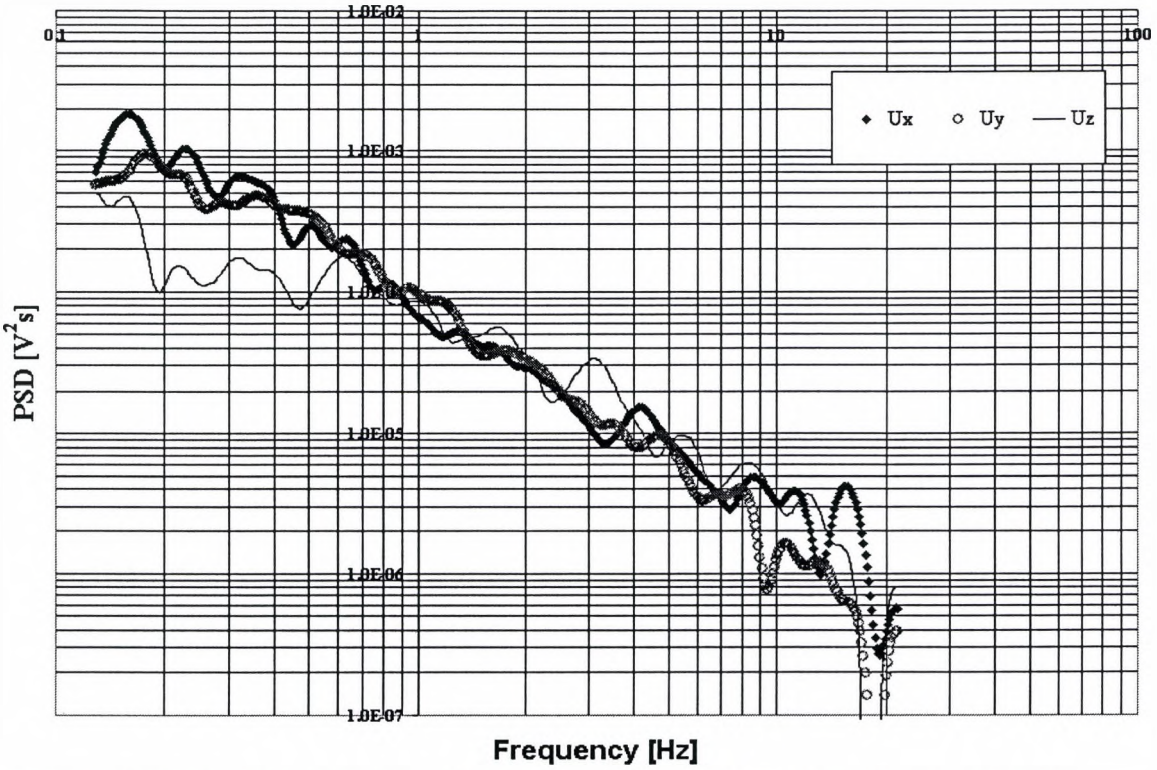

Figure F-2 Power Spectral Density profile at z/D = 2.69, x/D = 11.42, y/D = 0.

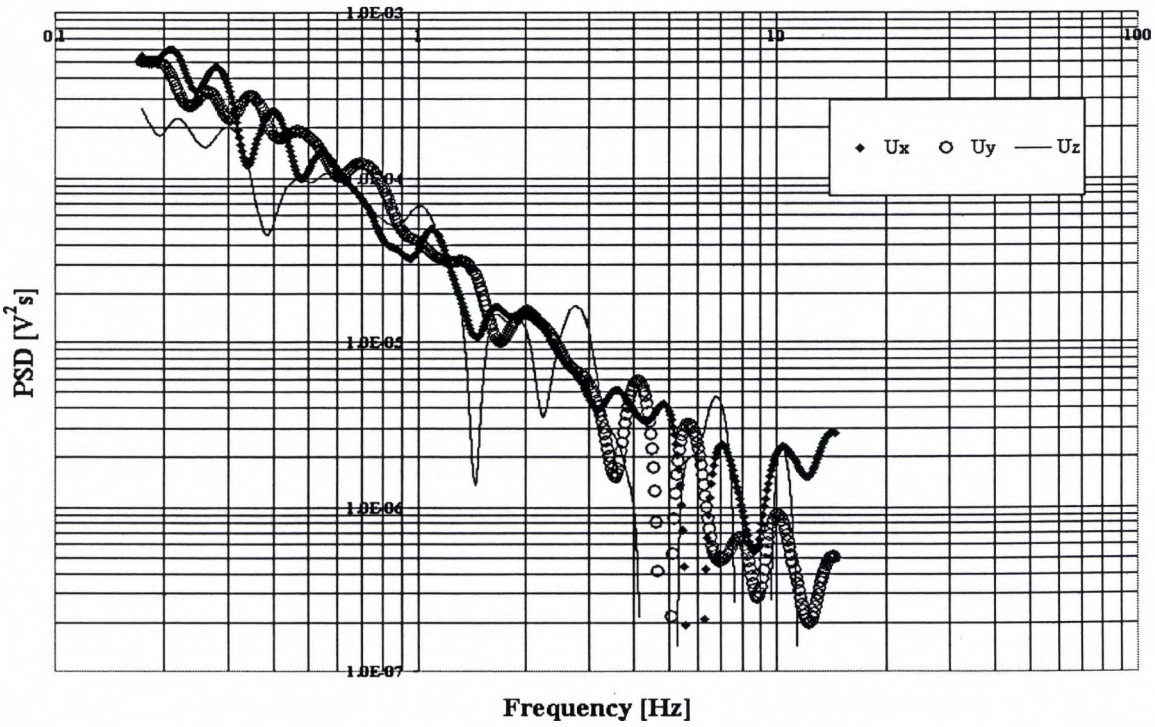

Figure F-3 Power Spectral Density profile at z/D = 1.92, x/D = 11.42, y/D = 0.

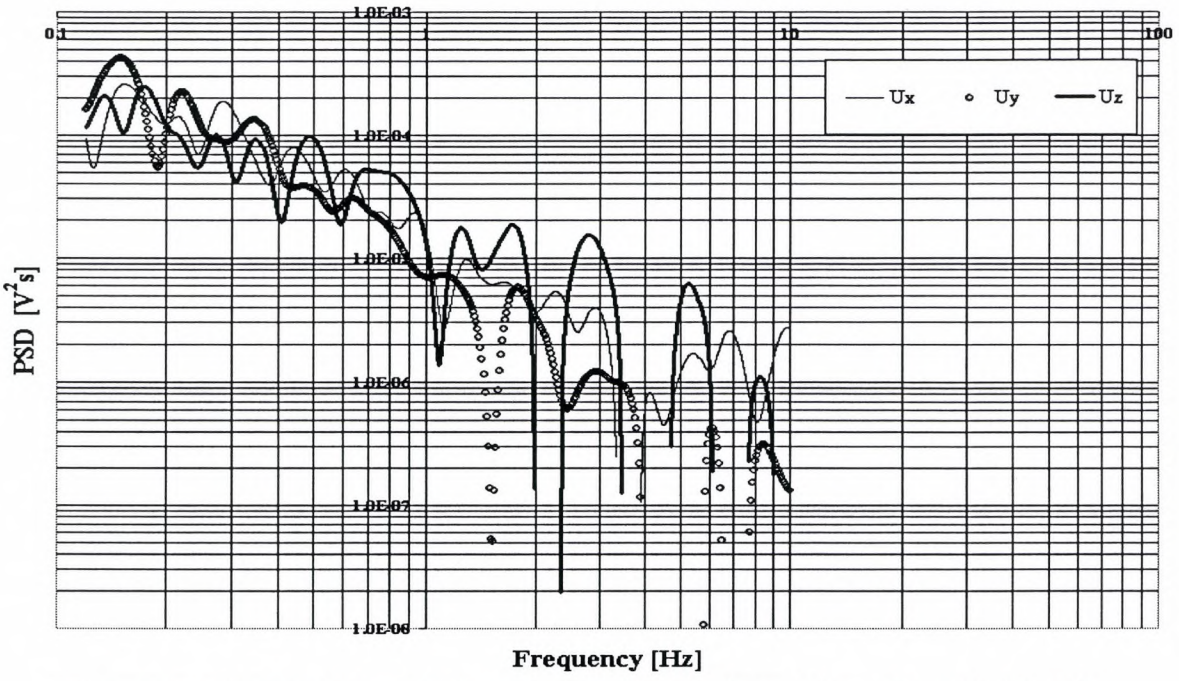

Figure F-4 Power Spectral Density profile at z/D = 1.15, x/D = 11.42, y/D = 0.

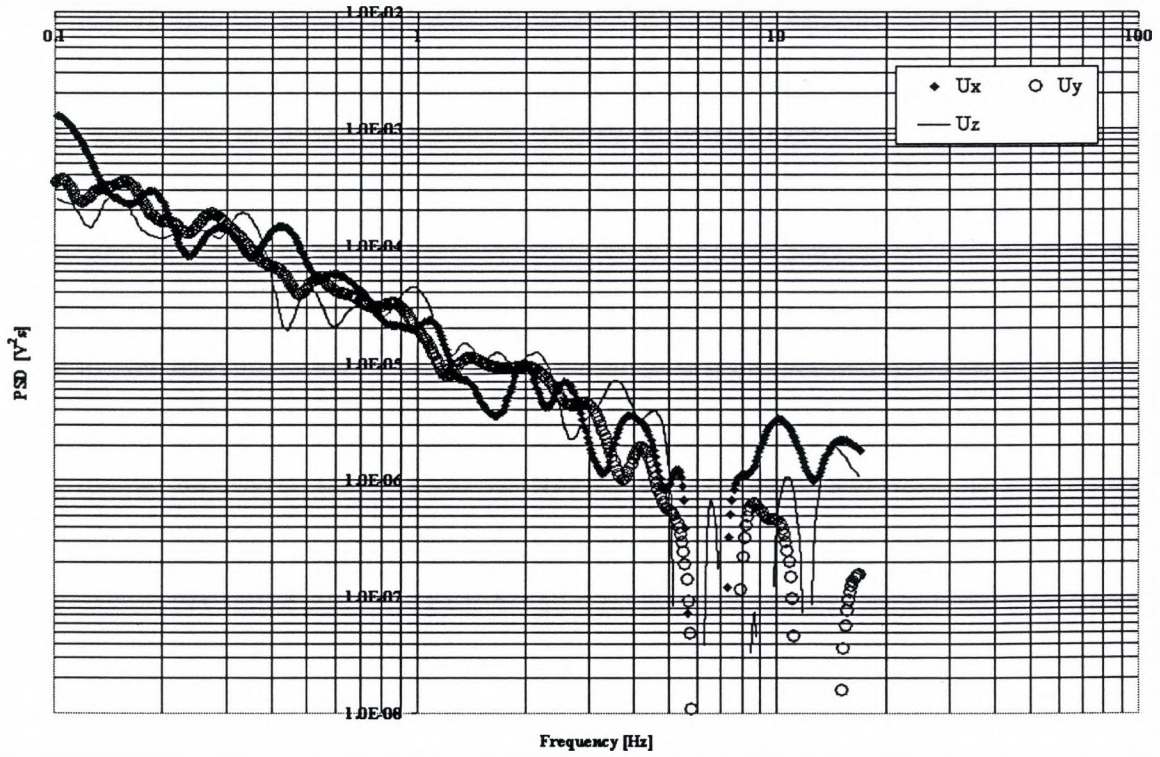

Figure F-5 Power Spectral Density profile at z/D = 0.38, x/D = 11.42, y/D = 0.

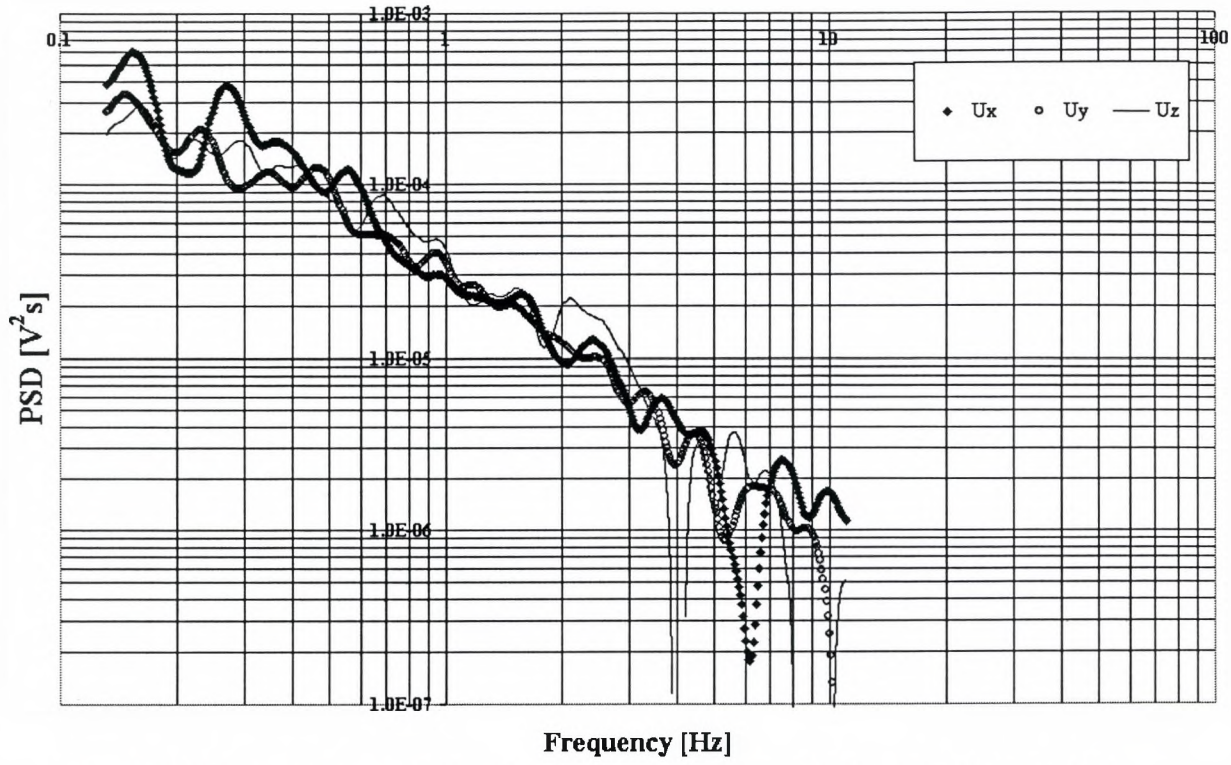

Figure F-6 Power Spectral Density profile at z/D = -0.38, x/D = 11.42, y/D = 0

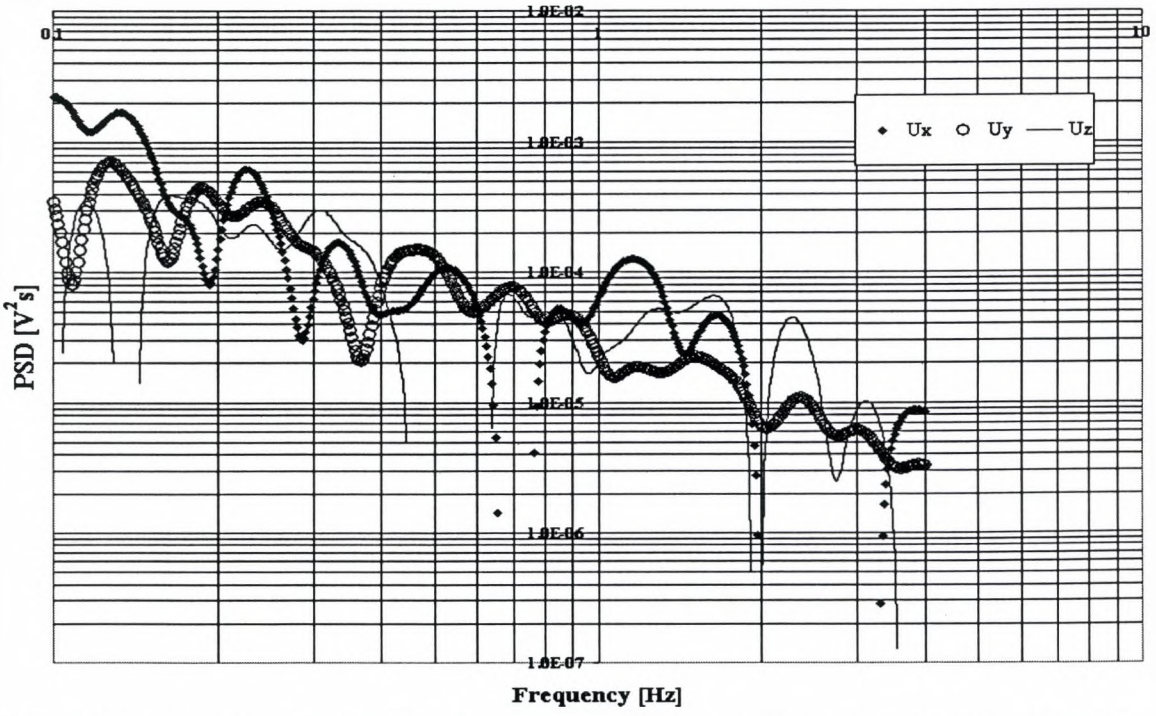

Figure F-7 Power Spectral Density profile at z/D = -1.15, x/D = 11.42, y/D = 0. Results were poor due to the lower data rate (~14 Hz), which limited the maximum displayable frequency.

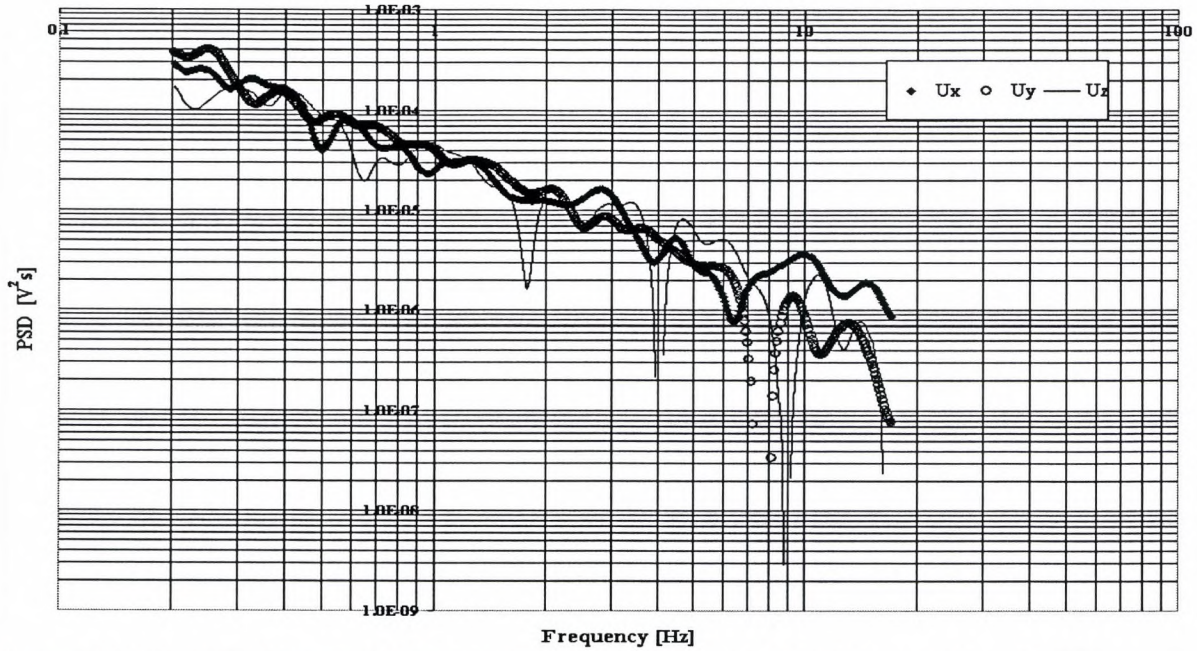

Figure F-8 Power Spectral Density profile at z/D = -1.92, x/D = 11.42, y/D = 0.

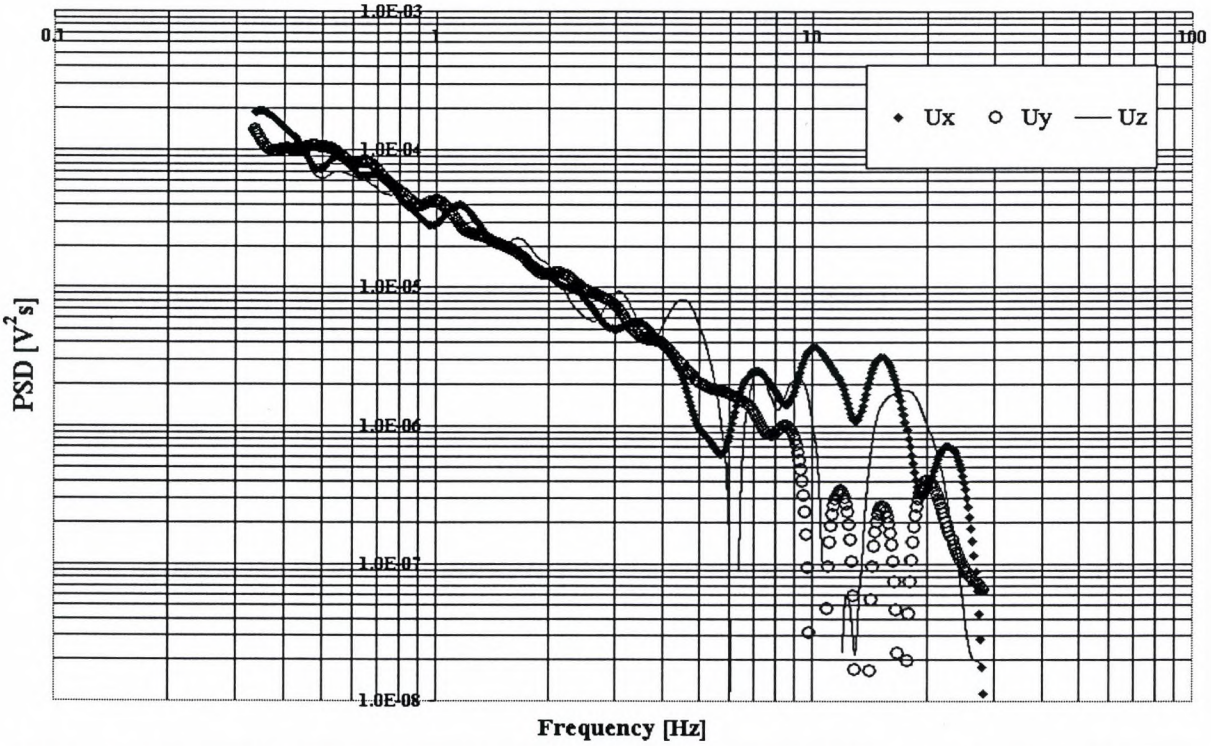

Figure F-9 Power Spectral Density profile at z/D = -2.69, x/D = 11.42, y/D = 0